ALMA MATER STUDIORUM
UNIVERSITÀ DI BOLOGNA

FACOLTÀ DI SCIENZE MATEMATICHE, FISICHE E NATURALI
DIPARTIMENTO DI ASTRONOMIA

THE VIMOS-VLT DEEP SURVEY: THE EVOLUTION OF TYPE–1 AGN

TESI DI DOTTORATO
DI
ANGELA BONGIORNO

RELATORE: **PROF. B. MARANO**

CO-RELATORE: **PROF. G. ZAMORANI**

COORDINATORE: **PROF. L. MOSCARDINI**

SCUOLA DI DOTTORATO IN SCIENZE MATEMATICHE, FISICHE E ASTRONOMICHE
DOTTORATO DI RICERCA IN ASTRONOMIA, XIX CICLO (2003–2006)

SETTORE SCIENTIFICO DISCIPLINARE: AREA 02 - SCIENZE FISICHE
FIS/05 ASTRONOMIA E ASTROFISICA

A Filippo e Valeria

Abstract

Quasars and AGN play an important role in many aspects of the modern cosmology. Of particular interest is the issue of the interplay between AGN activity and formation and evolution of galaxies and structures. Studies on nearby galaxies revealed that most (and possibly all) galaxy nuclei contain a super-massive black hole (SMBH) and that between a third and half of them are showing some evidence of activity (Kormendy and Richstone, 1995). The discovery of a tight relation between black holes mass and velocity dispersion of their host galaxy suggests that the evolution of the growth of SMBH and their host galaxy are linked together. In this context, studying the evolution of AGN, through the luminosity function (LF), is fundamental to constrain the theories of galaxy and SMBH formation and evolution. Recently, many theories have been developed to describe physical processes possibly responsible of a common formation scenario for galaxies and their central black hole (Volonteri et al., 2003; Springel et al., 2005a; Vittorini et al., 2005; Hopkins et al., 2006a) and an increasing number of observations in different bands are focused on collecting larger and larger quasar samples. Many issues remain however not yet fully understood.

In the context of the **VVDS** (VIMOS-VLT Deep Survey), we collected and studied an unbiased sample of spectroscopically selected faint type-1 AGN with a unique and straightforward selection function. Indeed, the VVDS is a large, purely magnitude limited spectroscopic survey of faint objects, free of any morphological and/or color pre-selection. We studied the statistical properties of this sample and its evolution up to redshift $z \sim 4$.

Because of the contamination of the AGN light by their host galaxies at the faint magnitudes explored by our sample, we observed that a significant fraction of AGN in our sample would be missed by the UV excess and morphological criteria usually adopted for the pre-selection of optical QSO candidates. If not properly taken into account, this failure in selecting particular sub-classes of AGN could, in principle, affect some of the conclusions drawn from samples of AGN based on these selection criteria.

The absence of any pre-selection in the VVDS leads us to have a very complete sample of AGN, including also objects with unusual colors and continuum shape. The VVDS AGN sample shows in fact redder colors than those expected by comparing it, for example,

with the color track derived from the SDSS composite spectrum. In particular, the faintest objects have on average redder colors than the brightest ones. This can be attributed to both a large fraction of dust-reddened objects and a significant contamination from the host galaxy. We have tested these possibilities by examining the global spectral energy distribution of each object using, in addition to the U, B, V, R and I-band magnitudes, also the UV-Galex and the IR-Spitzer bands, and fitting it with a combination of AGN and galaxy emission, allowing also for the possibility of extinction of the AGN flux. We found that for $\sim$44% of our objects the contamination from the host galaxy is not negligible and this fraction decreases to $\sim$21% if we restrict the analysis to a bright sub-sample (M_{1450} <-22.15).

Our estimated integral surface density at $I_{AB} < 24.0$ is $\sim$ 500 AGN per square degree, which represents the highest surface density of a spectroscopically confirmed sample of optically selected AGN.

We derived the luminosity function in B-band for $1.0 < z < 3.6$ using the $1/V_{max}$ estimator. Our data, more than one magnitude fainter than previous optical surveys, allow us to constrain the faint part of the luminosity function up to high redshift. A comparison of our data with the 2dF sample at low redshift ($1 < z < 2.1$) shows that the VDDS data can not be well fitted with the pure luminosity evolution (PLE) models derived by previous optically selected samples. Qualitatively, this appears to be due to the fact that our data suggest the presence of an excess of faint objects at low redshift ($1.0 < z < 1.5$) with respect to these models.

By combining our faint VVDS sample with the large sample of bright AGN extracted from the SDSS DR3 (Richards et al., 2006b) and testing a number of different evolutionary models, we find that the model which better represents the combined luminosity functions, over a wide range of redshift and luminosity, is a luminosity dependent density evolution (LDDE) model, similar to those derived from the major X-surveys. Such a parameterization allows the redshift of the AGN density peak to change as a function of luminosity, thus fitting the excess of faint AGN that we find at $1.0 < z < 1.5$.

On the basis of this model we find, for the first time from the analysis of optically selected samples, that the peak of the AGN space density shifts significantly towards lower redshift going to lower luminosity objects. The position of this peak moves from z$\sim$ 2.0 for M_B <-26.0 to z$\sim$ 0.65 for -22< M_B <-20.

This result, already found in a number of X-ray selected samples of AGN, is consistent with a scenario of “AGN cosmic downsizing”, in which the density of more luminous AGN, possibly associated to more massive black holes, peaks earlier in the history of the Universe (i.e. at higher redshift), than that of low luminosity ones, which reaches its maximum later (i.e. at lower redshift).

This behavior has since long been claimed to be present in elliptical galaxies and it is not

easy to reproduce it in the hierarchical cosmogonic scenario, where more massive Dark Matter Halos (DMH) form on average later by merging of less massive halos.

Contents

1 Introduction **1**

2 Active Galactic Nuclei **7**
2.1 History 7
2.2 Properties of AGN 9
2.3 Mass of the central object 10
2.4 Classification of AGN 11
2.5 Unified Model 13

3 AGN selection techniques **17**
3.1 Optical surveys 17
3.1.1 Optical selection of type–1 AGN 17
3.1.2 Optical selection of type–2 AGN 21
3.2 Radio surveys 22
3.3 X-ray surveys 23
3.4 Infrared surveys 24

4 The VIMOS-VLT Deep Survey **27**
4.1 Survey goals 28
4.2 Survey strategy 28
4.2.1 The VVDS multi-wavelength imaging survey 29
4.2.2 The VVDS spectroscopic survey 30
4.2.3 Target selection 31
4.2.4 Spectral classification 32
4.3 Deep spectroscopic sample and main survey results 35
4.3.1 Redshift distribution of the $I_{AB} \leq 24$ galaxy sample 35
4.3.2 Galaxy evolution 36
4.3.3 Evolution of the correlation function and bias 37
4.3.4 The large scale structure 38
4.3.5 The high redshift Universe 39

5 The VVDS type–1 AGN Sample **41**
5.1 The AGN selection . . . 41
5.1.1 Identification and redshift quality flags . . . 41
5.2 The BLAGN catalog . . . 42
5.2.1 Redshift degeneracy . . . 42
5.3 Redshift distribution . . . 47
5.4 A-posteriori morphological analysis and color-color diagrams . . . 48
5.4.1 Morphological analysis . . . 49
5.4.2 Color-Color diagrams analysis . . . 51
5.5 Composite Spectrum . . . 52
5.6 Colors of our sample . . . 54
5.6.1 Decomposition of active galactic nucleus and host galaxy components . . . 60

6 AGN Number Counts **69**
6.1 VVDS selection function for BLAGN . . . 69
6.1.1 Treatment of non-targeted BLAGN: w^{TSR} . . . 69
6.1.2 Treatment of misclassified AGN: w^{SSR} . . . 70
6.2 Coherent sample . . . 72
6.3 AGN Surface Density . . . 72

7 Evolution of type–1 AGN **77**
7.1 Luminosity function . . . 77
7.1.1 The V/V_{max} test . . . 78
7.1.2 Computation and Parameterization of the Luminosity Function . . . 78
7.2 AGN evolution: main results . . . 79

8 The VVDS type–1 AGN luminosity function **87**
8.1 Definition of the redshift range . . . 87
8.2 The K-correction . . . 87
8.3 Estimate of the absolute magnitude . . . 88
8.4 Computation of the luminosity function: the $1/V_{max}$ estimator . . . 90
8.5 Comparison with the results from other optical surveys . . . 91
8.5.1 The low redshift luminosity function . . . 91
8.5.2 The high redshift luminosity function . . . 93
8.6 The bolometric luminosity function . . . 93
8.7 Model fitting . . . 97
8.7.1 The PLE and PDE models . . . 97
8.7.2 The LDDE model . . . 98
8.8 The AGN activity as a function of redshift . . . 101

9 Conclusion **107**

List of Figures **120**

List of Tables **121**

Chapter 1

Introduction

Since their discovery, AGN were recognized as a remarkable class of objects. They in fact emit in the whole electromagnetic spectrum and are found to be highly variable in all the bands in which they have been observed. Their luminosities are $\sim$ 100 times larger than that of normal galaxies and they are thus visible up to large distances, where even the brightest normal galaxies would be not visible. Moreover, shortly after their discovery, it was understood that these objects were truly remarkable, not only in their physical nature but also in their cosmological evolution. Schmidt (1968) observed a very sharp decline in the space density on quasars, over roughly a factor of 100 from z$\sim$2 to z$\sim$0. This decline was so remarkable, that it could be credibly demonstrated from a small sample (33 objects). Many studies have been later performed in order to study the evolution of this population of objects in a wide redshift range but the general picture is not yet so clear.

Moreover, quasars and AGN play an important role in many aspects of the modern cosmology. Today, the main attention is focused on the issue of the interplay between AGN activity and formation and evolution of galaxies and structures.

The currently favored cosmological model for the formation and evolution of galaxies and structures in the Universe is the Λ *Cold Dark Matter*[1] (ΛCDM) model in which structures formed hierarchically through gravitational instability, with smaller ones originating first and then merging to produce successively larger bodies. As baryons fall into the potential wells created by the dark matter, the gas is shocked but it can cool radiatively to form stars and galaxies, in a "bottom-up" progression (White & Rees, 1978).

Even with the many successes of this picture, the processes underlying galaxy formation and evolution are poorly understood and some observational evidences are still not easy to reproduce (e.g. downsizing in elliptical galaxies; Cowie et al., 1996).

The difficulties in understanding these processes lie probably not in the initial conditions

[1]The Λ *Cold Dark Matter Model* assumes non-relativistic Dark Matter particles and takes into account the cosmological constant Λ. In this model the matter density Ω_m is taken smaller than 1, and a new quantity $\Omega_\Lambda = \rho_\Lambda/\rho_{crit}$ is introduced, in order that the sum of Ω_m and Ω_Λ is 1. Ω_Λ has a similar meaning with respect to Ω_m and is linked to the value of the cosmological constant.

or in the description of the Dark Matter, but rather in the physics that has been used to model the baryons.

Observational studies have revealed significant regularities in the structure of galaxies that identify some of the physics that has seemingly been "missing" from the theoretical calculations. For example, it is now believed that SHBH reside at the center of most (and possibly all) galaxies and that between a third and half of them are showing some evidence of activity (Kormendy & Richstone, 1995). Moreover, it has been established that the masses of these BH are correlated with either the mass (Magorrian et al., 1998; McLure & Dunlop, 2002; Marconi & Hunt, 2003) or the velocity dispersion (i.e. the $M_{BH} - \sigma$ relation: Ferrarese & Merritt, 2000; Gebhardt et al., 2000; Tremaine et al., 2002) of spheroids, demonstrating a fundamental link between the growth of SMBHs and galaxy formation. Simulations that simultaneously follow star formation and the growth of BH during galaxy-galaxy collisions have been performed by Di Matteo et al. (2005). They found that, in addition to generating a burst of star formation, a merger leads to strong inflows that feed gas to the SMBH and thereby power the QSO. Moreover, the energy released by the QSOs can have a global impact on the structure of the merger remnant. Applying this conclusion to spheroid formation in general, the simulations demonstrate that models for the origin and evolution of galaxies must account for black hole growth and feedback in a fully *self-consistent* manner.

Given these evidences, a large number of theories have been developed to describe physical processes possibly responsible of a common formation scenario for galaxies and their central black holes.
Analytical and semi-analytical models (Silk & Rees, 1998; Fabian, 1999; Wyithe & Loeb, 2002; Steed & Weinberg, 2003) suggest that, beyond a certain threshold, feedback energy from black holes can expel gas from the centers of galaxies, shutting down accretion onto them and thus limiting their masses. However, these calculations usually ignore the impact of this process on star formation and therefore do not explain the link between black hole growth and spheroid formation. Springel et al. (2005a) have incorporated black hole growth and feedback into simulations of galaxy mergers to explore the implications of these processes for galaxy formation and evolution. Di Matteo et al. (2005) and Springel et al. (2005b) have shown that gas inflows excited by gravitational torques during a merger both trigger starbursts and fuel rapid black hole growth. The growth of the black hole is determined by the gas supply and terminates as gas is expelled by feedback, halting accretion, leaving a dead quasar in an ordinary galaxy. Hopkins et al. (2006a) proposed a picture for galaxy formation and evolution, in which starbursts, quasars, and the simultaneous formation of spheroids and supermassive black holes represent connected phases in the life of galaxies. In this picture, mergers are expected to occur regularly in a hierarchical universe, particularly at high redshifts.

All these models must be compared with both local and high redshift observations, in order to set significant constraints on the relative importance of the involved processes. In this context, the shape and evolution of the quasar luminosity function (QLF) is fundamental to constrain theories of galaxy and SMBH formation, and it is therefore essential to obtain unbiased AGN samples at high redshifts. This requirement has stimulated an increasing number of observations in different bands focused on collecting larger and larger quasar samples.

A growing number of observations at different redshifts, in radio, optical and soft and hard X-ray bands, are suggesting that the faint end slope of the AGN luminosity function evolves, becoming flatter at high redshift (Page et al., 1997; Miyaji et al., 2000, 2001; La Franca et al., 2002; Cowie et al., 2003; Ueda et al., 2003; Fiore et al., 2003; Hunt et al., 2004; Cirasuolo et al., 2005; Hasinger et al., 2005). This evolution, now dubbed as "AGN cosmic downsizing" is described either as a direct evolution in the faint end slope or as "luminosity dependent density evolution" (LDDE), and it has been the subject of many speculations since it implies that the space density of high luminosity AGN peaks earlier in the history of the Universe (i.e. at higher redshift), while the density of low luminosity ones reaches its maximum later (i.e. at lower redshift). In particular, the peak of the AGN number density shifts from z $\sim$ 0.5 - 0.7 at $L_x \sim 10^{42} - 10^{43}$, to z $\sim$ 2.5 at $L_x \sim 10^{46}$. The same conclusion holds for the analysis of the accretion history of SMBHs: most massive BHs accreted mass faster and at higher redshifts (z $>$ 1.5), while the lower mass BHs have mostly grown at z $<$ 1.5 (Shankar et al., 2004). This behavior has been claimed to be present also in elliptical galaxies and, as already said, is not easy to reproduce in the hierarchical cosmogonic scenario, where more massive Dark Matter Halos (DMH) form on average later by merging of less massive halos.

The first models of the quasars LF have relied on restrictive assumptions about quasar lifetime and light curve. They generally assumed that quasars radiate at a fixed luminosity for some characteristic lifetime, or adopt simplified exponential light curves. Under these circumstances, the distribution of quasars with a given mass or peak luminosity is trivially related to the observed LF, and the two are essentially identical in shape.

Recent simulations, which incorporate the BH growth and feedback into numerical simulations of galaxy mergers (Springel et al., 2005a,b; Di Matteo et al., 2005), reproducing the $M_{BH} - \sigma$ relation and linking quasar activity to galaxy evolution, predict a more complicated quasar light curves then those adopted previously.

In the model of Hopkins et al. (2005a,b), quasars evolve rapidly and their lifetime depends on both their instantaneous *and* peak luminosities. Critically, the quasar lifetime in this model is longer at lower luminosities; i.e. a given quasar spends more time (and is more likely to be observed) at a luminosity well below its peak luminosity.

The resulting quasar light curves imply a qualitatively different picture of the QLF with

respect to what was previously considered. In this picture the steep bright end of the QLF consists of quasars radiating near their peak luminosities (Eddington limits), while the shallow faint end consists of quasars either growing efficiently in early stages of activity or in sub-Eddington quiescent states (with Eddington ratios generally between 0.01 and 1) going into or coming out of a period of peak activity (Hopkins et al., 2006b).

The "AGN cosmic downsizing" has not been clearly seen yet with optically selected AGN samples. By combining results from low and high redshifts, it is clear from the studies of optically selected samples that the cosmic QSO evolution shows a strong increase of the activity from $z \sim 0$ out to $z \sim 2$, reaches a maximum around $z \simeq 2-3$ and then declines, but the shape of the turnover and the redshift evolution of the peak in activity as a function of luminosity is still unclear.

Most of the optically selected AGN samples studied so far are obtained through various color (e.g. UV-excess) selections of candidates, followed by spectroscopic confirmation, or grism and slitless spectroscopic surveys. These samples are expected to be highly complete, at least for luminous AGN, at either $z \leq 2.2$ or $z \geq 3.6$, where AGN show conspicuous colors in broad band color searches, but less complete in the redshift range $2.2 \leq z \leq 3.6$ (Richards et al., 2002), where the maximum of the activity seems to occur.

An improvement in the multi-color selection in optical bands is through the simultaneous use of many broad and medium band filters as, for example, in the COMBO-17 survey (Wolf et al., 2003b). Such a survey is the only optical survey so far which, in addition to covering a redshift range large enough to see the peak of AGN activity, is also deep enough to sample up to high redshift AGN with luminosity below the break in the luminosity function. However, only photometric redshifts are available for this sample and, because of their selection criteria, it is incomplete for objects with a small ratio between the nuclear flux and the total host galaxy flux and for AGN with anomalous colors, such as, for example, the Broad Absorption Line (BAL) QSOs , which have on average redder colors and account for ($\sim 10 \div 15$) % of the overall AGN population.

The **VIMOS-VLT Deep Survey** is a spectroscopic survey in which the target selection is purely flux limited (in the I-band), with no additional selection criterion. This allows us to select a spectroscopic AGN sample free of biases in the redshift range $0 < z < 5$. An obvious advantage of such a selection is the possibility to test the completeness of the most current surveys, based on morphological and/or color pre-selection, and to study the evolution of AGN activity in a large redshift range.

In this thesis I will present the properties and the evolution of the spectroscopic type–1 AGN sample collected by the VVDS. The sample consists of 130 AGN with $0 < z < 5$, selected on the basis of their spectra in 3 VIMOS fields and in the Chandra Deep Field South (CDFS), which was partly included in the VVDS observations. It represents an unprecedented complete sample of faint AGN, free of morphological or color selection

bias.

The work is organized as follows:

- In Chapter 2 and 3 I will give a review of the main AGN properties and of the methods used to select them in different bands;
- In Chapter 4 I will present the *VIMOS-VLT Deep Survey* (VVDS), its observational strategy and the main scientific results obtained up to now;
- In Chapter 5 I will present the VVDS type–1 AGN sample selected from the VVDS sample, how it has been selected and its main properties;
- In Chapter 6 I will discuss the incompleteness function, the method used to account for it and the derived AGN number counts at $I_{AB} \leq 24$;
- In Chapter 7 I will introduce the luminosity function and I will briefly summarize the main results obtained up to now on the evolution of AGN;
- In Chapter 8 I will present the AGN luminosity function derived from the VVDS-sample;
- Finally, in Chapter 9 I will summarize the main results obtained through this work.

Chapter 2

Active Galactic Nuclei

Active Galactic Nuclei (AGN) are among the most powerful sources of energy in the Universe. They shine over the whole electromagnetic spectrum, from the radio to the gamma rays and in almost all of this huge energy range, AGN are the brightest sources in the sky.

As general definition, AGN are connected to energetic phenomena occurring at the central regions of galaxies that could not be attributed to stellar activity. A variety of objects are grouped under the name AGN: quasar, QSO, Seyfert galaxies, BL Lac, LINERS. The origin of these classification is substantially historical and not always reflects a real difference in the physical nature of the objects populating different classes. The main sub-classes of AGN are two: QSOs and Seyfert galaxies. AGN are divided in these groups depending on their luminosity.

2.1 History

Compared with the research on stars, the study of AGN is a relatively new field in astronomy. The first class of AGN discovered was Seyfert galaxies although they are the low luminosity class of AGN. This can be attributed to their morphology, in fact they appear morphologically extended so that their extragalactic nature has been more easily discovered. Quasars and QSOs have been instead discovered only 40 years ago because these objects are rare and appear in direct images like normal stars.

Seyfert galaxies: In 1908, working at Lick Observatory, Fath observed the spectra of "Spiral Nebulae". Although most of them showed an absorption line spectrum produced by the combined light of the galaxy stars, NGC 1068 displayed six bright emission lines. He identified the Hβ line and other five lines which were known from gaseous nebulae, but at that time the origin of these lines was unknown. Today we know that these lines are the "forbidden" lines [O II]λ3727*Å*, [Ne III]λ3869*Å*, [O III]λ4363*Å* and [O III]λλ4959, 5007*Å*. NGC 1068 was the first AGN discovered but not recognized. Up to 1943, twelve galaxies were known to show emission lines in their spectra. In that year, Carl Seyfert, studying the emission lines properties of six of these objects (Seyfert, 1943), reported that

some of them had very bright unresolved nuclei that were the source of striking broad emission lines produced by atoms in a wide range of ionization states. In this way, he realized that they were a special class of galaxies, known today as Seyfert galaxies. Later, Khachikian & Weedman (1974) defined two sub-classes of Seyfert galaxies, according to their spectral properties: (i) type–1 in which the Balmer lines are broader than the forbidden lines and (ii) type–2 in which the forbidden lines and Balmer lines have the same width.

Quasar and QSOs: At the end of fifties, the increasing number of radio sources discovered with radio telescopes introduces the problem of identifying them with sources already known in other wavelength ranges. In 1960 Thomas Matthews & Allan Sandage discovered that most of the radio sources present in the catalog 3C (*third Cambridge Catalogue of Discrete Radio Sources*) could be optically identified with stellar objects. Looking for the optical counterpart of the radio source 3C 48, they in fact found that, on photographic plates this object looked like a star, but with strange emission lines in the spectrum. This kind of spectrum, defined as *"weird"* by Sandage himself, was found again in 1963 in another radio source with stellar appearance (3C 273) by Matthews & Sandage. Since the physical nature of these objects was not understood, they were called *quasi stellar radio sources* (*quasars*).

The mystery was partly solved when Schmidt (1963) identified the lines observed in 3C 273 as Hydrogen Balmer lines severely redshifted (z=0.158). If this redshift was due to the Doppler effect, then 3C 273 would be receding from the earth at 14.6% of the speed of light. According to the Hubble's law [1], this places 3C 273 at a distance of about 630 Mpc; never before had been observed an object so far away. Since, at such distances, even the brightest normal galaxies would not be visible, this led to conclude that quasars had luminosities never seen before ($\sim$ 100 times larger than a bright spiral galaxy). Particular attention was immediately given to this class of objects and other similar objects were quickly discovered.

Subsequently, studies on this class of objects, based on different selection techniques, pointed out that most of the objects in this class did not have high radio luminosity. For this reason was introduced the term QSOs (*Quasi Stellar Objects*) referring only to their morphology. Quasars and QSOs are thus the same kind of objects discerned only by the intensity of their radio emission. Today both names are used without distinction to indicate the bright sub-class of AGN. In this manuscript we will refer them as QSO. The distinction based on the radio emission is now between *radio loud* and *radio quiet*. QSOs are defined as radio loud when their radio-to- optical flux ratio (R) exceed a certain value ($R > 10$, Kellermann et al. 1989). The remaining objects are classified as radio quiet. Only 10 to 20% of type–1 AGN are classified as radio-loud. They are also characterized

[1] given the Hubble's law ($v = H_0\, d$), the redshift in light coming from distant galaxies is proportional to their distance. The most recent calculation of the constant (H_0) yielded a value of 73.2 ± 3.1 km s^{-1} Mpc^{-1} (WMAP; Spergel et al., 2006)

by the presence of jets.

2.2 Properties of AGN

AGN are among the most powerful sources of energy in the Universe. They are characterized by a very large luminosity produced in a very small volume. The nucleus can be 100 or in some cases even 1000 times brighter than the host galaxy. In the optical band in fact, at high redshift, AGN appear as "quasi-stellar" sources while, at lower redshift and with high resolution observations, it is possible to distinguish the underlying host galaxy. The shape of the continuum emission of an AGN cannot be described by a thermal spectrum. It follows approximately a power-law over a wide range of frequencies due to a combination of synchrotron and Compton mechanisms. The broad-band Spectral Energy distribution (SED) can indeed be described by:

$$F_\nu = A\,\nu^{-\alpha} \tag{2.1}$$

where α is the power-law index, A is a constant and F_ν is the specific flux (i.e. per unit frequency interval), usually measured in units [erg s^{-1} cm $^{-2}$ Hz^{-1}][2]. Fits to QSO spectra over large frequency ranges yield spectral indices that are tipically in the range $0<\alpha<1$, but different value of α are found for different spectral ranges.

The UV-optical spectra of QSOs are distinguished by strong broad emission lines. The strongest observed lines are the hydrogen Balmer-series lines (H$\alpha\lambda$6563$\AA$, H$\beta\lambda$4861$\AA$ and H$\beta\lambda$4340$\AA$), hydrogen Ly$\alpha\lambda$1216$\AA$ and prominent lines of abundant ions (Mg IIλ2799$\AA$, C III]λ1909$\AA$ and C IVλ1549$\AA$). These lines appear in virtually all QSOs spectra, but depending on the redshift of the QSO, some of them may not be observable if they fall outside the spectral window of a particular detector.

A striking characteristic of most AGN is that they show a variability in their emission line and continuum in every wavebands in which they have been studied. This variation could be on different timescales, from months to days even as short as hours, decreasing to tens of seconds in X-ray. Optical continuum variability of QSOs was established even before the emission line redshifts were understood (e.g. Matthews & Sandage, 1963) and variability was one of the first properties of QSOs to be explored in detail (e.g. Smith & Hoffleit, 1963). From studying the continuum variability of these objects, it is known that the region where most of the energy of an AGN is produced is extremely compact, with a size of the order of light days or even less [3]. This was immediately perceived as a major problem, since a nucleus comparable in size to the Solar System is emitting hundreds of

[2] Specific fluxes, particularly in the UV and optical parts of the spectrum, are often measured per unit wavelength interval (i.e. in units of erg s^{-1} cm $^{-2}$ $\AA^{-1}$) rather than per unit frequency interval. The total flux measured in any bandpass is the same, of course, whether the band width is measured in frequency or in wavelength, so the relationship $F_\nu d\nu = F_\lambda d\lambda$ always tolds. The transformation between the two sistem is thus: $F_\lambda = F_\nu \left|\frac{d\nu}{d\lambda}\right| = A\left(\frac{c}{\lambda}\right)\ \frac{c}{\lambda^2} = A'\lambda^{\alpha-2}$

[3] Large variations in light output cannot occur on less than a light-crossing time; this time is related with the mass by: $t \geq R/c \geq 2\,G\,M/c^3 = 0.98\times10^{-5}(M/M_\odot)\,s$

times as much energy as the entire galaxy. Due to their low efficiency, nuclear fusion cannot explain this high energy output from such small regions. The only mechanism efficient enough to explain the observational properties of AGN is accretion of matter onto a compact object. To produce the observed luminosities, the mass of the central compact source must be of the order of 10^6 - 10^9 $M_\odot$ (see next Section). This range of masses excludes a neutron star as the accreting object, thus indicating the presence of a central Black Hole (BH) as responsible for the luminosities typically observed.

In this scenario, the black hole accretes matter from the inner region of the host galaxy; because the infalling matter possesses angular momentum, the flow is organized in a disk structure (the accretion disk) in which the matter falling toward the black hole loses angular momentum through viscous or turbulent torques. In many cases the disk flow is confined so closely to the orbital plane that its properties could be described to a first approximation, like a two-dimensional gas flow. Assuming the geometrically thin, optically thick disk model proposed by Shakura (1973), each element of the disk face radiates roughly as a blackbody and the total emission, extended from the optical to the X-ray band, is a convolution of blackbody spectra with different temperatures, emitted at different radii.

Summarizing, an AGN can thus be distinguished from a “normal” galaxy if, at least one of the properties described above and here listed are observed:

- Bright semi-stellar nucleus;
- High absolute nuclear luminosity;
- Non-thermal continuum;
- Broad emission lines;
- Variability of lines and continuum;
- Jets.

2.3 Mass of the central object

The most generally admitted interpretation given to the mechanism behind the huge amount of energy (up to 10^{48} erg s^{-1}) emitted from such a small volume (a few parsecs) is a ‘central engine’ that consists of a hot accretion disk surrounding a super-massive black hole. Energy is generated by gravitational infall of material which is heated to high temperatures in a dissipative accretion disk.

Since the gravitational force by the central mass M, acting on the gas falling onto the central engine, must balance or exceed the outward radiation force, one can link the

luminosity L emitted by the central engine to its mass M. Under the hypothesis of a spherical symmetry:

$$\frac{L\sigma_e}{4\pi cr^2} \leq \frac{GMm_p}{r^2} \tag{2.2}$$

where σ_e is the Thomson cross section and m_p the proton mass.

From relation 2.2, a lower limit on the mass of the hypothetical Super Massive Black Hole (SMBH) is obtained considering that the AGN is emitting light at the Eddington limit, i.e. the limit where the radiative pressure is balancing the gravitational potential:

$$M \geq 8 \times 10^5 L_{44} M_{\odot} \tag{2.3}$$

where L_{44} is the luminosity in units of 10^{44} erg s^{-1}, typical for a luminous Seyfert galaxy. For a typical quasar luminosity L$\simeq 10^{46}$ erg s^{-1}, a central mass of 10^8 $M_{\odot}$ is required.

2.4 Classification of AGN

Despite the common features described in the previous Section and despite the fact that basically the origin for the primary energetic output is the same in all AGN, a wide collection of different observational features has been observed. Depending on their spectral properties, their luminosity and the selection criteria, AGN have been classified in a large number of classes and sub-classes.

As already said in Section 2.1, historically, AGN have been divided in two different classes: QSOs and Seyfert galaxies. The only difference between these two classes of objects is the luminosity contrast between the compact central source and its host galaxy. When they were discovered, they were not recognized as parts of the same class of objects because the stellar appearance of QSOs did not suggest identification with galaxies, since only the not-resolved nuclear source was detected with the instrumentation available at that time. Nowadays, thanks to the improvement in camera resolution, we know that all QSOs with redshift up to 0.5 are embedded in the nucleus of a galaxy (Floyd et al., 2004). From the similarity of their spectra and most of their properties it is clearly established that Seyfert galaxies and QSOs form a single class of objects, whose properties vary continuously from the faintest Seyfert galaxies to the most luminous QSOs. The conventional limit following Schmidt & Green (1983) is M_B= -23: objects with $M_B <$ -23 are referred to as QSOs while objects with $M_B >$ -23 are called Seyfert galaxies.

The main division today, regarding both QSO and Seyfert galaxies is based on the optical emission lines. In the AGN spectra can be identified two principal systems of optical emission lines: Broad emission lines with typical *Full Width at Half Maximum* (FWHM)[4] $\gtrsim$ 2000 km s^{-1} and Narrow emission lines characterized by FWHM $\lesssim$ 1500 km s^{-1}.

[4]The *Full Width at Half Maximum* of a line is the width measured at half level between the continuum and the peak of the line. Given the relation $\Delta\lambda/\lambda = v/c$, the FWHM, expressed in km s^{-1} gives a measure of the gas velocity

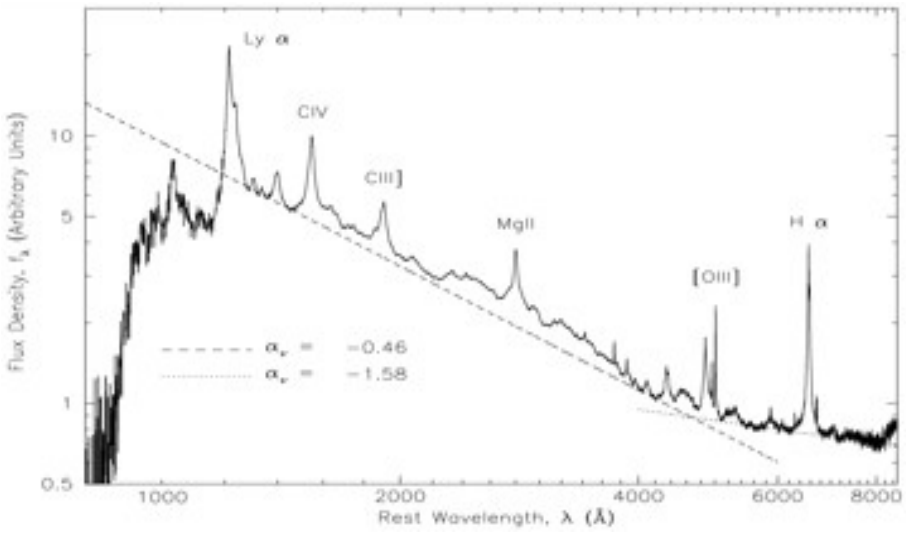

(a)

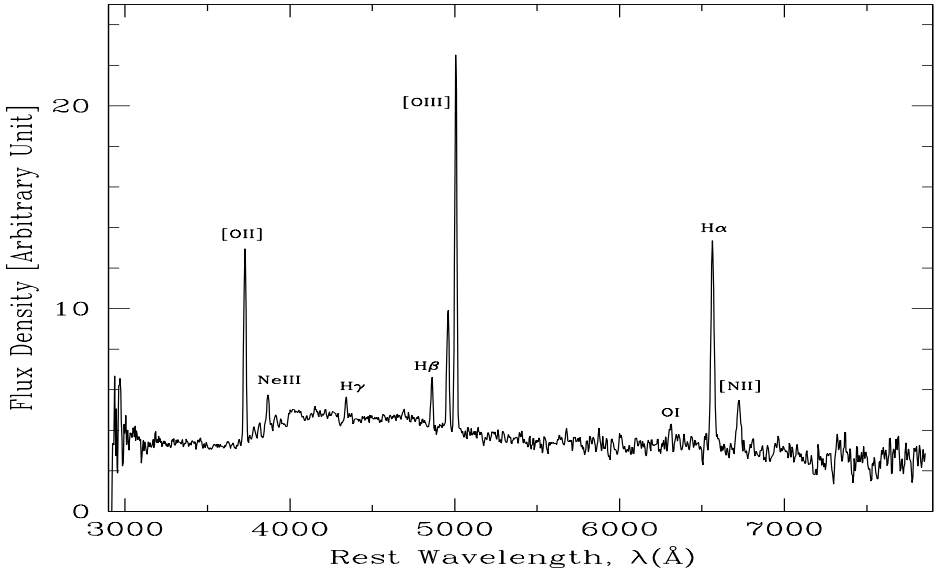

(b)

Figure 2.1. (a) Composite optical spectrum of type–1 AGN. Results from the SDSS (Vanden Berk et al., 2001). (b) Composite optical spectrum of type–2 AGN. Results from the VVDS (Contini et al., 2007 in prep.).

More details about the physical properties responsible for these two sets of lines are given in the next Section.

On the basis of the properties of the emission lines present in their spectra, AGN are classified as follow:

- **type–1** or **Broad Line AGN (BLAGN):** Objects with broad permitted lines and narrow forbidden lines. Their SED is dominated by the UV excess or *big blue bump*, while a second important component, the *IR bump*, emerges in the $\sim$ 1 - 300 μm region.

- **type–2** or **Narrow Line AGN (NLAGN):** Objects in which both permitted and forbidden line are narrow. Their SED does not show a strong UV excess, while the IR component is strongly enhanced.

Summarizing, AGN are divided in QSO and Seyfert galaxies on the basis of their bolometric luminosity and each class is then divided in type–1 and type–2 depending on the properties of their emission lines. Figure 2.1 show a typical spectrum of both classes. In this classification, two special cases can be pointed out: (i) The *Broad Absorption Line QSOs* (BAL), a sub-class of type–1 AGN with optical spectra characterized by strong absorption lines; and (ii) the *BL Lacertae* (BLLac) objects with strong non-thermal continuum and, if present, very weak emission lines.
Moreover, Osterbrock & Koski (1976) have shown that there is a continuum of AGN, between type–1 and type–2, covering a wide range of relative strength of narrow to broad components of the HI emission lines. These galaxies, with intermediate-type composite line profiles, have been called with intermediate numbers, e.g. type–1.2, –1.5, –1.8 AGN. In particular, type–1.8 AGN indicate that the broad Hα emission-line component is weak and that the broad Hβ component, although very weak, nevertheless can be seen directly on the spectral scan. On the contrary, type–1.9 AGN indicate objects in which, although the broad Hα is clearly evident and indeed is rather strong, broad Hβ cannot be detected (Osterbrock, 1981).

In this thesis I will present the properties of a sample of type–1 AGN, in which no distinction based on their luminosity has been done .

2.5 Unified Model

The classification of AGN is empirical and phenomenological. As widely explained in previous Sections, historically the term QSO has been used to refer to AGN of high luminosity whose emission completely overwhelmed that of the host galaxy (thus, these sources appeared as point sources in optical observations). Low luminosity AGN were (and still are) referred to as “Seyfert Galaxies”. However, evidence for any basic physical

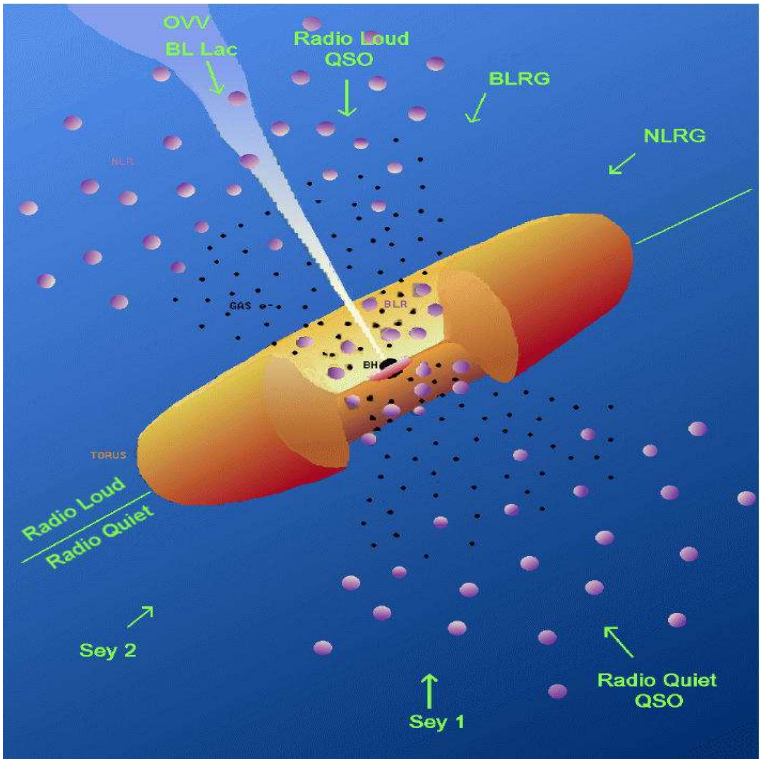

Figure 2.2. Unified Model of AGN according to Urry & Padovani (1995)

difference between these types of active objects has diminished through the years, nearly to the vanishing point. The simple picture of dividing AGN in type–1 and type–2 has been changed when the first type–2 AGN was observed in polarized light. Antonucci & Miller (1985) have found that in NGC 1068, classified as a type–2 Seyfert galaxy, also broad components in the hydrogen lines were present in polarized light. Based on this observations, Antonucci attributed this phenomenon to the scattering of broad-line emission above the poles of the dust torus (e.g. Antonucci, 1982; Antonucci & Miller, 1985) and indeed proposed a model that explains Seyfert-1 and Seyfert-2 as the same kind of objects seen at different inclination angles (Unified Model; Antonucci, 1993)
According to this model, the variety of AGN properties described above could be reconciled. This model postulates the presence of a central engine consisting in a SMBH surrounded by an accretion disk; a toroidal region consisting mainly in dust particles and two gas clouds regions with different radii and velocity dispersions. In the radio loud AGN is present also another component: jets. Figure 2.2 summarizes the different typologies of AGN justified by the Unified Model.

The toroidal structure around the central engine absorbs the radiation coming from the SMBH over a large solid angle. The bolometric luminosity emitted from the central engine is about 10^{42} - 10^{48} erg s^{-1}. The continuum emission comes from the central source and part of this radiation photoionizes the surrounding clouds.

Broad lines are generated inside a small region (from 10^{-2} pc to 10 pc) known as the *Broad Line Region* (BLR). The strong emission lines are formed in the BLR clouds and their broadening is interpreted as the effect of the high velocity dispersion in these clouds ($\gtrsim$ 2000 km s^{-1}). The absence of forbidden broad lines means that they are all collisionally suppressed and indicates densities of the order of 10^9 - 10^{10} cm^{-3}. The presence of high ionization lines in a warm medium (temperature $\sim 10^5$ K) is the signature of photoionization in the clouds. The energy source that drives the broad emission lines in AGN spectra is almost certainly photoionization by the continuum radiation from the central source, since the emission line fluxes vary strongly in response to changes in the continuum flux. Because the recombination lines are strongly variable, it can be concluded that a significant fraction of the BLR emission aries in clouds that are optically thick to ionize photons of energy $h\nu \geq 13.6$ eV. Those clouds are optically thick at UV wavelengths, so the fact that we are able to see the continuum emission from the central source indicates that their covering angle [5] is not very high (~ 0.1). The confinement of clouds in the BLR is under debate. It is possible that they are pressure confined by a surrounding intracloud hot medium or by their own magnetic field, or it is possible that clouds are short living system continuously created and destroyed during the AGN shining.

Narrow lines in AGN spectra are on the contrary, generated in a region extending from $\sim$ 10 pc up to 1 Kpc from the central source; the *Narrow Line Region* (NRL). The width of the lines generated in this region is interpreted as the effect of a velocity dispersion lower than in the BLR clouds ($\sim$ 1000 km s^{-1}, temperature $\sim 10^4$ K), while the presence of forbidden lines indicates electron densities low enough that many forbidden transition are not collisionally suppressed (10^2 - 10^6 cm^{-3}). The estimated covering angle is ~ 0.2. In this framework we can understand the observed properties of AGN. At polar observing angles we observe the inner regions and BLR clouds, so we will recognize a type–1 AGN. If we look through the toroidal structure all BLR emission is obscured and we see only the emission from the outer NLR clouds and the resulting object is a type–2 AGN. Concerning QSOs and Seyfert galaxies, the difference is due only to the bolometric luminosity of the source, with QSOs being the brighter part of the AGN population. In the framework of the Unified Model, a SMBH could be present at the center of each galaxy. When the SMBH accretes mass, it gives rise to an AGN, whereas when it is in a quiescent phase it can be only seen as a Massive Dark Objects (MDO). MDO are in fact often detected at the center of local galaxies (and also at the center of the Milky Way corresponding to the Sagittarius region) and are commonly interpreted as quiescent (maybe slowly accreting) SMBH, the relics of the past AGN activity in their host galaxies.

[5] The fraction of solid angle covered by clouds as seen from the central source

Chapter 3

AGN selection techniques

The ideal AGN selection technique would produce a candidate list that includes 100% of the objects of interest and contains no contaminating objects. In practice, usually one tries to maximize the level of completeness (missing as few true AGN as possible) while at the same time, minimize the number of contaminants.
AGN are observed in a large variety of forms and it is in practice not possible to make a census of the complete AGN population through a single survey.

To pre-select AGN candidates, it is possible to use the different characteristics of this class of objects (see previous Chapter): QSOs can be discovered through optical surveys by their ultraviolet colors or by their variability and lack of proper motion. Moreover we can use their radio, X-ray and infrared properties. Each of these criteria is based on a set of properties and therefore is focused on a specific sub-class of the AGN population. All survey techniques have redshift- and/or luminosity- dependent selection biases and they have to be quantified and taken into account in the statistical analysis of a sample. In the following paragraphs we will describe all these techniques with particular attention to the optical surveys.

3.1 Optical surveys

3.1.1 Optical selection of type–1 AGN

Ultraviolet-excess (UVX) and Multicolor surveys

Historically, the most common technique for QSOs selection has been the UV-excess in their continuum. This technique utilizes two of the main AGN peculiarities in the optical bands: (i) they appear morphologically point-like (not-resolved sources) and (ii) they show remarkably smaller U–B colors (i.e. large negative values) with respect to normal stars. This is often referred to as the “ultraviolet excess” (UVX) of quasars. Therefore, a natural selection of QSOs candidates can be performed on a photometric catalog by selecting all the point-like sources with bluer colors with respect to the normal stars.

A large scale UV-excess survey is the *Bright Quasar Survey* (BQS), which yielded to

Palomar-Green (PG) QSOs sample (Schmidt & Green, 1983). The candidate objects in this survey were selected from digital photografic plates according to the criterium U - B $<$ -0.44. The selection limit is normally chosen for efficiency (selecting objects that are probably QSOs) and not for completeness (selecting all the QSOs). Hence the selection limit is in no way related to any intrinsic property of the QSOs, but rather to the UV emission of stars: the color limit is chosen in order to reject the great majority of stars and thus have a high efficiency in QSO selection. In principle, a more relaxed color selection would find more QSOs, but the fraction of stars among the selected objects would be much higher, making the spectroscopic follow-up extremely time-consuming. The*Two-Degree Field QSO Redshift survey* (2Qz) is the largest UV-excess-selected survey, with an efficiency above 50% (Croom et al., 2004). It contains $\sim$ 20000 spectrocopically confirmed QSOs and is the second larger QSOs sample after the *Sloan Digital Sky Survey* (SDSS) quasar sample (see Table 3.1).

The drawback of this technique is a bias at low redshift against the objects for which the host galaxy is detected and resolved. A further complication of the UVX method is that colors are affected by emission lines as they are redshifted into and out of the filter passbands. This effect leads to a redshift dependence of the completeness. In particular, at $0.5 < z < 1.0$, the completeness can be around 70% but at redshift greater than 2.2, Lyα moves from the U passband to the B passband and the ultraviolet excess decreases to the point where the method is ineffective. Figure 3.1 shows an example of u – g vs g – r color diagram. The dashed region in both panels, indicates the star locus while the curve in the right panel corresponds to the evolution of the QSO colors with redshift. To extend the selection of QSO candidates also at redshift greater than 2.2, it is possible to use a combination of different filters. This method is known as multicolor technique.

The multicolor selection is an extension of the UVX technique by the addition of more passbands. By the combination of different colors it is possible to find QSOs at z$>$2, where the UVX method fails, on the basis of segregation from normal stars in the multicolor space. Candidate objects are in-fact selected because they are separated from the stellar locus of colors and not simply because of ultraviolet excess. Multicolor optical selections have been used in recent surveys, like the SDSS. Figure 3.2 is an example of this method used by Warren et al. (1991) to select QSO candidates.

Slitless spectroscopic surveys

This technique uses type–1 AGN characteristic broad lines as selection criterium. The use of slitless spectroscopy corresponds to look for emission line objects and since type–1 AGN have characteristic broad lines, this technique has a high efficiency to isolate AGN candidates in a wide range of redshifts. Using this method, low redshift QSOs, normally missed by other optical surveys, are selected since no discrimination against extended sources is imposed. As with other QSO survey methods, there are inherent limitations and

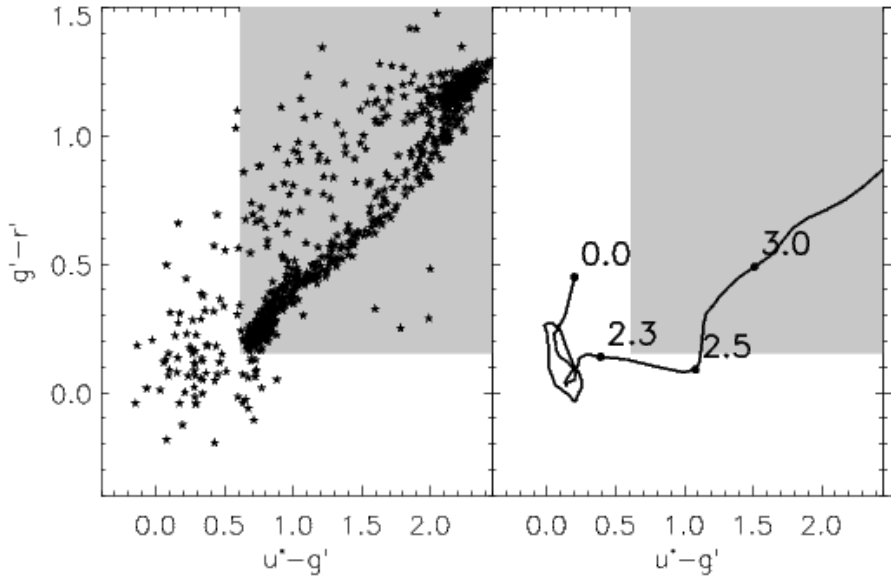

Figure 3.1. UVX method: example of u – g vs g – r color diagram. Shaded region corresponds to the star locus. The solid curve in the right panel shows the evolution of QSO colors with redshift.

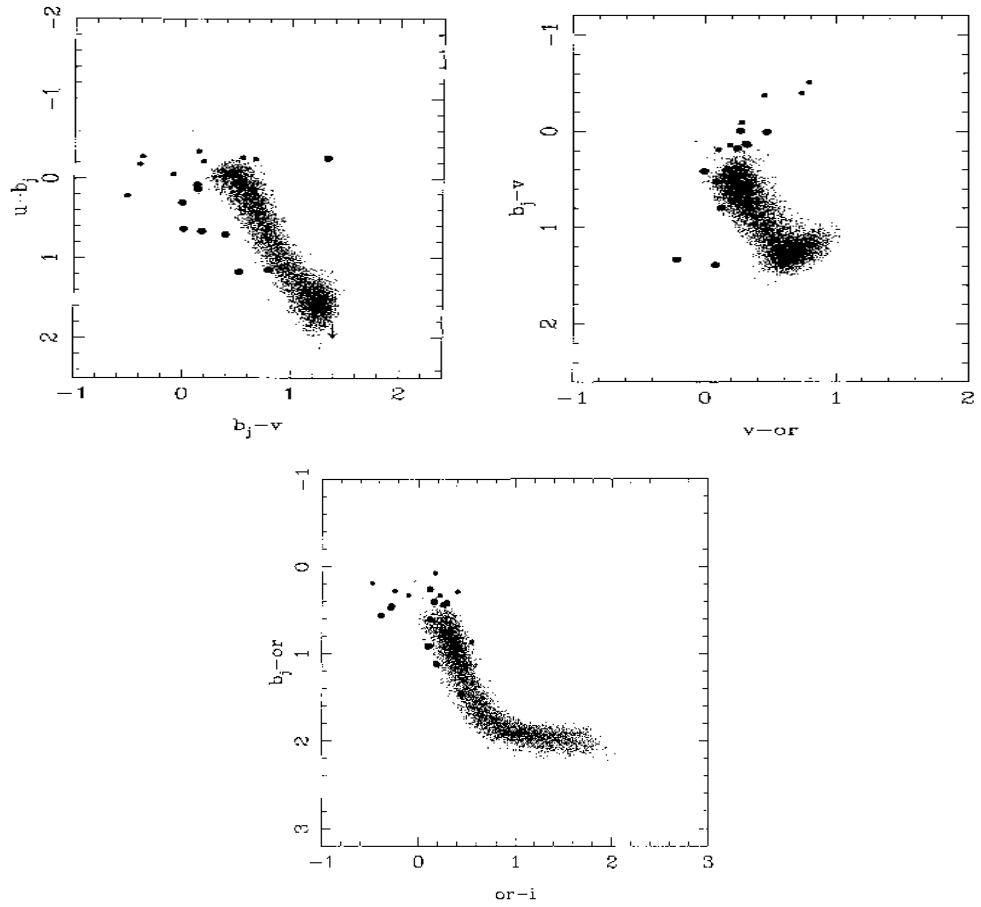

Figure 3.2. Multicolor method: examples of color-color diagrams used by Warren et al. (1991) to select a sample of QSOs candidates. Filled circles indicate spectroscopically confirmed quasar candidates.

selection biases that need to be understood. The basic problems with slitless spectroscopy are:

1.) The limiting magnitude of the survey cannot be reliably determined from the spectroscopic data. Identification of a QSO depends often on emission line identification, and the continuum flux of a particular faint QSO might lie well below the nominal detection limit without actually precluding detection of the source. A way around this difficulty is to obtain broad-band images of the field to define *a priori* a magnitude-limited sample.

2.) Slitless spectra have limited wavelength information, so sometimes there are few (or no) lines in the spectra. This is a particular problem at z$\simeq$1, when only Mg IIλ2798$\AA$ is redshifted into the optical spectrum.

3.) There is a clear bias in such surveys towards objects with the strongest lines relative to the continuum (Peterson, 1988). With photografic slitless spectroscopy, weak-lined objects are a particular problem because of their very low contrast.

This technique has been used for a long time. The first application of the slitless spectral technique to quasar was described by Hoag & Schroeder (1970) . As in the case of color surveys, spectroscopic surveys were originally carried out with photographic detectors and the data were inspected visually. Even when the detection limit and the overall efficiency were poorly known, these surveys led to important results, such as Osmer's (1982) recognition that the space density of very high-redshift (z $\gtrsim$ 3.5) QSOs must be extremely low. The basic data are now either digitized from photografic plates or obtained with CCDs, and thus sophisticated candidate-selection algorithms can be employed (e.g Hewett et al., 1985). Two recent illustrations of this technique are the *Large Bright Quasar Survey* (LBQS, Hewett et al. 1995) and the *Hamburg ESO Survey* (HES, Wisotzki et al. 2000).

Most of the slitless spectroscopic surveys, are realized applying several selection criteria in parallel. For the HES, for example, the authors used two sets of criteria: (1) color (identification of objects with blue continuum) and (2) spectral features detection.

Other selection methods

While slitless spectroscopy and color selection are probably the most efficient method in isolating QSO candidates, other methods deserve at least brief mention because they provide important checks on the principal techniques.

Variability: Various classes of AGN show different variability properties: the variations could vary from less than 0.5 mag. to more than 1 mag. on timescales from days to months. However, it seems that all QSOs are variable if observed on the scale of few years,

and this distinguish them from most stars. Identification of candidates on the basis of variability has proven to be quite effective when performed on a sufficiently large number of observations spaced over many years. This method is usually used in combination with the multicolor method (Cimatti et al., 1993; Rengstorf et al., 2004) since, even if it is time-consuming, it allows to discover QSOs that would have been missed by the other selection criteria.

Proper motion: Proper motions were initially used by Sandage & Luyten (1967) to identify white dwarfs among their blue objects. Kron & Chiu (1981) pointed out that the absence of proper motion can be used to detect compact extragalactic objects with no bias concerning spectral properties of the objects. With this method it is possible to detect all QSOs missed by the other methods, like QSOs that do not show the UV excess (missed by the UVX method) or without strong emission lines (missed by the slitless spectroscopic surveys). Unfortunately, this research is quite complex because it requires to observe two or more times the same field in different years. Moreover, stars with low tangential velocity could be misclassified as QSO candidates.

This method is in general used in combination with other selection criteria (e.g. with variability; Brunzendorf & Meusinger, 2002), to give an independent handle on their completeness function.

3.1.2 Optical selection of type–2 AGN

Type–2 AGN are more difficult to select with respect to type–1 AGN since their spectra show permitted and forbidden lines with similar width and can be confused with HII region-like galaxies.

The HII-region-like galaxies have emission-line spectra similar to those of HII regions (Huchra, 1977) and contain gas that is photoionized by hot stars. The most luminous objects of this type with the strongest emission lines are called starburst galaxies (Weedman et al., 1981). The fundamental difference, which distinguishes Seyfert galaxies and HII-region galaxies, is based on the mechanism by which emission lines are produced. In the HII galaxies, the gas is photoionized by young, hot OB stars, whereas in the AGN, the ionizing energy is supposed to come from accreting material around a SMBH and the ionizing energy spectrum takes the form of power law continuum.

Another class of narrow-emission line AGN is made up of low-ionization nuclear emission-line region (LINERs) (Heckman, 1980). Their spectra include strong low-ionization nuclear emission line such as [O I]$\lambda 6300\mathring{A}$ and [S II]$\lambda\lambda 6716, 6731\mathring{A}$ showing a wider range of ionization stages than the emission-line spectra produced in HII region. At present it seems most likely that their ionization is due primarily to “power law” continua similar to those responsible for the emission-line spectra of type–2 AGN.

The standard method used to distinguish between this classes of objects is based on

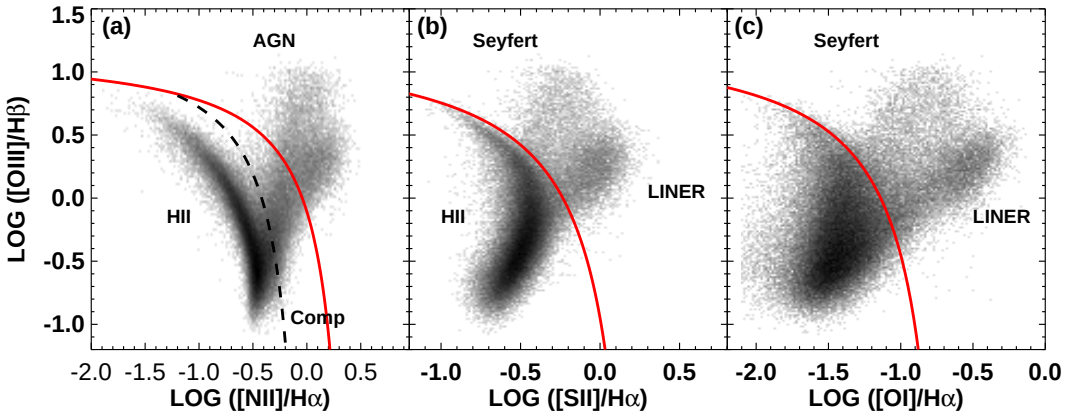

Figure 3.3. Example of standard diagnostic diagrams for galaxies of the Sloan Digital Sky Survey (Kewley et al., 2006)

diagnostic diagrams using line ratios ([N II]λ6583$\AA$/Hα, [S II]$\lambda\lambda$6716, 6731$\AA$/Hα and [O III]λ5007$\AA$/Hβ) to determine the main ionizing source responsible for the emission-line spectrum: photoionization by hot and massive stars (HII regions) or non-thermal continuum from an accretion disc around a BH (AGN). This classification, firstly defined by Veilleux & Osterbrock (1987), has been revised by Kewley et al. (2001; 2006) using new photoionization models. This new method may provide a more objective classification between star forming galaxies and AGN and is presented in Figure 3.3.

Since these models cannot be used at higer redshift, where Hα [N II]λ6583$\AA$ and [S II]$\lambda\lambda$6716, 6731$\AA$ are out of the observed range or in low resolution spectra, where Hα and [N II]λ6583$\AA$ are not well separated, Rola et al. (1997), and Dessauges-Zavadsky et al. (2000) proposed new classification criteria based on only "blue" emission line (e.g. [O III]$\lambda\lambda$4959, 5007$\AA$, [O II]λ3727$\AA$ and Hβ from Dessauges-Zavadsky et al. (2000) classification).

3.2 Radio surveys

Historically, quasars were discovered for the first time thanks to their radio emission. Thus, this property has been largely used to select quasars sample, even if only a small percentage of AGN show radio emission.

In 1943 April the "amateur" radio astronomer Grote Reber began the first systematic survey in the radio band, providing the first image of the Universe outside the traditional optical window (Reber, 1944).

Today, the two largest radio survey are the *NRAO VLA Sky Survey* (NVSS) and the *Faint Images of the Radio Sky at Twenty-cm survey* (FIRST) (Becker et al., 1995; Condon et al., 1998).

Using the VLA FIRST survey combined with the Automated Plate Measuring Facility

(APM) optical catalog, a relatively large ($\sim$ 1000) radio-selected sample of optically bright quasars has been constructed (the First Bright Quasar Sample - FBQS). Both radio-loud and radio-quiet QSOs have been detected with this survey and moreover a large population of objects of intermediate radio loudness has been found.

Radio surveys are very important in selecting QSO candidates because the radio wavelengths are not affected by dust extinction. It is indeed possible to select, in the radio band, AGN whose optical emission is extinguished by dust and thus to construct a complete radio selected sample free of optical color pre-selection biases.

3.3 X-ray surveys

The study of AGN in the X-ray band has really began in 1978 through deep *Einstein* observations that allowed to resolve $\sim$25% of the 1 – 3 keV Cosmic X-Ray Background (CXRB) into discrete sources, a large fraction of which were identified as AGN (Giacconi et al., 1979).

The CXRB was discovered by Giacconi et al. (1962) in a rocket flight originally designed to detect X-ray emission from the Moon. The data showed a diffuse X-ray emission of approximatively constant intensity from all directions observed during the flight. The discrete nature of the CXRB became clear only when sensitive, high-angular-resolution imaging X-ray observations with Wolter telescopes [1] became possible.

Deep 0.5 – 2 keV surveys with *ROSAT* were, for the first time, able to resolve the majority ($\sim$75%) of the soft CXRB into discrete sources (e.g. Hasinger et al. 1993, 1998) and extensive optical follow-up spectroscopy identified the bulk of these sources as AGN (McHardy et al., 1998; Schmidt et al., 1998; Zamorani et al., 1999; Lehmann et al., 2001), demonstrating that at least at 0.5 – 2 keV, the CXRB is predominantly due to accretion onto SMBH, integrated over the cosmic time.

X-ray emission is indeed one of the most common and distinctive feature of AGN and thanks to *ROSAT*, and more recently to the *Chandra* and *XMM* missions, the selection of AGN in the soft 0.5 – 2 keV band yields the highest surface densities of AGN with respect to any other wavelength ($\sim$ 780 - 870 deg^{-2} from the deep *ROSAT* surveys (Miyaji et al., 2000) and even larger densities in the deeper Chandra images (Giacconi et al., 2002; Alexander et al., 2003, respectively for Chandra Deep Field North (CDFN) and Chandra Deep Field South (CDFS)).

Surveys at higher energy, were pioneered using *ASCA* (2 – 10 keV) and *BeppoSAX* (5 – 10 keV). These observations resolved 20-30% of the 5 – 10 keV CXRB (e.g. Comastri et al. 2001). The resolved fraction of the 2 – 10 keV hard X-ray background with the CDFN (Giacconi et al., 2002) and CDFS (Alexander et al., 2003) is as large as 80% (Worsley et al., 2005), and intense effort of optical identification of these faint sources is

[1] Aplanatic system of grazing incidence mirrors designed by Wolter (1952), that is free of both spherical aberration and coma.

leading to samples of reasonable statistics with good completeness (Hasinger et al., 2005). Despite this situation, the picture of the AGN population and evolution is not as clear as expected.

The major advantage related to X-ray selected samples consists on their ability to select at the same time type–1 AGN and type–2 AGN. Moreover, deep X-ray surveys efficiently select AGN less luminous than those found in optical surveys out to high redshift.

An interesting result of X-ray surveys is that while type–1 AGN constitute the major population of bright sources, while at fainter luminosities type–2 AGN dominate (Barger et al., 2005). Only a few examples of bright type–2 AGN were uncovered until recently by deep soft X-ray observations (e.g. Norman et al., 2002). This can be due to the large absorption column densities inferred for these objects ($N_H > 10^{23-24}$) that makes them extremely difficult to detect or identify in soft X-ray surveys.

3.4 Infrared surveys

In this wavelength range, AGN are selected thanks to their infrared (IR) excess due to thermal emission coming from the dust heated by the optical and UV fluxes emitted in the AGN inner regions.

The first IR survey, (IRAS launched in 1982) led to a huge catalog of IR sources ($\sim$ 250000) of which less than 1000 seem to be QSO.

Today, the Spitzer mission is providing the possibility to select AGN from their mid-infrared emission (e.g. Lacy et al., 2004; Sajina et al., 2005) and the first results suggest the presence of a significant population of obscured AGN partially missed in X-rays (Martínez-Sansigre et al., 2005; Treister et al., 2006).

The main recent AGN surveys are summarized in Table 3.1.

In this thesis I will present the properties and the evolution of an optically selected type–1 AGN sample. No pre-selection method has been used for these objects; they are selected from the VIMOS-VLT Deep Survey (see next Chapter), only on the basis of their spectra.

Table 3.1. Example of recent AGN surveys. The work presented in this thesis is based on the VVDS-sample.

Survey	Selection technique	Number of AGN$^{(*)}$	Limiting flux	Redshift range	Reference
2Qz	u, b_j, r + morphology	23 338	$b_j < 20.85$	$z \lesssim 2.3$	Croom et al. (2004)
SDSS	u, g, r, i, z + radio + morph.	76 483	$i^* < 19.1$ for $z \lesssim 3$ $i^* < 20.2$ for $z \gtrsim 3$	$z \lesssim 5.8$	Richards et al. (2002)
COMBO-17	SED fitting, 17 filters: UV to near-IR	192	$R < 24$	$1.2 < z < 4.8$	Wolf et al. (2003b)
LBQS	SS: continuum + EL + morph.	1055	$B_J \lesssim 18.5$	$0.2 \leq z \leq 3.4$	Hewett et al. (1995)
HES	SS: continuum + EL	415	$B_J \lesssim 17.5$	$z < 3.2$	Wisotzki et al. (2000)
CFRS	I-band flux limited	6	$I_{AB} < 22.5$	$z < 5$	Schade et al. (1996)
VVDS	I-band flux limited	56	$I_{AB} < 22.5$	$z < 5$	Gavignaud et al. (2006)
	I-band flux limited	74	$I_{AB} < 24$	$z < 5$	
CDFS-N CDFS-S	Soft X-ray	~ 400	$F_{0.5--2keV} > 3.10^{-14}$ erg cm^{-2} s^{-1}	–	Alexander et al. (2003) Barger et al. (2003)
HELLAS	Hard X-ray	38	$F_{5--10keV} > 3.10^{-14}$ erg cm^{-2} s^{-1}	–	Fiore et al. (1999) La Franca et al. (2002)
FBQS	radio + blue color + optical morphology	957	$S_{1.4GHz} \geq 1$ mJy, $R < 17.8$ and $R < 18.9$	$z < 4$	White et al. (2000) Becker et al. (2001)
PQJ	radio flat spectra	379	$S_{2.7GHz} \geq 0.25$ Jy	$z < 4$	Jackson et al. (2002)

(*) Number of AGN with an optical spectral identification (except in the case of COMBO-17 sample).
- SS: Slitless spectroscopy;
- EL: Emission lines.

Chapter 4

The VIMOS-VLT Deep Survey

Researches on the physical nature of a class of objects can be divided in two different areas: (i) the study of the physical properties of the single objects and (ii) the statistical analysis of samples of objects.

The first area is dedicated to determine the physical condition of single objects, and in this sense, the attention is focused on the particular physical processes that are taking place in them. The aim of the second area is instead the study of the statistical properties of a class of objects looking for correlations between different observational properties (like the surface density as a function of magnitude and the cosmological evolution). The observational techniques related to the latter kind of research are the surveys. In these studies, it is important to have large samples as complete as possible so that the derived properties can be considered general for that specific class of objects. For this reason, the surveys have to cover large areas of the sky and reach faint limiting magnitudes with a high degree of completeness. These two characteristics, which are linked to the used instrumentation (e.g. limiting magnitudes, field of view and spectral resolutions), cannot be optimized at the same time. There are indeed wide surveys covering large portion of the sky at bright limiting magnitudes that allow to study, with large samples, the statistical properties of the local Universe, and deep surveys on restricted areas with faint limiting magnitude to follow the evolution with redshift of such properties.

Today, the main optical spectroscopic surveys of relatively bright galaxies are the *two degree field Galaxy Redshift Survey* [1] (2dFGRS, Colless et al. 2001) and the *Sloan Digital Sky Survey*[2] (SDSS, Abazajian et al. 2003). The 2dFGRS is designed to measure redshifts for approximatively 250000 galaxies using the 2dF multifibre spectrograph on the Anglo-Australian Telescope. The survey covers 2000 deg^2 over two declination strips (one in the southern and the other in the northern Galactic hemisphere) and has a median depth of z=0.11. The source catalog used to select the targets is a revised and extended version of the APM galaxy catalog, and the targets are selected at magnitudes brighter than b_j = 19.45. On the contrary, the SDSS consists of a photometric survey in five bands

[1] http://mso.anu.edu.au/2dFGRS/

[2] http://www.sdss.org/

(u, g, r, i, z) that is used for the target selection in the following spectroscopic survey. The Data Release 3 spectroscopic catalog (Abazajian et al., 2005) consists of 528640 objects selected from 4188 deg^2 of the imaging area. The main galaxy sample is limited to r = 17.77 while the QSO sample to i = 19.1 (for z $<$ 3 candidates) and i = 20.2 (for higher redshift candidates). The resulting median depth of the SDSS galaxy sample is z $\simeq$0.1.

The 2dF and the SDSS are indeed mapping the distribution and establishing the properties of several hundreds of thousands of galaxies in the local Universe (up to z $\sim$ 0.3).

The **VIMOS-VLT Deep Survey** (VVDS)[3] aims to be the complementary deep and high redshift counterpart of the massive efforts undertaken with the 2dF and SDSS surveys

4.1 Survey goals

The aim of the VVDS is to probe the Universe at increasingly higher redshifts to establish the evolutionary sequence of galaxies, AGN, clusters and large scale structures, and provide a statistically robust dataset to challenge current and future models, from one single dataset.

In particular, the main astrophysical goals are:

- study the formation and evolution of galaxies up to z $\sim$ 5;
- study the evolution of large scale structures over 100 h^{-1} Mpc up to z $\sim$ 5;
- measure the properties of galaxy biasing using together the dark matter (from weak lensing) and the galaxy distribution;
- identify new high redshift clusters of galaxies;
- study high redshift Lyman-break galaxies with $3.5 < z < 4.2$, using multi-color data set of the optical and U-band survey.
- identify faint AGN and study their evolution.

4.2 Survey strategy

The science goals, listed above, require a large number of objects over large and deep volumes. For this reason, the VVDS survey consists of two main parts: the *VVDS-Deep Survey* which is a magnitude limited survey reaching a limiting magnitude of $I_{\rm AB}$ = 24.0 in 2 fields (the VVDS-02h field and the *Chandra Deep Field South* (CDFS)), and the *VVDS-Wide Survey* which consists of objects selected in 4 fields down to $I_{\rm AB}$ = 22.5.

[3] http://www.oamp.fr/virmos/vvds.htm

Field	α_{2000} center	δ_{2000} center	b	l	E(B-V)	field size (I-band)
0226-04 “wide”	$02^h24^m39.75^s$	-04°30 ’00 ”	-58.0	172.0	0.027	5.40
0226-04 “deep”	$02^h26^m00^s$	-04°30 ’00 ”	-58.0	172.0	0.027	1.45
1003+01	$10^h03^m39.00^s$	+01°54 ’39 ”	42.6	237.8	0.023	4.14
1400+05	$14^h00^m00.00^s$	+05°00 ’00 ”	62.5	342.4	0.026	4.32
2217+00	$22^h17^m50.40^s$	+00°24 ’27 ”	-44.0	63.3	0.062	3.60

Table 4.1. Survey fields

The VVDS survey is indeed based on a simple selection function: the sample is selected only on the basis of I-band magnitude. The purely magnitude-limited selection of spectroscopic targets was carried out from an imaging catalog based on deep photometry, performed for this purpose. The CDFS is based on the EIS *I*-band catalog described in Arnouts et al. (2001).

4.2.1 The VVDS multi-wavelength imaging survey

The imaging survey has been used to select the targets for the spectroscopic survey. The survey fields have been selected with the following criteria:

- along the celestial equator ($|\delta| < 5°$) to allow for visibility from northern and southern hemisphere observatories;
- galactic latitude higher than b =40°;
- low cirrus absorption as measured from the DIRBE maps available when the survey started in 1998;
- visibility of at least two fields at any time of the year to fill observing nights.

The selected fields are listed in Table 4.1 and their position in the dust sky map is shown in Figure 4.1.

The wide photometric survey covers 12 deg^2 in three high galactic latitude fields, each 2x2 deg^2 large: VVDS-1003+01, VVDS-1400+05, and VVDS-2217+00. The deep photometric survey covers a 1.3 x 1 deg area in the VVDS-0226-04.

The imaging survey consists of observations in four bands, B, V, R and I and it has been designed to reach a limiting magnitude I_{AB} = 24.5 in all the area surveyed, with a smaller area (1.3 deg^2 in the 02h field) at I_{AB} = 25.0.

The B, V, R and I observations were performed from November 1999 to October 2000 at the 3.6 m Canada-France-Hawaii Telescope (CFHT), with the CFH12K wide field mosaic camera. The depth of this imaging survey is at least one magnitude deeper than the limiting magnitudes of the spectroscopic survey. This ensures that the imaging survey

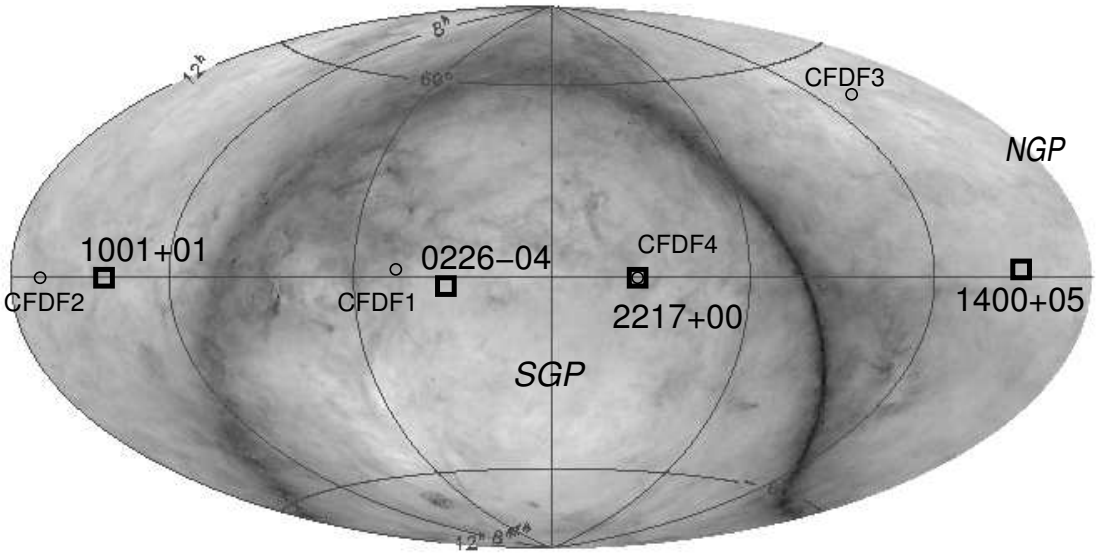

Figure 4.1. Positions of the 4 VIRMOS fields on a dust map (Schlegel et al., 1998) of the sky (Aitoff projection in equatorial coordinates). The open squares are the center positions. One can see that the four fields are visible from CFHT as well as the ESO Paranal and the ESO La Silla observatories and are separated by at least 4 hours, making the observations optimally spread over the nights and over the year. The square size are not exactly scaled according to the true field size ($2^\circ \times 2^\circ$) to ease visualization. For comparison the open circles indicates of center position of the CFDF fields (McCracken et al., 2001). The CFDF field sizes are 16 times smaller than the VIRMOS. The dust map was generated using the advanced Skyview virtual observatory tools (`http://http://skys4.gsfc.nasa.gov/`).

doesn't introduce any bias in the galaxy samples selected for the spectroscopic survey. Part of the deep field has been observed in additional bands: U (Radovich et al., 2004), J and K (Iovino et al., 2005), u^*,g',r',i',z' from the Canada-France-Hawaii Legacy Survey (CFHTLS) [4] as well as in radio (1.4 GHz) on the VLA (Bondi et al., 2003), X-ray with XMM (Pierre et al., 2004), and UV with Galex (Morrissey et al., 2005).
For a detailed description of the photometric catalog I refer the reader to Le Fèvre et al. (2004).

4.2.2 The VVDS spectroscopic survey

Spectroscopic observations were performed with the VIsible Multi Object Spectrograph (VIMOS) installed on Melipal, the third 8-meter telescope at Paranal Observatory. The VIMOS instrument consists of 4 quadrants covering a total field of view (a pointing) of ~ 218 arcmin^2 (each quadrant being $\sim 7 \times 8$ arcmin^2). It allows to observe with about 600 slits simultaneously at a spectral resolution of $R \sim 230$ (see Figure 4.2).

The area covered by the Epoch One VVDS spectroscopy is $\sim$0.6 deg^2 in the deep fields and $\sim$1.1 deg^2 in the wide fields (see column 5 in Table 4.2) and the corresponding numbers of spectra are 11564 and 9440 respectively. The target sampling rate, (i.e.

[4] www.cfht.hawaii.edu/Science/CFHLS

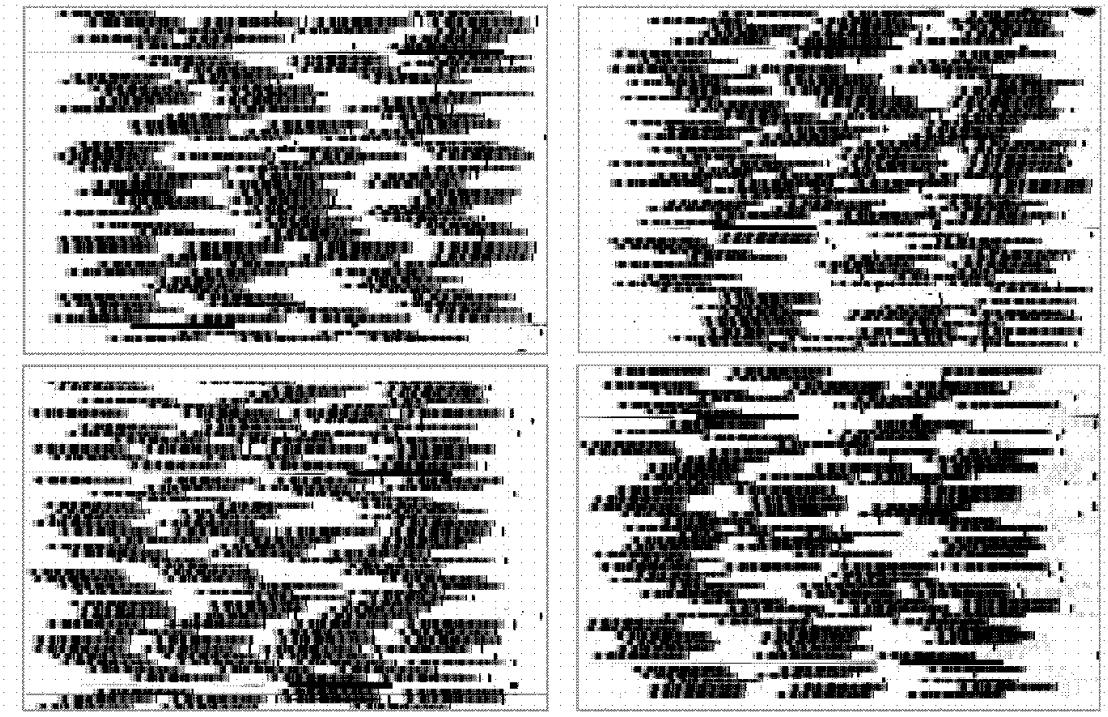

Figure 4.2. Typical layout of spectra in the 4 quadrants of a VVDS-Wide pointing; more than 550 spectra are observed on average (Le Fèvre et al., 2005c)

the ratio of selected objects for spectroscopy to the total number of objects down to the respective spectroscopic flux limits) is $\sim 25\%$ in both the wide and the deep surveys (see column 4 in Table 4.2).

Spectra are obtained using the VIMOS-LRRED grism which covers the wavelength range 5500 – 9500Å with a 7Å/pixel dispersion. The slit width was fixed to 1 arcsec, providing a sampling of 5 pixels per slit and a spectral resolution of $R \sim 230$. The total integration time is 4.5 hours per mask in the deep fields and 50 minutes in the wide fields.

The measured median signal-to-noise ratio (S/N) per resolution element at our limiting magnitudes is 4 in both the deep and wide fields.

4.2.3 Target selection

The VVDS spectroscopic targets are selected only on the basis of I-band magnitude; the resulting sample is indeed free of biases introduced by pre-selection methods. However, to get a fully unbiased spectroscopic sample one would pick objects at random from the input catalog. Such a procedure would ensure randomness, but would not provide spectra at the optimal rate for a given observing time. For this reason a special target selection algorithm (*Slit Positioning Optimization Code* - SPOC), was developed with the aim of optimizing the use of spectroscopic follow-up time given the constraints of the VIMOS optical and mechanical layout (Bottini et al., 2005). In this optimization process, however,

Table 4.2. Summary of the VVDS Epoch-1 spectroscopic fields.

Field	Survey Mode	limiting magn. I_{AB}	TSR*	$\mathcal{A}$** [deg^2]
VVDS-0226-04	deep	24.0	25%	0.48
VVDS-1003+01	wide	22.5	26%	0.33
VVDS-2217+00	wide	22.5	22%	0.81
VVDS-CDFS	deep	24.0	23%	0.13

* Target Sampling Rate: Fraction of objects in the photometric catalog inside our targeted area $\mathcal{A}$ which have been spectroscopically observed.

** Geometrical area in deg^2 of the spectroscopic first epoch data which are used in this work.

two biases are introduced:

(i) Objects with a small projected size along the slit are slightly favored for spectroscopic selection, resulting in a bias against more extended objects.

(ii) The distribution of selected targets is not isotropic as SPOC prevents the observation of target closer than 2 arcmin, perpendicular to the slit direction to avoid surperpositions of spectra.

4.2.4 Spectral classification

Data reduction was performed homogeneously by the VIMOS team using the VIPGI software which was developed specifically for the VVDS survey (Scodeggio et al., 2005). The redshift of each object has been then classified on the basis of the confidence level on it. In particular:

- **flag 4:** a completely secure redshift, obvious spectral features in support of redshift measurement;
- **flag 3:** a very secure redshift, strong spectral features;
- **flag 2:** a secure redshift measurement, several features in support of measurement;
- **flag 1:** a tentative redshift measurement, weak spectral features including continuum shape;
- **flag 0:** no redshift measurement, no apparent features;
- **flag 9:** one secure single spectral feature in emission;

For each of these flags, a probability to be correct can be assigned from various analyses (e.g using the repeated observations of the same objects and photometric redshift up to $z \sim 1$). We estimated that the probability of a solution, to be the correct one is $53 \pm 5\%$, $81 \pm 3\%$, $94 \pm 3\%$ and 100%, for galaxies with flags 1, 2, 3 and 4 respectively.

These flags are replicated for broad line AGN adding 1- before the flag number (11, 12, 13, 14 and 19). We will better discuss the AGN flags in the next Chapter.

Examples of VVDS spectra with flags from 1 to 4 are reported in Figures 4.3, 4.4, 4.5 and 4.6 corresponding respectively to the redshift range $0 < z \leq 0.7$, $0.7 < z \leq 1.3$, $1.3 < z \leq 2.2$ and $2.2 < z \leq 5$.

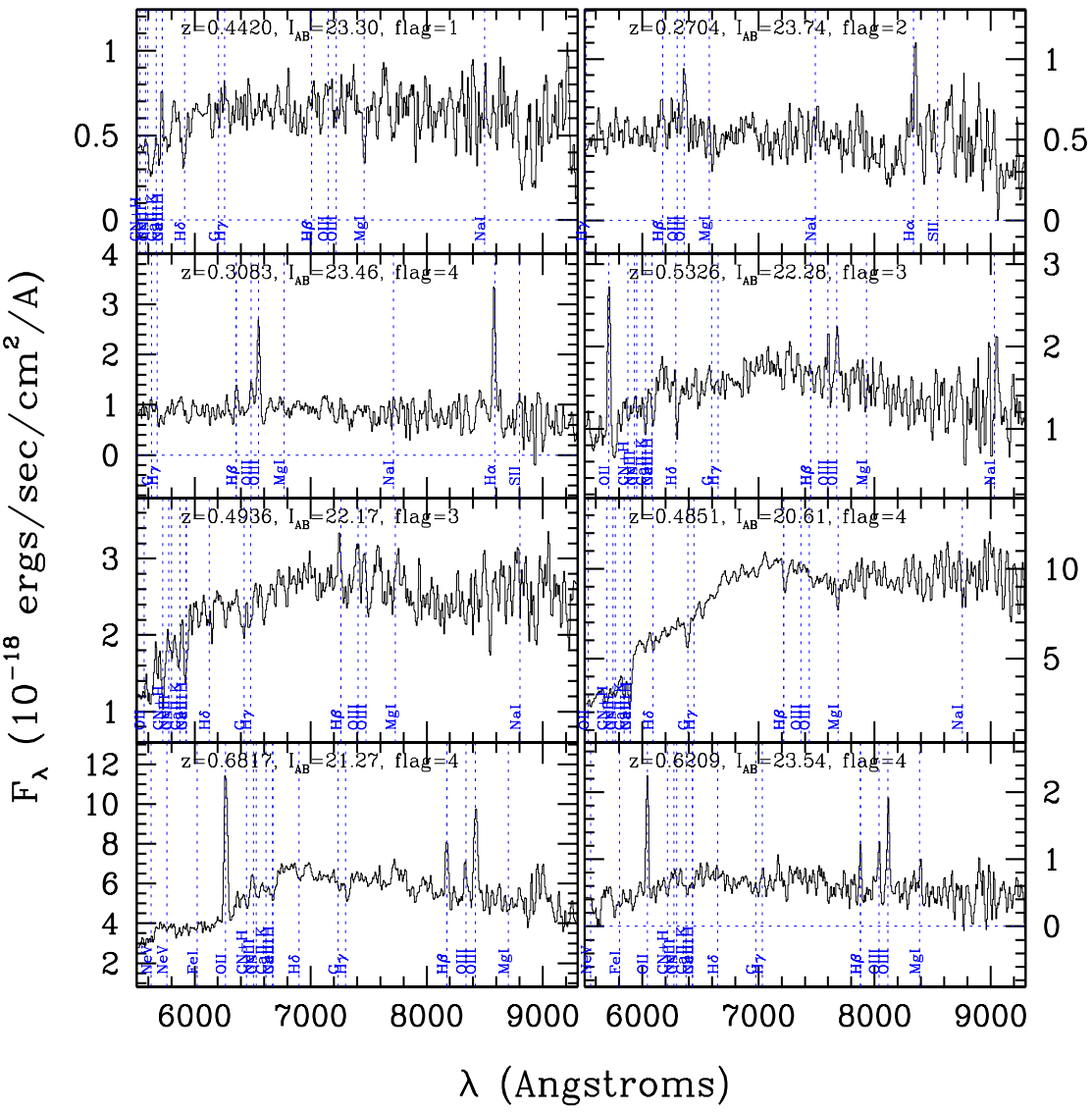

Figure 4.3. Examples of VVDS spectra in the range $0 < z \leq 0.7$.

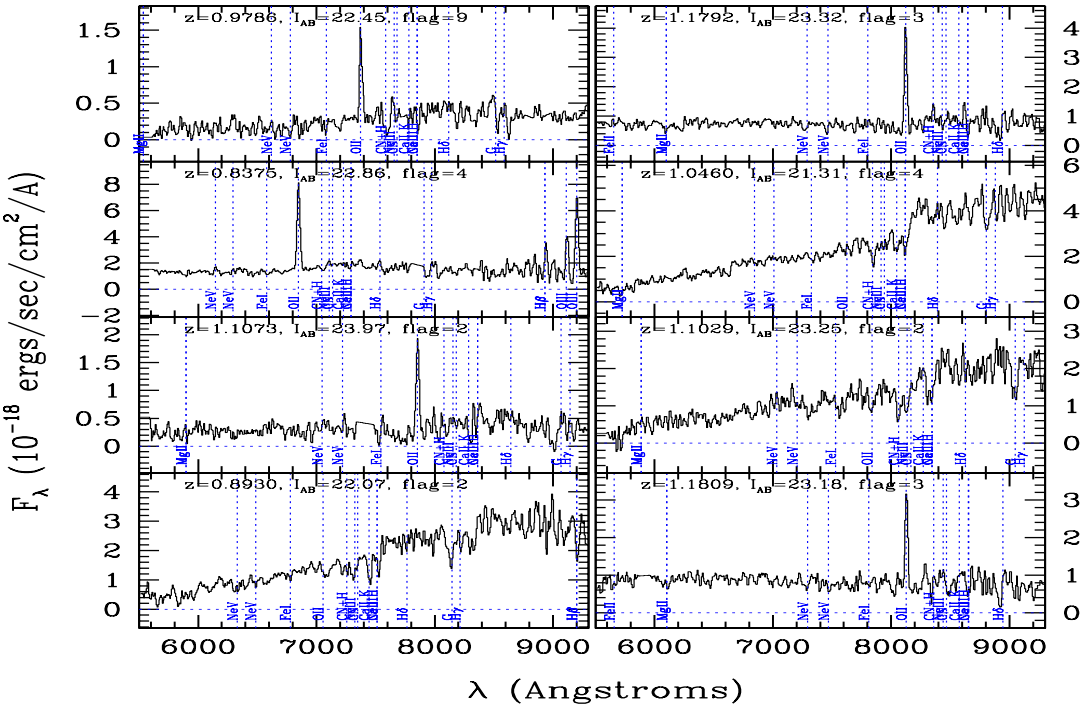

Figure 4.4. Examples of VVDS spectra in the range $0.7 < z \leq 1.3$.

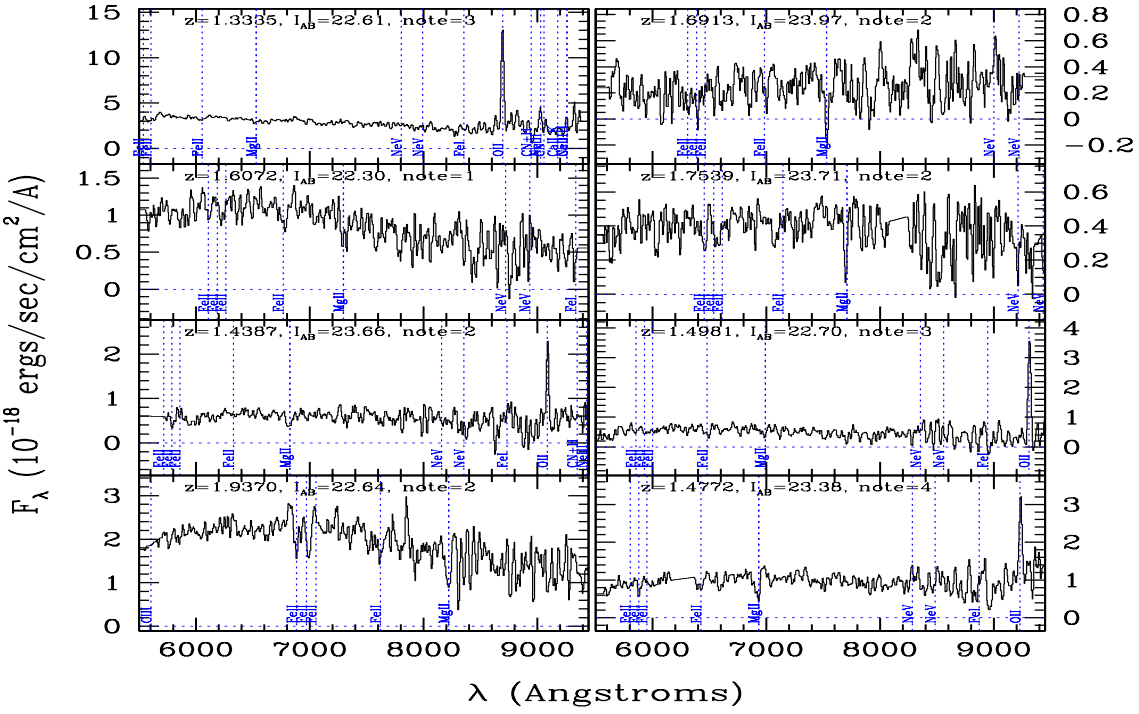

Figure 4.5. Examples of VVDS spectra in the range $1.3 < z \leq 2.2$.

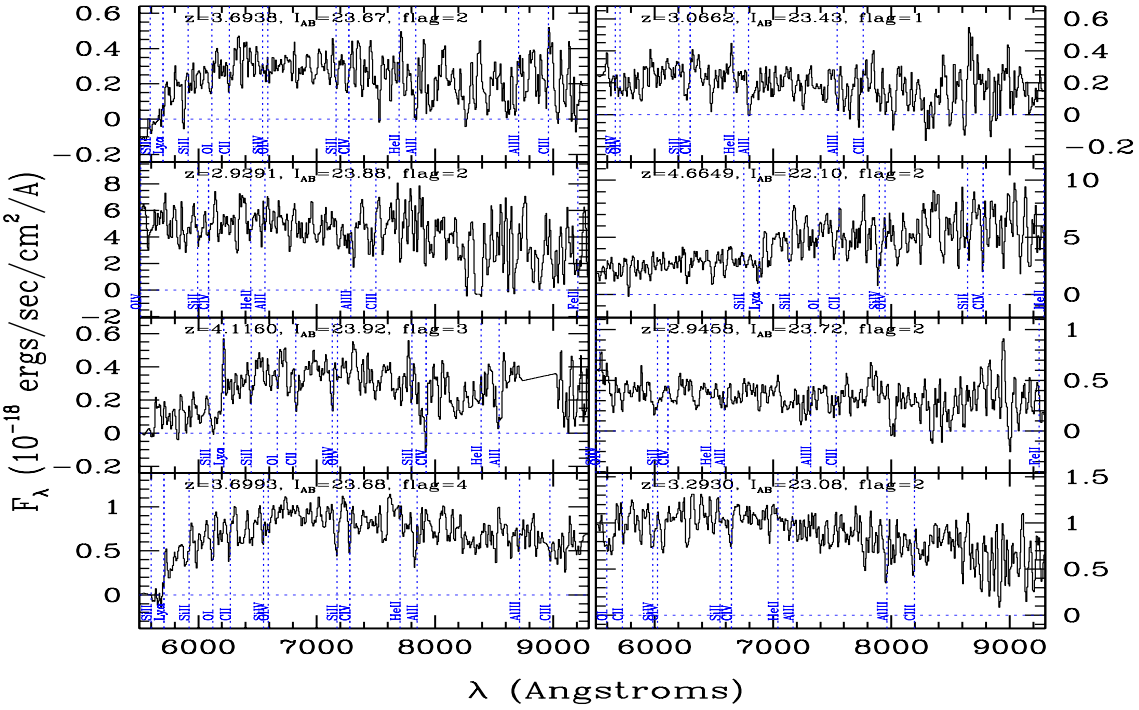

Figure 4.6. Examples of VVDS spectra in the range $2.2 < z \leq 5.0$.

4.3 Deep spectroscopic sample and main survey results

4.3.1 Redshift distribution of the $I_{AB} \leq$24 galaxy sample

The redshift distribution of the spectroscopically selected sample of galaxies with $17.5 \leq I_{AB} \leq 24$ from the VVDS is shown in Figure 4.7. The histogram peaks at $\sim$ 0.8 - 0.9 (median redshift z = 0.76; mean redshift z = 0.90) with a significant high redshift tail extending up to z $\sim$ 5. This fraction of galaxies, appearing at all redshifts $2< z <5$, indicates that the observations are deep enough to probe the brightest part of the population at these redshift. There are 558 galaxies with measured redshift $1.4 \leq z \leq 2.5$, 258 with $2.5 \leq z \leq 3.5$ and 161 with $3.5 \leq z \leq 5$; it represents the largest deep purely magnitude selected sample at this redshift so far. However, as clearly visible in Figure 4.7, there is a paucity of galaxies with measured redshift $2.2 \leq z \leq 2.6$ (the so called "redshift desert"). This is due to the VVDS observed wavelength range (5500$\AA$ - 9500$\AA$) which contains very few faint features for galaxies at these redshifts, making the redshift measurement very hard.

The redshift distribution of galaxies in the VVDS-02h field is presented in Figure 4.7 (right panel) with smaller redshift bins (dz=0.0033). The field shows an alternance of strong density peaks and almost empty regions, with strong peaks identified all across the redshift range, although less prominent at $z \gtrsim 2$. This is the first time that the large-scale structure distribution of galaxies has been probed on transverse scales $\sim 30 h^{-1}$ Mpc at

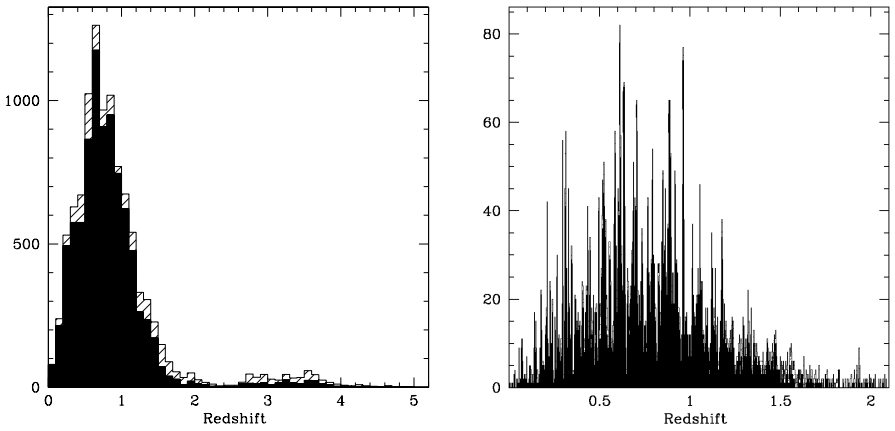

Figure 4.7. *Left:* Redshift distribution for the VVDS $I_{AB} \leq 24$ sample. It consists of 9141 galaxies with $17.5 \leq I_{AB} \leq 24$, extracted from the sum of the VVDS-CDFS and the VVDS-F02h fields. Galaxies with flags 2,3,4 and 9 are represented by the filled histogram, galaxies with flag 1 by the open histogram. This sample, including flags 2,3,4 and 9, is 93% complete. The median redshift is z = 0.62 and the mean redshift is z = 0.65. *Right:* Redshift distribution for galaxies in the VVDS-02h field with $0 \leq z \leq 1.7$, for galaxies with redshift quality flags 2,3,4,9. The redshift bin is dz=0.0033

these redshifts.

4.3.2 Galaxy evolution

One of the main goals of the VVDS is the study of galaxy formation and evolution. The galaxy luminosity function (LF) and its evolution, has been investigated from the First Epoch VVDS sample, for $17.5 \leq I_{AB} \leq 24$ by Ilbert et al. (2005). We observe a substantial evolution with redshift of the global luminosity function in all bands from U to I rest frame. Compared to the local SDSS values, we measure a brightening ranging from 1.8 - 2.4 magnitudes in the U band, to 0.1–1.4 magnitudes in the I-band, when going from z=0.05 up to z=2. The stronger brightening toward bluer rest frame wavelengths suggests that most of the evolution of the global LF up to z=2 is related to the star formation history, better probed with the luminosity measured at short rest frame wavelengths.

The First Epoch sample allows also the derivation of the LF for each of hte 4 galaxy spectral types out to $z \sim 1.5$ (Zucca et al., 2006). The results show striking differences among the different types: the early type galaxies are only mildly evolving with a 0.5 magnitudes brightening, while the late-irregular type galaxies are $\sim$2 magnitudes brigther and two times more numerous at $z \sim 1.2$–1.5. At bright magnitudes ($I_{AB} \leq 22.5$), our results are fully consistent with the *Canada-France Redshift Survey* (CFRS) results (Lilly et al., 1995). Down to $I_{AB} \leq 24$, we find some significant differences compared to previous surveys based on photometric redshift (e.g. COMBO-17, Wolf et al. 2003a), possibly due to the degeneracy in photometric redshifts computation. Finally, combining VVDS spectroscopic redshifts with public ACS/HST images from the GOODS survey, we investigate the LF evolution per morphological type on a small area of 160 $arcmin^2$

(Ilbert et al., 2006). From this analysis, we found a small increase of the density of red massive galaxies from $z \sim 1$ to $z \sim 0.2$. Since most of the massive elliptical galaxies seems already in place at $z \sim 1$, we conclude that mergers should have been very efficient a $z > 1$.

4.3.3 Evolution of the correlation function and bias

The First Epoch VVDS sample allows a direct estimate of clustering evolution over the cosmic time sampled (Le Fèvre et al., 2005a). We have computed the correlation function $\xi(r_p, \pi)$ and $w_p(r_p)$, and the correlation length $r_0(z)$, for the VVDS-02 and VVDS-CDFS fields, for a total of 7155 galaxies in a 0.61 deg^2 area. The correlation functions represent the excess probability over random distribution of finding a galaxy in a given volume and at a fixed distance from another galaxy. They are a key diagnostics of different paradigms of galaxy formation and evolution and represent the link between the dark matter distribution (obtained through models and numerical simulations) and the observed luminous matter. Unfortunately, their interpretation is complicated by the bias function *b* and by the differences in rest frame luminosities probed at different redshifts. We find that the correlation length in this sample remains roughtly constant from z=0.5 to z=1.1, with $r_0(z)$ = 2.5–2.8 h^{-1} Mpc (comoving), for galaxies comparable in luminosity to the local 2dFGRS (Colless et al., 2001) and SDSS sample (Abazajian et al., 2003), indicating that the amplitude of the correlation function was $\sim$2.5 times lower at z$\sim$1 than that observed at present time. The correlation length in our lowest redshift bin ($0.2 < z < 0.5$) is $r_0(z)$ = 2.4 h^{-1} Mpc, lower than for any other population at the same redshift, indicating the low clustering of very low luminosity galaxies (1.5 magnitudes fainter than in the 2dFGRS or SDSS). The correlation length increases to $r_0(z) \sim 3.0$ h^{-1} Mpc at higher redshift z=[1.3,2.1] (as we observe increasingly brigther galaxies) becoming comparable to the clustering length of galaxies with M_B = -20.5 in the local Universe. This is the first time that a consistent picture of galaxy clustering is obtained over such a large time whithin the same survey. The galaxy clustering seems to evolve very slowly; on the other hand predictions on the dark matter clustering show a faster evolution, therefore evidencing a strong evolution of the bias.

We investigated also the dependence of galaxy clustering on the galaxy intrinsic luminosity at high redshift (Pollo et al., 2005). At the current epoch, luminous galaxies tend to be more clustered than faint ones, in agreement with predictions from hierarchical models of galaxy formation. The difference becomes remarkable above the characteristic luminosity L^* of the Schechter luminosity function. This luminosity dependence of clustering has been so far difficult to establish because of the limited dynamic range in luminosity for even the largest local galaxy redshift surveys. Even more problematic has been to study this effect at redshifts significantly higher than zero. Moreover, the comparison of high redshift measurement to local values requires an accurate knowledge

of the evolution of the global LF.

We observe that at the median redshift z$\sim$0.9 the clustering length has a low, nearly constant value $r_0 \sim 2.9\ h^{-1}$ Mpc for luminosities $M_B < M_B^*$ rising suddenly for $M_B > M_B^*$ and approaching value $r_0 \sim 5\ h^{-1}$ Mpc similar to those of local galaxies with comparable luminosity. An other important result of this work is the clear detection of a systematic steepening of the high-redshift correlation function for absolute magnitudes brighter than M_B^*+0.5. This kind of behavior, in general not seen neither in our local sample nor in other local surveys, shows that there is a significant redshift evolution of the luminosity dependence of both the normalization and slope parameter of the galaxy correlation function.

To better investigate the trend of the bias function, the Probability Distribution Function (PDF) of galaxy fluctuations can be used. Marinoni et al. (2005), taking into account the selection function of the VVDS sample, show that the maximum of the PDF moves toward lower density regions at high redshift. Moreover the probability for a galaxy of being in an underdense region is higher at lower redshifts. These findings strongly support the theory of gravitational growth of structures and the evolution with cosmic time of the bias between matter and galaxies. Comparing theoretical expectations to observed data it is possible to study the evolution of the biasing function. Marinoni et al. (2005) inferred that the function b is non linear and rises in underdense regions, implying a mass density threshold for galaxy formation, with the threshold being a function of redshift. In a linear approximation of the biasing function, the bias is an increasing function of redshift and its evolution is stronger at $z > 0.8$. Moreover, dividing the galaxy sample in red and blue populations, Marinoni et al. (2005) find that red galaxies are more biased tracers of the total mass.

4.3.4 The large scale structure

The complete spectroscopic survey gives access to a sampling of the high redshift Universe at z $\sim$ 1 equivalent to the sampling of the 2dFGRS at a mean redshift z $\sim$ 0.1, with a mean inter-galaxy separation of ~ 5 Mpc (comparable to the 2dFGRS). This allows the identification of galaxy structures in the VVDS fields. Using the VVDS in combination with other spectroscopic, photometric and X-ray surveys from the literature, several galaxy structures have been detected in this field (Adami et al., 2005).

For this analysis, both a friend-of-friend-based algorithm applied to the spectroscopic redshift catalog and an adaptive kernel galaxy density and color maps correlated with photometric redshift estimates were used: 17 compact structures and 1 more diffuse wall were detected. The most important are a chain-like structure at $z = 0.66$ and a dense wall at $z = 0.735$. The chain-like structure is embedded in a quite diffuse wall showing signs of ongoing collapse and perhaps similar to the progenitors of giant nearby elliptical galaxies. The dense wall at $z = 0.735$ is instead very compact in redshift space and extends across

the whole field of view. The number of massive structures we detected is consistent with what is expected for a ΛCDM model but a larger sample, on which we are currently working, is required to put significant cosmological constraints.

4.3.5 The high redshift Universe

One of the most important goal of the modern astrophysics is the understanding of the evolution of galaxies. To do that we need to know as accurately as possible how many galaxies were present in the Universe at different epochs. One technique to identify galaxies in the distant Universe is to use the discontinuity in the spectrum produced by the photon absorption below the 912*Å* Lyman limit to isolate high redshift galaxies from the dominating population of foreground galaxies in color-color diagrams (Steidel et al., 1999). This technique has led to the identification of the Lyman-break galaxies (LBGs) at redshift z=2-4. However, this color-selection technique with its associated uncertainties and assumptions could exclude a significant fraction of the high-redshift galaxy population because their colors are the result of a complex mix of stars, gas, dust or active galactic nuclei. The VVDS allowed to identify spectroscopically, 970 galaxies with redshift $1.4< z <5$, selected from a purely I-band flux selected sample (Le Fèvre et al., 2005b). Figure 4.8 show clearly that our sample lies in both color-color regions and not only in the standard permitted area.

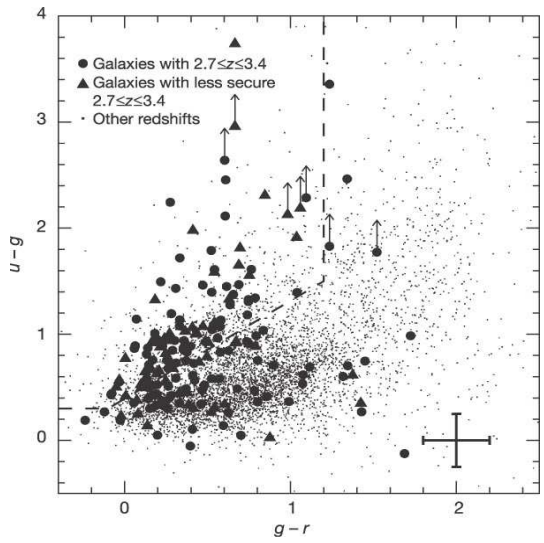

Figure 4.8. Color diagram of the VVDS high-redshift galaxies. Circle and triangle symbols represent galaxies at high redshift while small dots are galaxies at other redshifts. The dashed line delineates the area where Lyman Break Gakaxies with $2.7< z <3.4$ would be searched for if a color-color pre-selection was performed (Steidel et al., 1999).

The estimated number density measured from this sample at z=3 is between 1.6 and 6.2 times larger than those obtained from the color-selected Lyman-break samples. This result therefore shows that the Universe contained more galaxies at redshift 1.4 to 5 than previously reported using the color-selection technique. This indicates that the bright end

of the galaxy luminosity function at these early epochs is more populated than previously thought. Moreover, this result demonstrates that magnitude-selected samples, although requiring a large number of redshift measurements, provide a more complete census of the high-redshift galaxy population. Our discovery of a significantly population at high redshift than was previously believed has important consequences for our understanding of galaxy evolution.

Chapter 5

The VVDS type–1 AGN Sample

From the VVDS survey, as an integrated part of classification and redshift determination of the reduced VVDS spectra, we collected a sample of type–1 AGN. Here I will present the selection method and the properties derived from it.

5.1 The AGN selection

The AGN catalog considered in this thesis consists of a sub-sample of objects in the VVDS spectroscopic catalog, identified purely on the basis of the presence of at least one broad emission line in their spectra. Given our effective spectral resolution, a line is here considered broad if its FWHM is larger than 1000 km s^{-1}. Our sample consists therefore of *Broad Line AGN* (BLAGN) since only type–1 AGN with an *observed* broad line have been selected.
However, through this manuscript we will refer to these objects with both type–1 AGN and BLAGN names. Moreover, no distinction between Seyfert galaxies and QSOs based on the absolute magnitude or morphology of the objects has been introduced. Narrow line AGN (type–2) are not included in the present catalog because, when only narrow emission lines are present, it is not easy to distinguish AGN activity from starburst activity, especially in spectra with relatively low S/N ratio and limited wavelength range. This population has been selected on the basis of the line ratios, as explained in Section 3.1.2 and will not be included in this thesis.

5.1.1 Identification and redshift quality flags

At each object we have assigned a value for the spectroscopic redshift and a spectroscopic quality flag which quantifies our confidence level in that given redshift based on a method similar to that used for galaxies and already explained in Section 4.2.4. It follows these criteria:

Flag 14: BLAGN with secure redshift measurement (i.e.: two lines or more);

Flag 13: BLAGN with only one broad line detection but with the redshift secured from other informations such as:

- there is no other possible identification for the given wavelength range;
- an intervening absorption lines system is detected and leave only one redshift solution for the BLAGN;
- strong iron features, so called 'bumps', are detected;
- a second line is marginally detected.

Flag 19: BLAGN with only one detected line and more than one possible redshift;

Flag 12: Object with secure redshift but for which the broad line nature is uncertain due to the low spectral resolution, often coupled with low S/N or to technical limitations (i.e. it could be a narrow line object);

Flag 11: Both the redshift and the broad line nature of the target are uncertain.

Objects with uncertain broad emission lines (flags 11 and 12), corresponding to $\sim$ 10 - 15 % of our survey objects, are excluded from the present analysis since we do not want to be contaminated by normal galaxies and we don't know which percentage of these objects are really broad-line AGN.

5.2 The BLAGN catalog

The final sample of BLAGN spectra selected from the VVDS survey consists of 130 BLAGN with flag=14,13 and 19, in the redshift range $0 < z < 5$, selected in 3 VIMOS fields (0226-04, 1003+01 and 2217-00) and in the Chandra Deep Field South (CDFS), which was partly included in the VVDS observations. We discovered 74 of them in the deep fields (62 in the 02h field and 12 in the CDFS) and 56 in the wide fields (18 in the 10h field and 38 in the 22h field). The distribution of BLAGN across the VVDS fields is shown with red dots in figure 5.1. The total amount of BLAGN, which consists of 130 objects, corresponds to about 0.7% of the objects in the total VVDS database with a measured redshift. This sample represents an unprecedented complete sample of faint AGN, free of morphological or color selection bias.

5.2.1 Redshift degeneracy

The exact list of emission lines we expect to detect in any given spectrum is a function of its S/N. In addition, because of the limited wavelength coverage of the observations, there are some redshift intervals where only a single broad emission line may be detected in our spectra (see gray portions in figure 5.2). In these cases, if no other features (e.g. narrow emission lines, absorption systems, Lyman forest) are present, several interpretations of

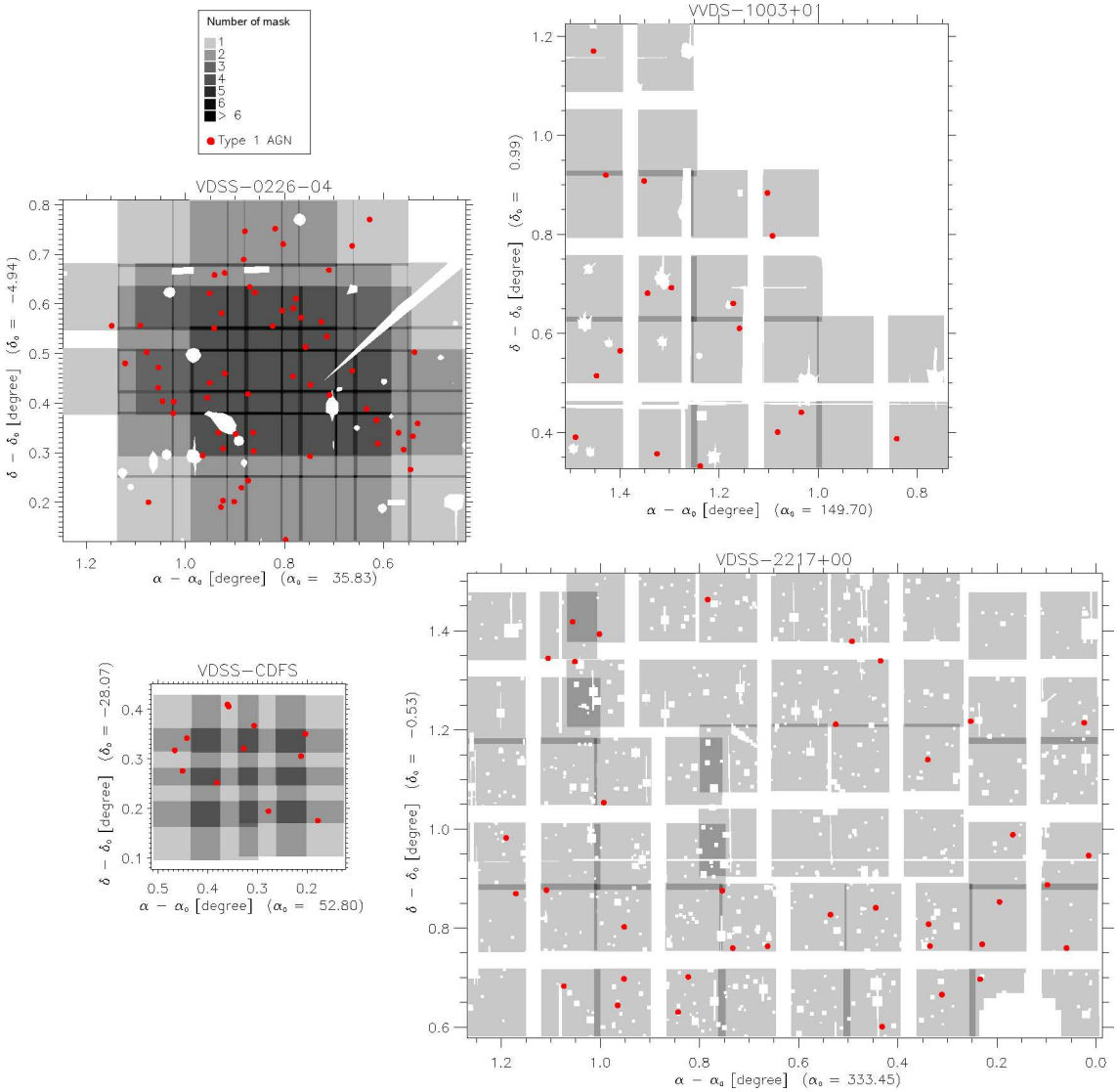

Figure 5.1. Spectroscopically observed area $\mathcal{A}$ in the VVDS first epoch fields: the grey scale indicates the number of VIMOS passes. The area masked in the photometric catalog has been subtracted from the different VIMOS fields of view. Red dots indicates type 1 AGN identified in the spectroscopic catalog.

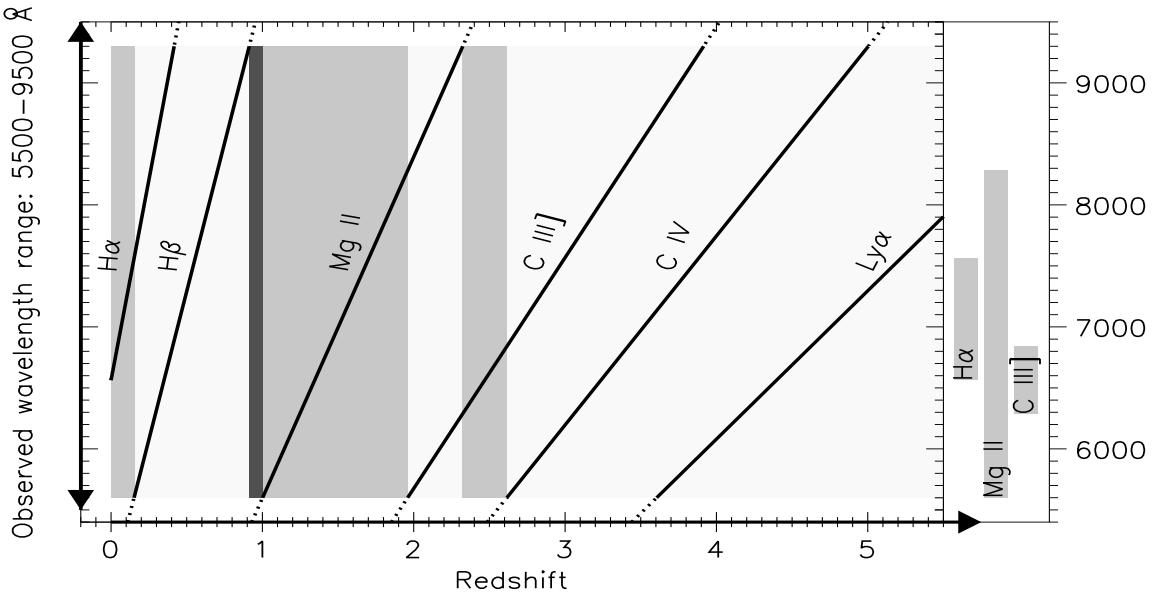

Figure 5.2. Visibility in the wavelength range of our data of AGN broad emission lines along redshift: The thick lines trace the observed wavelength as a function of redshift of the main AGN broad emission lines that we expect to detect in our spectra. The objects in which we detect only a single broad emission line are expected to be in the redshift ranges shown in light gray. We expect to miss BLAGN lying in the narrow redshift range filled in dark gray since no strong broad emission line is visible at that redshift within our observed wavelength window. On the right side are reported the wavelength ranges in which each broad emission line can be observed as a single line. Hβ and Lyα are not reported there since they are not affected by the redshift degeneracy.

the broad line may be allowed, thereby leading to a degeneracy of solutions for the redshift (see an example in Figure 5.4; object 220098629).

In order to treat redshift degeneracy in a consistent way, we have taken the SDSS composite spectrum of BLAGN (Vanden Berk et al., 2001), convolved it to our resolution, and added noise. For each line we then determined the S/N which would provide a 3.5 σ detection of the line. Following this procedure we have found that for a S/N lower than 4 per resolution element, we are able to detect and recognize as broad the following lines: H$\alpha\lambda$6563*Å*, H$\beta\lambda$4861*Å*, Mg IIλ2799*Å*, C III]λ1909*Å*, C IVλ1549*Å* and Ly$\alpha\lambda$1216*Å*.

The visibility windows of these lines within the VVDS observed spectral range are shown in figure 5.2 as a function of redshift. The redshift ranges where we expect to observe a single broad emission line (in gray) are: [0 - 0.13], [1.0 - 1.9] and [2.4 - 2.6]. Since we always expect to detect the narrow-emission-line doublet [O III]$\lambda\lambda$4959, 5007*Å* close to Hβ we consider the detection of Hβ to securely identify the redshift. Consequently, for an object with a single broad line, we have up to three possible redshifts. In addition, a small gap is present at redshift $\sim$0.95 (dark gray in Figure 5.2) where no broad emission line is visible within our observed wavelength window.

A small fraction of spectra ($\sim$ 15%) fall outside this general scheme, due to a lower S/N or to technical limitations such as strong fringing. For this reason some objects have up to four possible redshifts (see Table 5.3).

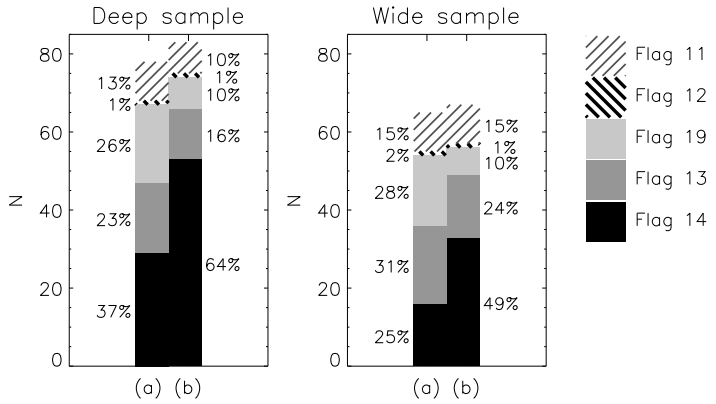

Figure 5.3. AGN quality flags statistics. Columns (a) correspond to our original quality flags, before looking for objects already existing in other spectroscopic samples and performing re-observations with FORS. Columns (b) correspond to our current quality flag statistics.

Because of these limitations, a total of 42 BLAGN in our original sample were flagged as having a degenerate redshift (flag 19, as defined in Section 5.1.1). For all of them, however, a *best solution* is proposed. To solve this redshift degeneracy we have first looked for the objects already observed in other spectroscopic surveys in the same areas. From the CDFS optical spectroscopic data we found the redshifts of 3 of them (Szokoly et al., 2004).
Furthermore, additional observations have been obtained with FORS1 on the VLT in March 2004 and November 2005 to extend the spectral coverage down to 3800*Å*. With these additional observations we solved $\sim$57% of our 42 degeneracy, finding a secure redshift for 24 of our AGN with ambiguous redshift determination. Moreover, we found that our proposed best solution was the correct one in $\sim$ 77% of the cases.

As of today, we have 115 BLAGN with secure redshift, and 15 BLAGN with two or more possible values for the redshift.

The statistics of the data quality according to these flags, before and after the FORS1 follow-up, is summarized in Figure 5.3. As we already said, flag 11 and 12 are excluded from our sample.

The final list of BLAGN is presented in the Tables at the end of the Chapter: Table 5.2 gives the list of BLAGN in our wide and deep samples for which we have a secure redshift, while Table 5.3 lists the BLAGN for which we still have a redshift degeneracy (flag 19) with all the possible z solutions. Best z solution are reported in boldface.

Figure 5.4 presents some examples of spectra across our magnitude and redshift range. In particular, object 220567224 is the highest redshift BLAGN discovered with this survey; object 020180665 is an example of a broad-absorption-line (BAL) spectrum, while object 020302785 is instead a BLAGN at z=2.24 in which there are evident intervening absorption features at z=1.727. Object 020463196 is an example of AGN in which strong [NeIII], NeIV and [NeV] lines are visible and finally, object 220098629 is an

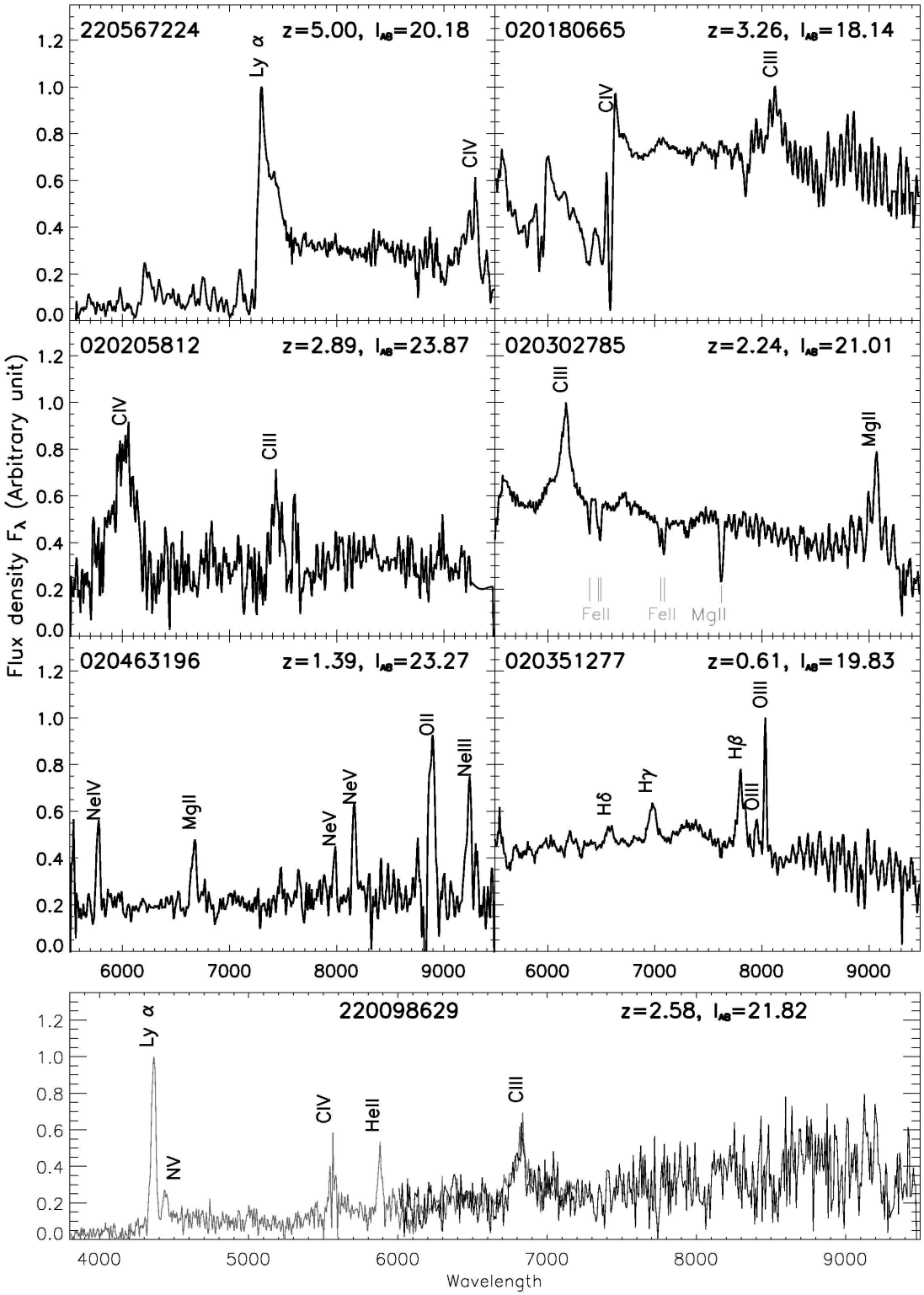

Figure 5.4. Examples of BLAGN spectra across our magnitude and redshift ranges.

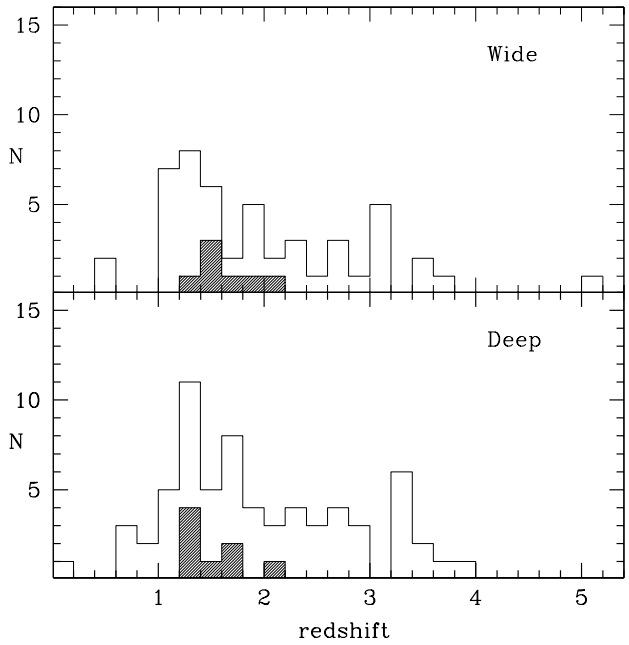

Figure 5.5. Redshift distributions of the wide (upper panel) and the deep (bottom panel) VVDS BLAGN sample. The unshaded histogram corresponds to BLAGN with secure redshift (flags 13 and 14), while the shaded histogram includes flag 19 BLAGN with their best solution.

example of flag 19 for which the redshift was resolved using the spectroscopic follow-up with FORS1@VLT-UT3.

5.3 Redshift distribution

The redshift distributions of our wide and deep samples are presented in Figure 5.5. BLAGN with degenerate redshift solutions (flag 19) are presented, in the shadow histogram, with their best solutions. The absence of objects between redshift 0.5 and 1 in the wide fields can be attributed to our low efficiency for selecting objects in this redshift range (see Figure 6.2).

The fraction of $z > 3$ objects is $\sim$ 18% in the wide sample and $\sim$ 14% in the deep sample. The mean redshift is ~ 1.9 in both the wide and deep samples. This shows that, by pushing our limit in magnitude from the wide to the deep survey, we are not increasing our mean redshift but rather exploring the fainter part of the luminosity function at all redshifts.

Figure 5.6 shows the apparent magnitude versus redshift distribution of BLAGN and galaxies in the deep sample. We see that the VVDS objects samples the faint magnitudes, well inside the galaxy luminosity function. We find that $\sim$ 35% of the objects in the deep sample are Seyfert galaxies, rather than QSOs, having absolute magnitudes fainter than $M_B = -23$.

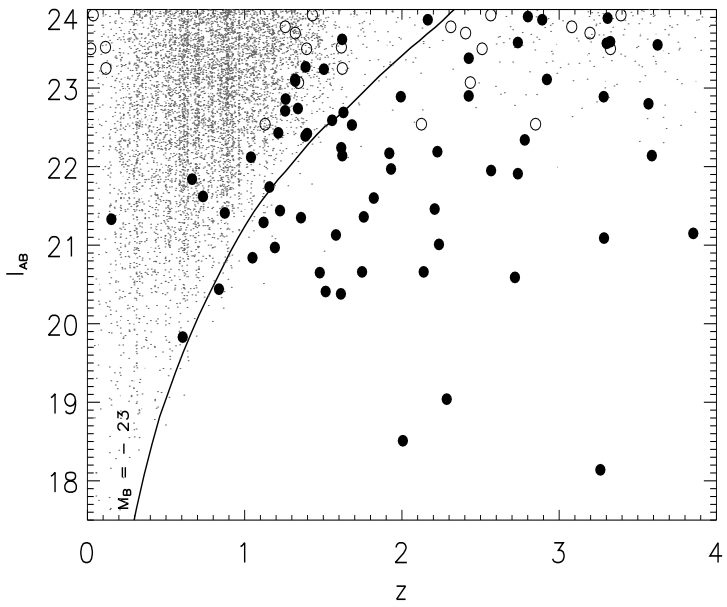

Figure 5.6. Apparent I_{AB} magnitude as a function of redshift in the VVDS deep sample. Galaxies are plotted with small points, BLAGN with secure redshift are plotted with filled dots and BLAGN with degenerate redshift are presented at all their redshift solutions with empty circles. The thick line gives the apparent magnitude of a BLAGN template of absolute magnitude $M_B = -23$ and therefore corresponds to the transition between the QSOs and Seyfert galaxies.

5.4 A-posteriori morphological analysis and color-color diagrams

As already discussed in Section 3.1.1, the classical way to create an optical BLAGN sample is to preselect candidates from a photometric catalog requiring that the objects are point-like and have blue colors. However, this selection criterium introduces a bias mainly due to two effects:

(a) It excludes objects at low redshift, for which the contribution of the host galaxy is detected and resolved, thus introducing a bias especially toward the faint end of the BLAGN luminosity function;

(b) It is not able to select QSOs with redshift larger than 2.3 as the Lyα line is shifted out the UV passband.

The fundamental property of our survey is that the target selection is performed only on the basis of the I-band magnitude and indeed our BLAGN sample does not suffer neither from morphological nor from color selection biases which are present in most optical surveys. Therefore, using the VVDS deep photometric data, we are able, a posteriori, to quantitatively estimate the fraction of AGN missed by these standard selection criteria.

5.4.1 Morphological analysis

The use of a morphological selection of point-like objects causes the loss of BLAGN candidates for two main reasons. The first is due to the fact that a reliable separation between point-like and extended sources from ground-based data images is possible only for relatively bright objects. The second is linked to an intrinsic property of BLAGN: at relatively low z and low intrinsic luminosity, BLAGN may appear extended or at least slightly resolved because of significant contribution from the host galaxy. This effect can introduce a redshift-dependent bias in morphologically selected AGN samples, especially at faint magnitudes.

We have conducted a morphological analysis of our BLAGN sample through the study of various shape parameters, which define a characteristic radius weighted by the light distribution function (Kron, 1980). In particular, for this analysis we used the `SExtractor` flux-radius parameter, denoted as r_2, which measures approximately the radius which encloses half of the object's total light.

This parameter is used to identify point-like sources, because, for unresolved objects, it is directly related to the width of the point spread function and it is independent of luminosity (for non-saturated objects). In the plane r_2 (measured in I-band) versus I-magnitude, we can distinguish two different classes of objects: unresolved sources that occupy a well defined strip of the plane at small and approximately constant values of r_2 and resolved objects for which r_2 varies with magnitude.

This analysis is restricted to the F02, F10 and F22 fields. We exclude the CDFS for which this parameter is not measured. Since our data, covering large areas in different sky regions, have been taken with different seeing conditions, the stellar locus resulting from the use of the measured r_2 values is significantly broadened, thus making difficult a clear separation between point-like and extended objects. To account for this, we used an "adaptive" classification technique following McCracken et al. (2003). After dividing the field into many sub-areas, mainly following the pattern corresponding to different pointings, we have normalized the flux radius of each object to the local r_2 mode, computed for all the objects within each sub-area. Figure 5.7 shows this normalized r_2(I) parameter versus I-magnitude.

The use of the normalized r_2(I) allows us to improve our ability to distinguish point-like from extended objects. As shown in Figure 5.7, this separation appears to be feasible up to $I_{AB} \sim 22.5$ (without normalization, the corresponding limiting magnitude was $I_{AB} \sim 21.5$). Beyond this magnitude ($I_{AB} \sim 22.5$), the number of galaxies with small $r_2(I)$ parameter increases and no reliable selection of point-like sources is possible.

The two horizontal lines correspond to the range in $r_2(I)$ we have adopted for our morphological classification of point-like sources. The upper limit in this range corresponds to about 3.5σ of the Gaussian fit of the r_2 normalized distribution of point-like sources. As shown by the inset in the left part of Figure 5.7, this somewhat

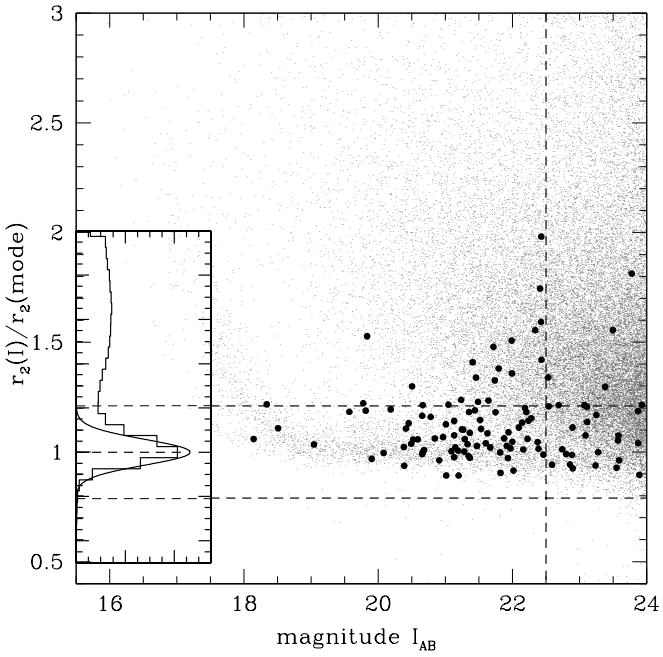

Figure 5.7. Normalized $r_2(I)$ parameter versus I_{AB} magnitude. The two horizontal lines correspond to the range in $r_2(I)$ we have adopted for our morphological classification of point-like sources. Large circles are the spectroscopically confirmed BLAGN. The inset shows the r_2 distribution of objects with $21.0 < I_{AB} < 22.0$, fitted with a Gaussian with $\sigma = 0.06$.

conservative choice makes sure that the vast majority of point-like sources are really classified as point-like, allowing some contamination from extended objects, especially at faint magnitude. Efficiency in classifying point-like sources has been tested on the spectroscopically confirmed stars in the magnitude range $18.5 \leq I_{AB} \leq 22.5$ (the bright limit has been set in order to exclude saturated objects (see Figure 5.7)). We find that 95% of the stars with spectroscopic flag ≥ 3 are correctly classified as point-like sources.

Figure 5.7 also shows the location in this plane of the spectroscopically confirmed BLAGN. In this analysis we consider only BLAGN brighter than $I_{AB} = 22.5$ (90 objects); within this limit, 77% of the BLAGN are classified as point-like, while 21 of them (23%) are classified as extended. This percentage is significantly higher than that of morphologically misclassified stars (see above).

Nineteen of these 21 extended BLAGN, have a secure redshift measurement, while the other 2 are BLAGN with two or more possible values for z. Figure 5.8 shows the redshift distribution of BLAGN with secure redshift and $I_{AB} \leq 22.5$, morphologically classified as extended compared to those classified as point-like. The two redshift distributions are significantly different (the probability that they are drawn from the same distribution, as estimated from a Kolmogorov-Smirnov (KS) test, is smaller than $\sim 4 \times 10^{-4}$), with the extended BLAGN having on average a lower redshift. The figure shows that sixteen out of nineteen of these BLAGN have $z < 1.6$ and in this redshift range they constitute $\sim 42\%$

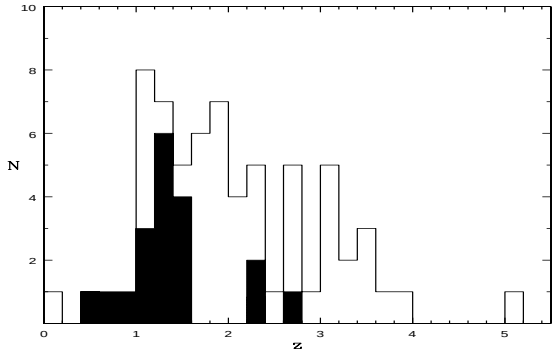

Figure 5.8. Redshift distribution of BLAGN with secure redshift and $I_{AB} < 22.5$. The unshaded histogram shows the objects classified as point-like, while the filled histogram shows the objects classified as extended.

of the sample.

5.4.2 Color-Color diagrams analysis

The use of the UVX color preselection causes the loss of some BLAGN candidates because colors are affected by emission lines as they are redshifted into and out of the filter passbands. This effect leads to a redshift dependence of the completeness. Moreover BLAGN without a UVX excess are excluded by this method.

We investigate here what would have been the results of a simple ultraviolet excess preselection technique based on three color bands applied to our sample. For this purpose we used the deep photometry obtained in the frame of the CFHTLS and we plotted our point-like objects in the color plane $u^* - g'$,$g' - r'$, as shown in the left panel of figure 5.9. We could then set a color selection criterium meant to exclude most of the main sequence stars: (a) $u^* - g' < 0.62$; (b) $g' - r' < 0.16$. The exclusion area is reported in gray in figure 5.9. Most of the objects in the exclusion area, outside the locus delineated by the main sequence stars are compact galaxies classified as point-like objects.

Following the evolutionary track of a QSO template (here the SDSS composite spectrum, Vanden Berk et al. 2001) in this color plane (middle panel of figure 5.9), we expect that this selection criterium is efficient up to $z \sim 2.3 - 2.5$.

We estimate now which fraction of the optical AGN population with $z < 2.3$ would have been missed by this selection criterium. Our AGN sample with $z < 2.3$ and photometric information in the u^*,g' and r' band is reported in this plane (right panel of figure 5.9). We find that $\sim$ 25% of the population of our optical BLAGN would have been excluded by this color selection. If we restrict now our analysis to a limiting magnitude of $I_{AB} < 22.5$, we find that $\sim$ 35% of our AGN do not fulfill this color selection criterium combined with a morphological selection of point like objects. As expected, at higher redshift this selection criterium becomes inefficient, with 75% of our $z > 2.3$ objects excluded.

We would like to emphasize that these completeness rates are found for our sample

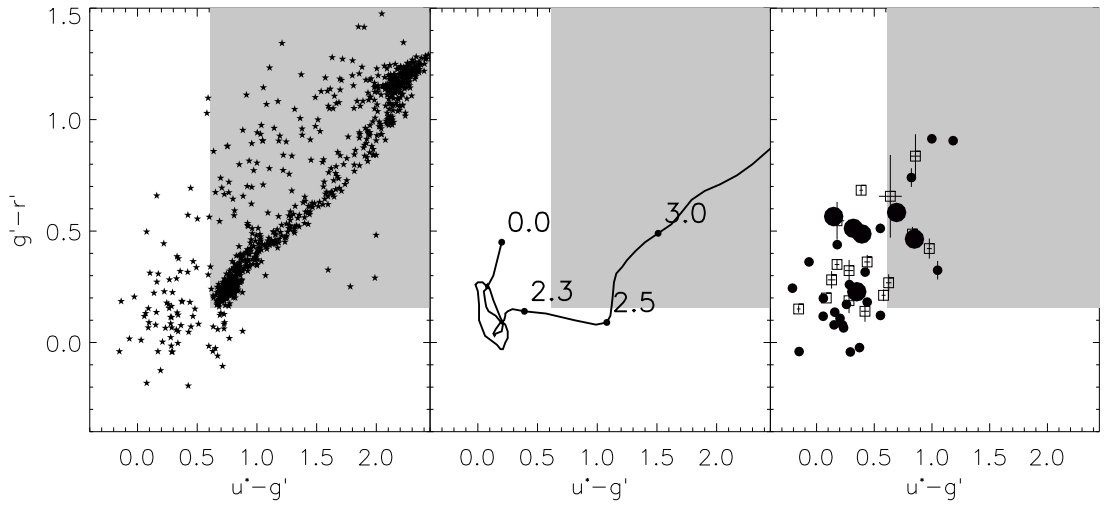

Figure 5.9. $u^* - g'$, $g' - r'$ color diagram. Left panel: location of the point-like objects in our photometric catalog. An exclusion area, reported in gray, is set to exclude most of main sequence stars. Middle panel: color evolutionary track with redshift of a BLAGN. The template considered here is the SDSS composite spectrum. Right panel: location of AGN with $z < 2.3$. AGN which could not be morphologically classified ($I_{AB} > 22.5$) are plotted with open boxes. AGN classified as extended are large circles, while AGN classified as point-like are small circles.

which is two to three magnitude deeper than current major samples and do not necessary apply to existing brighter samples. At faintest magnitude in fact, both morphological and UVX selection efficiency decreases: (a) at relatively low z and low intrinsic luminosity, BLAGN may appear extended and (b) faintest objects are found to have on average redder colors than the brightest ones (see Section 5.6). From this morphological and color analysis we conclude that classical optical preselection techniques are significantly under-sampling the overall BLAGN population in deep samples.

5.5 Composite Spectrum

A useful instrument to study the mean spectral properties of a class of objects is the composite spectrum. It allows to enlarge the wavelength range covered by single spectra[1] and indeed to study the mean spectral properties. Moreover, it provides a reference to study the deviation between these mean properties and those of the individual objects or to highlight the differences between different samples characterized by different selection functions.

Despite differences in detail between individual objects, QSOs spectra, with respect to stars and galaxies, bear a strong family resemblance, including features such as a non-thermal power-law continuum, a UV excess and broad emission lines.

A rest-frame composite spectrum was generated according to the method described in

[1] observed spectra cover a restricted wavelength range which corresponds to different intrinsic wavelength ranges depending on the redshift of the objects

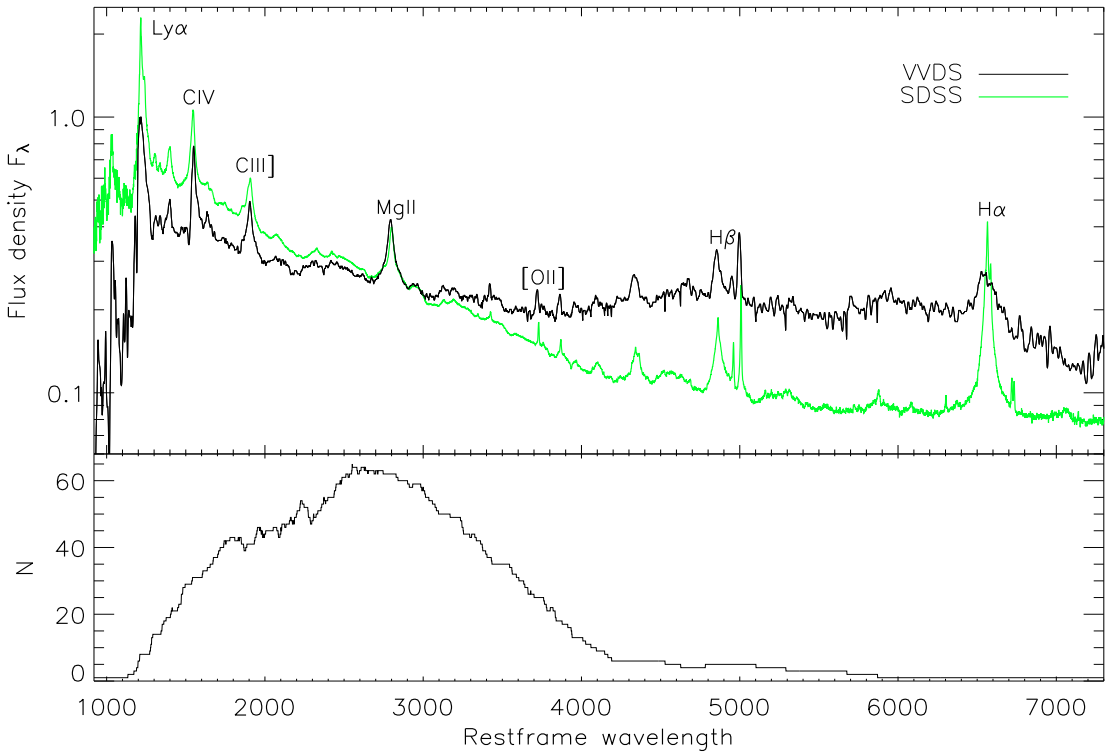

Figure 5.10. Composite spectrum. Top panel: Composite spectrum of the VVDS BLAGN with secure redshift (black) compared with the SDSS composite spectrum (green). Bottom panel: Number of contributing spectra as a function of wavelength.

Francis et al. (1991). The spectra were first blue-shifted in their rest frame and rebinned to 1 Å. The lowest redshift spectrum was taken as a starting point to build the long wavelength part of the composite. The spectra were then taken in order of increasing redshift and for each of them the spectral range in common with the composite was determined. A scaling factor was then applied to each subsequent spectrum to ensure that it had a median continuum flux equal to that of the partially complete composite over the wavelength range in common. Finally it is added to the composite. Each contribution is weighted by the corresponding individual average S/N ratio. The co-addition has been done using a geometric mean in order to preserve the underlying continuum logarithmic slope of the quasar sample as a whole. The arithmetic mean of a sample of power law spectra ($f_\nu = \nu^{-\alpha_\nu}$ or, expressed in wavelength, $f_\lambda = \lambda^{-(\alpha_\nu+2)}$) is not in fact, in general, a power law with the mean index. On the contrary, considering the geometric mean, which is defined as:

$$\langle f_\lambda \rangle_{gm} = \left(\prod_{i=1}^{n} f_{\lambda,i} \right)^{1/n}$$

(where $f_{\lambda,i}$ is the flux density of spectrum number i in the bin centered on wavelength λ, and n is the number of spectra contributing to the bin) we obtain: $\langle f_\lambda \rangle_{gm} \propto \lambda^{-(\langle\alpha_\nu\rangle+2)}$, where $\langle\alpha_\nu\rangle$ is the (arithmetic) mean value of the frequency index α_ν. Once all spectra

are co-added, a sliding gaussian filter ($\sigma = 2$ Å) is applied to the composite to improve the S/N ratio. The generation of a composite spectrum requires an accurate estimate of the redshift of each quasar. Individual redshifts are thus slightly varied so as to maximize the peaks of each main emission line, then they are averaged and corrected to fix the line peaks close to their laboratory wavelengths. Then the entire procedure is iterated, the convergence being quite fast after 2 or 3 iterations. All 115 BLAGN spectra with secure redshifts but one have been used to generate the composite. In particular, BAL spectra are included. The spectrum of the object 000029274, at redshift 0.7352, is strongly affected by the residual noise of the fringing pattern and contributes to a wavelength range covered by only 5 other objects. For this reason it was excluded in generating the composite. The final resulting composite is shown in Figure 5.10 along with the number of contributing spectra at each wavelength. For comparison the SDSS composite spectrum obtained with the same method over 2200 spectra is plotted over our composite (Vanden Berk et al., 2001).

The maximum number of individual spectra contributing to the composite is 64 near 2570 Å. At both wavelength ends, just few objects contribute to the composite spectrum. The signal to noise is ~ 60 in the $2000 - 4000$ Å range and decrease at both shorter and longer wavengths. We measured the EW of the main emission lines in the composite using the IRAF package [2]. Broad emission lines have been fitted by a Lorentzian profile, while narrow emission lines have been fitted by a Gaussian profile. C IV and Lyα lines have been deblended from their absorption component. The resulting EW values are given Table 5.1 and are compared to those of the SDSS composite spectrum.

Significant differences are seen in the EW of Lyα and Hα. The reason for such discrepancies is likely to be essentially due to the large variety of EWs for the same line observed in QSO spectra, since very few objects are contributing at both ends of the VVDS composite spectrum, 5 or less below 1200 Å and above 5050 Å.
We interpret the larger EW we obtain for the C IV, C III] and Mg II lines as a consequence of the Baldwin effect [3] (Baldwin, 1977), our objects being a factor up to 100 times fainter than the ones of the SDSS sample.

The overall continuum shape of our composite spectrum is redder than the SDSS one composite and this is particularly true at $\lambda > 3000$ Å. We will discuss this aspect in Section 5.6.

5.6 Colors of our sample

The comparison of the VVDS and SDSS composite QSO spectra shows that the VVDS continuum is significantly redder than the SDSS one, especially at long wavelengths.

[2] http://iraf.noao.edu/

[3] Anti-correlation of high ionization line strength with continuum luminosity.

Line	λ_0	EW (VVDS)	EW (SDSS)
Lyα+N V	1216+1240	137.4	92.91
Si IV+O IV]	1396+1402	7.9	8.13
C IV	1549	46.0	23.78
C III]	1909	25.5	21.19
Mg II	2798	40.3	32.28
[O II]	3727	3.4	1.56
[Ne III]	3869	2.7	1.38
Hδ	4103	5.0	5.05
Hγ	4342	21.8	12.62
Hβ	4861	33.8	46.21
[O III]	4959	4.9	3.50
[O III]	5007	16.8	13.23
Hα	6562	137.5	194.52

Table 5.1. Rest-frame EWs and FWHM of the emission lines in the VVDS composite spectrum and their comparison to the corresponding lines of the SDSS composite spectrum.

Figure 5.11 presents the differences as a function of redshift between the $B_{AB} - I_{AB}$ colors of our BLAGN sample and the color expected for the SDSS composite spectrum for $z < 2.8$. The dispersion in color is large and most of our objects have a significantly redder color than that expected from the SDSS composite spectrum. Moreover, the faintest objects (Seyfert galaxies, $M_B > -23$, grey points) appear to have on average redder colors than the brightest ones (QSQs, $M_B < -23$, black points). A KS test applied on the Seyfert galaxies and QSOs colors indicates a probability $\sim 1 \times 10^{-3}$ that these objects have the same color distribution.

Moreover, we observe that for $\sim 50-60$ % of our reddest AGN (objects with $(B_{AB} - I_{AB}) - (B_{AB} - I_{AB})_{SDSS} > 0.8$) we detect the extended component of the BLAGN host galaxy in I band. This could be an indication of the fact that colors are reddened by the host galaxy flux contribution.

Restricting our analysis only to the 02h deep sample, in which we can take advantage of the whole VVDS photometric coverage (U, B, V, R, I, J, K), we derived the spectral index α by fitting a simple power law $f(\nu) = \nu^{-\alpha}$ to our photometric data points. In figure 5.12(a),we plot the spectral index α as a function of the AGN luminosity. The choice of the reference wavelength for the absolute magnitude, $\lambda = 1450$ Å, is motivated by our photometric coverage. In fact, for most of the objects it is possible to interpolate M_{1450} directly from the observed magnitudes.

Most of the AGN with $\alpha > 1$ are fainter than $M_{1450} = -22.15$, showing that the faintest objects have on average redder colors than the brightest ones. The outlier (the brightest object with large α, i.e. very red colors, in the upper right corner of the plot) is a BAL AGN.

Figure 5.12(b) shows the histograms of the resulting power law slopes for the same AGN

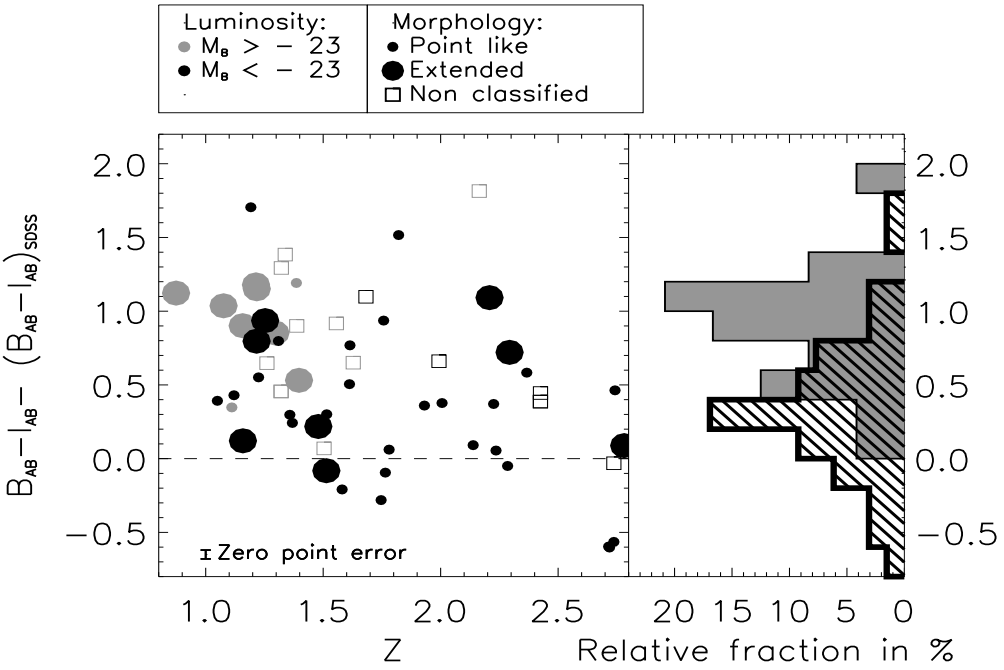

Figure 5.11. Differences as a function of redshift between the observed $B_{AB} - I_{AB}$ colors and the color expected for the SDSS composite spectrum. Black circles correspond to QSOs, while the gray circles correspond to Seyfert galaxies. The $B_{AB} - I_{AB}$ color histograms of these two populations are shown on the right. Moreover small and large circles correspond respectively to objects morphologically classified as poin-like and extended. Open squares are instead morphologically not classified (I_{AB} >22.5).

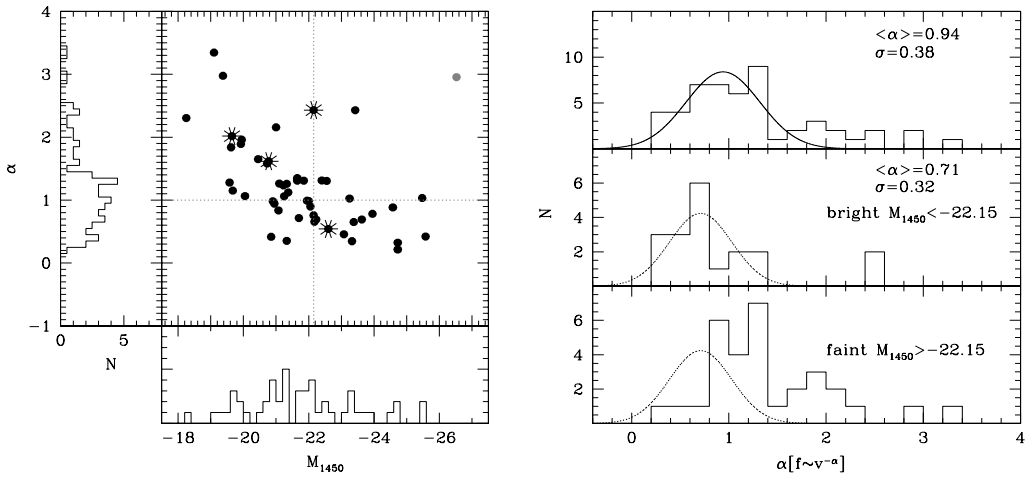

(a) (b)

Figure 5.12. (a) Distribution of the spectral index α as a function of M_{1450}. The spectral index is derived here by fitting a simple power law $f(\nu) = \nu^{-\alpha}$ to our photometric data points. Asterisks are AGN morphologically classified as extended. (b) Distribution of the spectral index α for the same sample of AGN as in (a). All the AGN in this sample are shown in the upper panel, while the AGN in the "bright" and "faint" sub–samples are shown in the middle and lower panel, respectively. The dotted curve in the middle panel corresponds to the gaussian fit of the bright sub–sample and it is reported also in the lower panel to highlight the differences in the α distributions of the two sub-samples.

sample. The total sample is plotted in the upper panel, while the bright and the faint sub-samples are plotted in the middle and bottom panels, respectively. A Gaussian curve with $\langle\alpha\rangle = 0.94$ and dispersion $\sigma = 0.38$ is a good representation for the distribution of about 80% of the objects in the upper panel. In addition, there is a significant tail ($\sim$ 20%) of redder AGN with slopes in the range from 1.8 up to $\sim$ 3.0. The average slope of the total sample ($\sim$ 0.94) is redder than the fit to the SDSS composite ($\sim$ 0.44). Moreover, the distribution of α is shifted toward much larger values (redder continua) than the similar distribution in the SDSS sample (Richards et al., 2003). For example, only 6% of the objects in the SDSS sample have $\alpha > 1.0$, while this percentage is 57% in our sample.

The differences with respect to the SDSS sample can be partly due to the differences in absolute magnitude of the two samples ($i^* < 19.9$ for the SDSS sample and $I_{AB} < 24.0$ for the VVDS sample). In fact, if we consider the VVDS "bright" sub-sample, the average spectral index $\langle\alpha\rangle$ becomes $\sim$ 0.71, which is closer to the SDSS value (even if it is still somewhat redder), and only two objects ($\sim$8% of the sample) show values not consistent with a gaussian distribution with $\sigma \sim 0.32$. Moreover, only 30% of this sample have $\alpha > 1.0$.

Most of the bright SDSS AGN with $\alpha > 1$ are interpreted by Richards et al. (2003) to be dust-reddened, although a fraction of them is likely to be due to intrinsically red AGN (Hall et al., 2006). At fainter magnitude one would expect both a larger fraction of dust-reddened objects (in analogy with indications from the X-ray data (Brandt et al., 2000; Mushotzky et al., 2000)) and a more significant contamination from the host galaxy.

Summarizing, from this first analysis we can propose different explanations for the reddening observed in the colors of our AGN sample:

(a) the contamination of the host galaxy is significantly reddening the measured colors of faint AGN;

(b) BLAGN are intrinsically redder when they are faint;

(c) the reddest color are due to the presence of dust.

We have tested these possibilities both by examining the median colors of our sample and by studying the global spectral energy distribution of each object.

Presence of dust

We computed the composite spectrum separately for the "bright" sub-sample ($M_{1450} < -22.15$) and the "faint" sub-sample ($M_{1450} > -22.15$) of AGN as previously defined. In figure 5.13 we show the comparison of these two VVDS composite spectra compared with the SDSS composite spectrum (solid curve). Even if also the "bright" VVDS composite (dotted curve) is somewhat redder than the SDSS one, it is clear from this plot that the

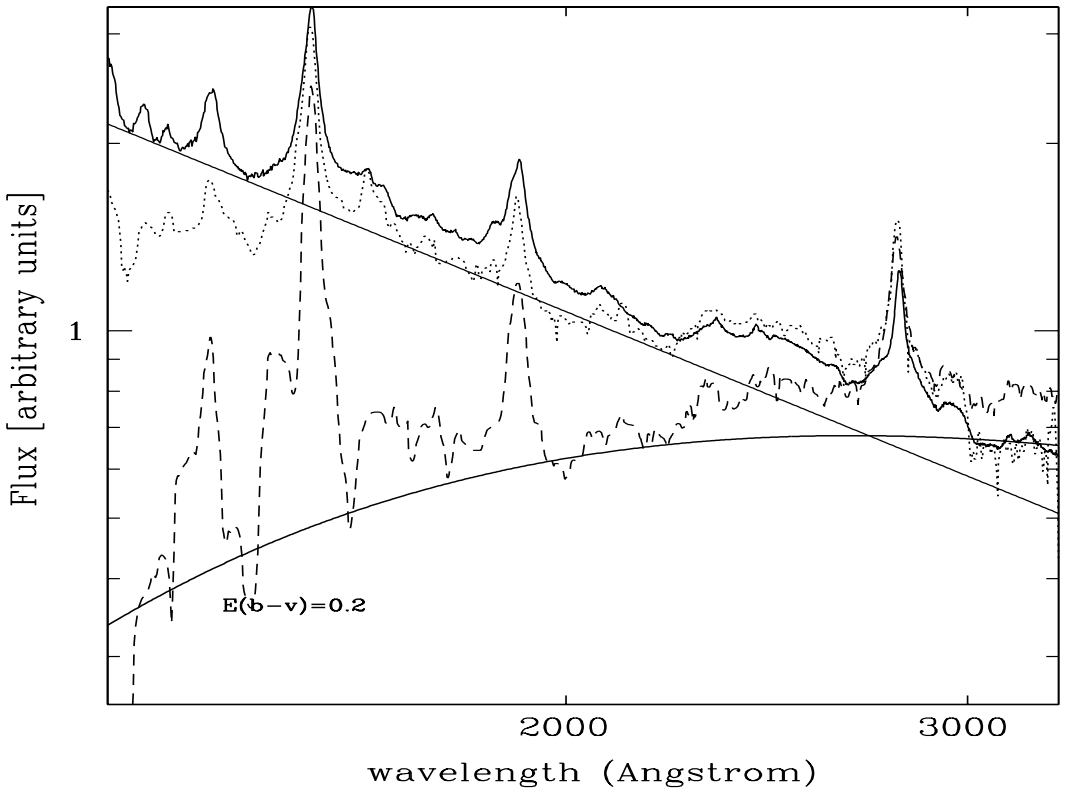

Figure 5.13. Composite spectra derived for our AGN with secure redshift in the 02h field, divided in a "bright" (19 objects at M_{1450} <-22.15, dotted curve) and a "faint" (31 objects at M_{1450} >-22.15, dashed curve) sample. The SDSS composite spectrum is shown with a solid line for comparison. The two solid lines correspond respectively to the power-law SDSS continuum fit ($f_\nu = \nu^{-\alpha}$) with α = 0.44 and to the same fit but dust-extincted according to a SMC-like dust-reddened law (Prevot et al., 1984) with E_{b-v} = 0.2.

main differences occur for faintest objects (dashed curve). Moreover the continuum of the faint sub-sample composite can be well reproduced by a power-law with α=-0.44 (corresponding to the SDSS continuum shape) with an extinction of E_{b-v} = 0.2. This test could be an evidence in favor of the hypothesis (c): the dust is responsible for the reddest colors of our faint objects.

Contamination by host-galaxy

The first evidence that led us to attribute the reddest colors to host galaxy contamination is that, for $\sim 50-60$ % of our reddest AGN (objects with $(B_{AB}-I_{AB})-(B_{AB}-I_{AB})_{SDSS} >$ 0.8), we detect the extended component of the BLAGN host galaxy in I band (see figure 5.11). Since, in this redshift range, the contribution from the host galaxies is expected to be more significant in the I band (corresponding to near UV-B rest-frame bands) than in the B band (corresponding to the far U rest-frame band), this leads us to believe that host galaxy contamination is contributing to give a redder color to our BLAGN.

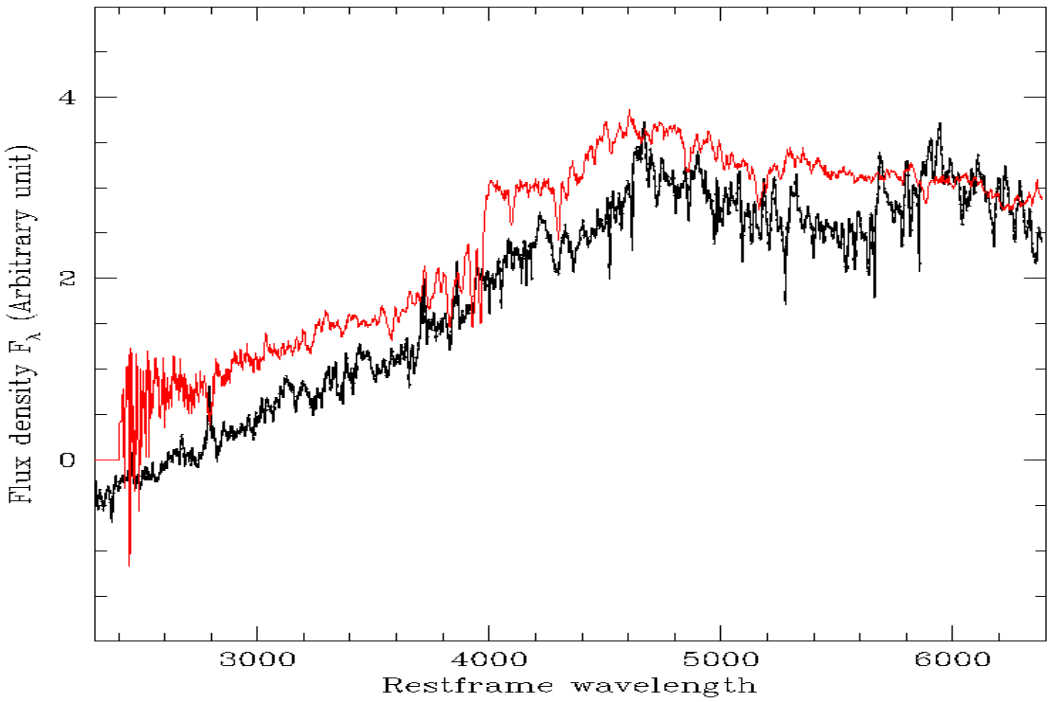

Figure 5.14. Difference between VVDS-AGN composite spectrum and the SDSS one. For comparison, the red line shows the template of early type galaxies as derived from the VVDS data

To further check this possibility, a new composite was computed excluding the extended objects found in our morphological analysis, for which we expect the contamination of the host galaxy to be stronger. This composite of point-like BLAGN is indeed found to have a bluer continuum than our composite with the complete sample.

Moreover, we subtracted the continuum of the SDSS composite spectrum from that of the VVDS composite; wavelength ranges corresponding to emission lines have been excluded. The resulting difference is shown in Figure 5.14 together with the spectrum of the template of early type galaxies as derived from the VVDS data (Contini et al., 2007). The good agreement of the overall shape of the two spectra is a strong evidence about the probable significant contamination by emission from the host galaxies.

Concluding, through this first analysis we are not able to discriminate between the different proposed hypotheses. Both contamination by the host galaxy and presence of dust could explain the reddest colors of our objects.

To better investigate this property we analyzed in detail the spectral energy distribution of each object.

5.6.1 Decomposition of active galactic nucleus and host galaxy components

The study of the Spectral Energy Distribution (SED) has been conducted only on the 02h deep field. In this field a wide multi-wavelength photometric coverage (from UV to IR) is in fact available. In addition to VVDS bands, we can use also data from GALEX, CFHTLS, UKIDSS and Spizer.

We examined the global spectral energy distribution of each object and we fitted the observed fluxes f_{oss} with a combination of AGN and galaxy emission, allowing also for the possibility of extinction of the AGN flux. In particular, we assume that:

$$f_{oss} = c_1 f_{AGN} \cdot 10^{-0.4 \cdot A_\lambda} + c_2 f_{GAL} \tag{5.1}$$

where A_λ is the dust extinction. Using a library of galaxy and AGN templates, by minimizing χ^2, we find the best parameters c_1, c_2 and A_λ to reproduce the observed flux of each object. Notice that we are not implying that our sample, on the whole, is composed only by objects having all these components. The only feature whose presence is certain *a priori* is of course the nuclear component: due to our selection criteria, all the selected sources do contain an active nucleus.

Modeling Nucleus and Host Galaxy

We used the AGN SEDs derived by Richards et al. (2006a) for a type–1 quasar sample selected combining IR and optical selection (259 quasars with both SDSS and Spitzer photometry). They derived different AGN SEDs: for the entire SDSS quasar sample and also for different sub-samples such as optically luminous and dim or optically red and blue quasars. All these SEDs constitute our AGN SED library and at each of them a SMC-like dust-reddening law (Prevot et al., 1984) of the form:

$$\frac{A_\lambda}{E_{b-v}} = 1.39\, \lambda_{\mu m}^{-1.2} \tag{5.2}$$

has been applied for different E_{b-v} (reddening factor) values.
The absorbed AGN flux is therefore:

$$f_{AGN}^{ext} = f_{AGN}\ 10^{-0.56\ E_{b-v}\ \lambda_{\mu m}^{-1.2}} \tag{5.3}$$

We show in figure 5.15 an example of AGN template (solid line) and the corresponding dust-reddened templates obtained by applying Equation 5.3 with different E_{b-v} values.

The galaxy library consists of a number of galaxy templates derived by the Bruzual & Charlot (2003) models based on the Salpeter Initial Mass Function (IMF; Salpeter 1955) and assuming solar metallicity. We used simple stellar population (SSP) models with ages spanning from 0.5 Gyr to 2 Gyr (see below for this choice of the age range). Moreover, starburst galaxies models (Devriendt et al., 1999) have been included to our library. No

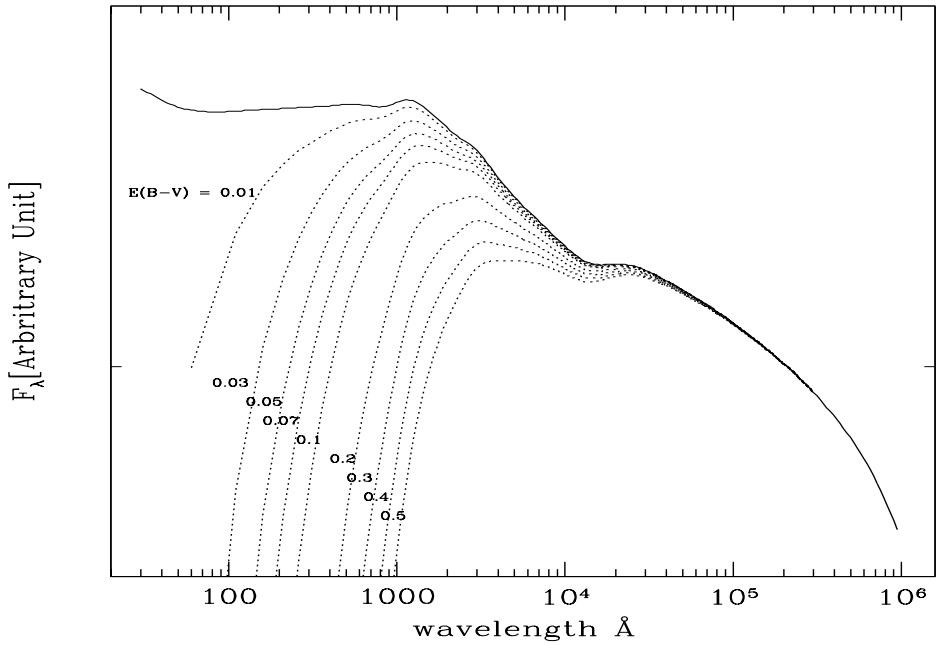

Figure 5.15. Example of an AGN template by Richards et al. (2006a) (solid line). The dashed curves correspond to the same SED dust-reddened using Equation 5.3 with different E_{b-v} values [0.01, 0.03, 0.05, 0.07, 0.1, 0.3, 0.4, 0.5].

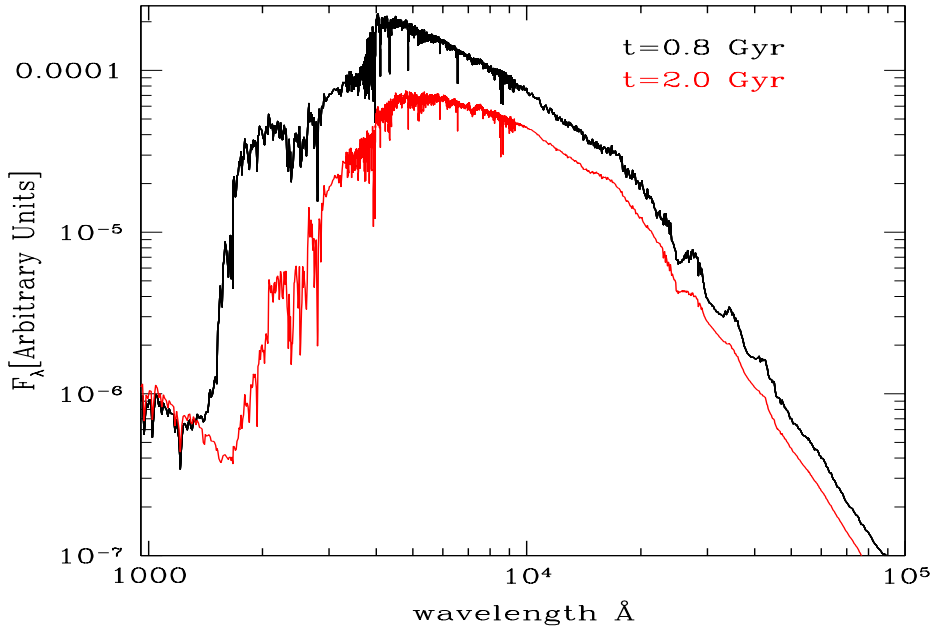

Figure 5.16. Examples of galaxy templates derived by the Bruzual & Charlot (2003) models based on the Salpeter Initial Mass Function (Salpeter, 1955) and assuming solar metallicity. The black and the red curves correspond to assume simple stellar population models with ages respectively of 0.8 Gyr and 2 Gyr .

internal dust extinction has been added in the galaxy. Figure 5.16 show two examples of galaxy templates derived using the Bruzual & Charlot (2003) models with ages of respectively 0.8 Gyr and 2 Gyr .

Studies on type–1 AGN host galaxies (e.g. Smith et al., 1986; McLeod & Rieke, 1995; Taylor et al., 1996; Schade et al., 2000; Jahnke et al., 2004) have shown that most of type–1 AGN are hosted by early-type galaxies. Moreover, Jahnke et al. (2004), studying a sample of 19 low-redshift ($z < 0.2$) quasar host galaxies, found strong evidence that, at least a sub-population of host galaxies, has significantly different color properties than their inactive counterparts. A large fraction of ellipticals in fact exhibit abnormally blue colors and SEDs not consistent with old, evolved stellar populations. Moreover, they found that, for almost all their objects, the best-fitting models are quite young (< 2 Gyr). The galaxy templates in our library are thus chosen with single stellar population of age spanning from 0.5 Gyr to 2 Gyr .

We found that for $\sim$37% of the objects, the observed flux is fitted by a typical AGN power law (pure AGN) while 44% of the sources require the presence of the host galaxy flux to reproduce the observed flux. In only 4% of the objects, the presence of dust is enough to describe the SED and, the remaining 15% of objects show instead both contributions (host galaxy contamination and presence of dust). If we restrict the analysis to the bright sample, the percentage of pure AGN increases to 68% and that of contaminated AGN decreases to 21%, for AGN with host galaxy contamination, and to 11%, for AGN contaminated by dust.

In figure 5.17 we show 4 examples of the resulting fits: (i) pure AGN; (ii) dust-extincted AGN; (iii) AGN contaminated by the host galaxy; (iv) dust-extincted AGN and contaminated by the host galaxy. The blue line corresponds to the AGN template, the red line to the galaxy template and, finally, the black line is the sum of the two. Since for $\lambda < 1216\,\AA$, corresponding to the Lyα line (dashed line), the observed flux is expected to decrease because of intervening absorption, all the photometric data at $\lambda <$1216 $\AA$ have not been considered in the fitting. The only requested constraint is that they lie below the fit.

Summarizing, the VVDS BLAGN have redder colors than the intrinsically brighter AGN and this is particularly true for the faintest VVDS AGN. We found that both presence of dust and contamination from the host galaxy are likely to be responsible for this reddening, even if it is not possible to exclude that at least some of the faint AGN are intrinsically redder than the brighter ones.

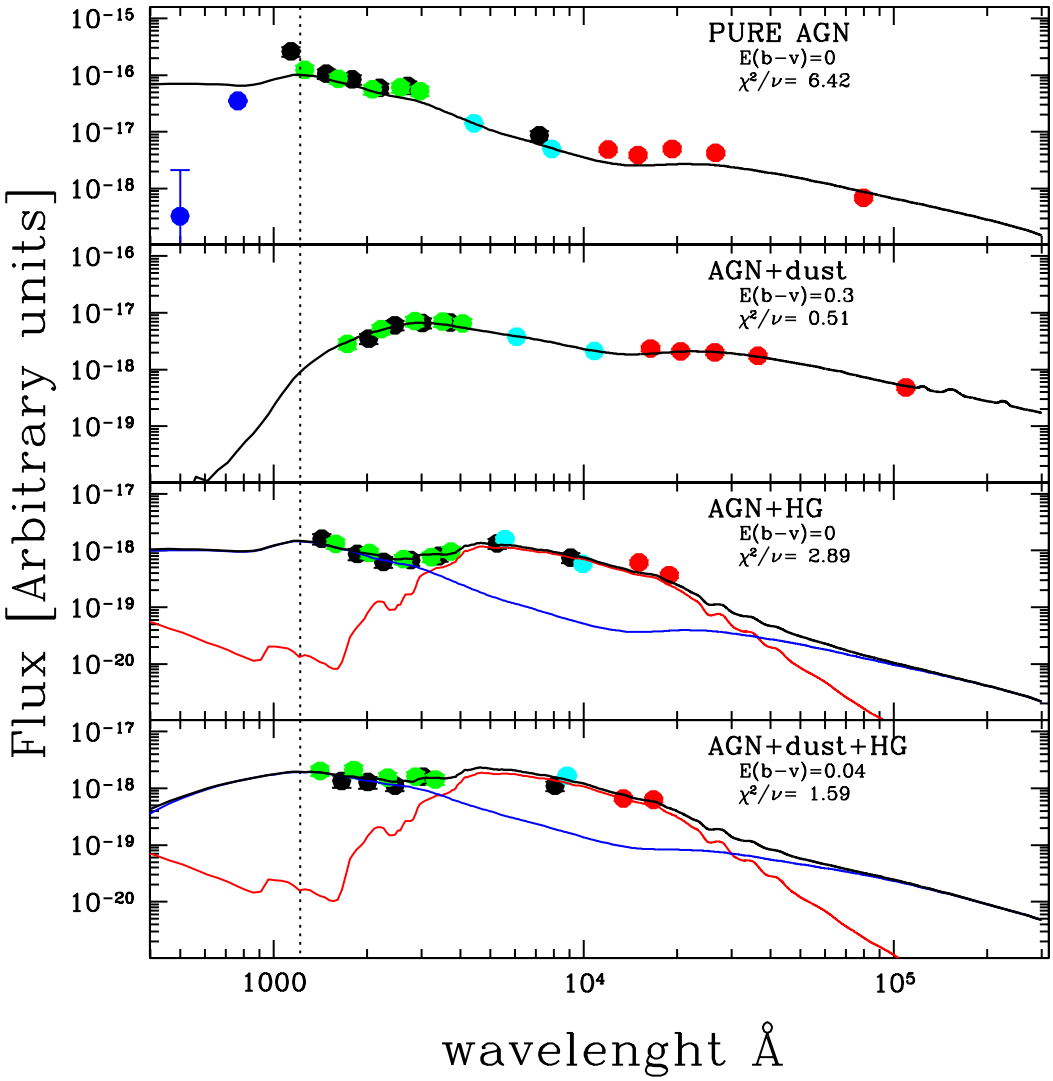

Figure 5.17. Four examples of different decompositions of the observed SEDs of our objects. Since for $\lambda < 1216$ Å, corresponding to the Lyα line (dashed line), the observed flux is expected to decrease because of intervening absorption, all the photometric data at $\lambda <$1216 Å have not been considered in the fitting. The only requested constraint is that they lie below the fit. The four fits shown in this figure correspond, from top to bottom, to pure-AGN, dust-extincted AGN, AGN and host galaxy, dust-extincted AGN and host galaxy.

Table 5.2. BLAGN with secure redshift (flags 14 and 13).

Object ID	α_{J2000}	δ_{J2000}	z	$flag$	I_{AB}	B_{AB}	V_{AB}	R_{AB}	$Morphology^{(*)}$
CDFS:	deep mode	10 AGN							
000037103	$03^h32^m37.47^s$	$-27^o40^m00.33^s$	0.6656	14	21.84	–	–	–	–
000037399	$03^h32^m38.14^s$	$-27^o39^m45.02^s$	0.8366	14	20.44	–	–	–	–
000073509	$03^h32^m02.47^s$	$-27^o46^m00.53^s$	1.6199	$14^{(S)}$	23.62	–	–	–	–
000023526	$03^h32^m43.25^s$	$-27^o49^m14.38^s$	1.9199	$14^{(S)}$	22.17	–	–	–	–
000028880	$03^h33^m03.62^s$	$-27^o45^m18.97^s$	1.2574	14	22.71	–	–	–	–
000029274	$03^h32^m30.23^s$	$-27^o45^m04.75^s$	0.7352	14	21.62	–	–	–	–
000018607	$03^h32^m18.26^s$	$-27^o52^m41.42^s$	2.8010	14	23.91	–	–	–	–
000025363	$03^h32^m59.85^s$	$-27^o47^m48.42^s$	2.5673	14	21.95	–	–	–	–
000033629	$03^h32^m25.17^s$	$-27^o42^m19.05^s$	1.6207	14	22.14	–	–	–	–
000031947	$03^h32^m00.37^s$	$-27^o43^m19.85^s$	1.0401	$14^{(S)}$	22.12	–	–	–	–
0226-04	deep mode	56 AGN							
020176565	$02^h25^m28.06^s$	$-04^o36^m41.59^s$	1.5039	14	23.24	23.62	23.61	23.26	–
020158952	$02^h26^m17.81^s$	$-04^o39^m08.50^s$	0.8738	14	21.41	22.82	22.16	21.99	extended
020086859	$02^h26^m29.62^s$	$-04^o49^m14.41^s$	1.1921	13	20.97	22.98	21.97	21.43	point-like
020213000	$02^h26^m47.88^s$	$-04^o31^m35.20^s$	1.2250	13	21.44	22.30	22.02	21.76	point-like
020212038	$02^h26^m08.40^s$	$-04^o31^m43.15^s$	2.2082	$14^{(F)}$	21.46	22.91	22.27	22.02	extended
020131908	$02^h26^m51.04^s$	$-04^o42^m56.55^s$	2.7813	14	22.34	23.08	22.75	22.76	extended
020210524	$02^h27^m07.55^s$	$-04^o32^m02.98^s$	1.5150	14	20.41	21.03	20.90	20.64	point-like
020120394	$02^h26^m59.92^s$	$-04^o44^m30.32^s$	1.6120	14	20.38	21.27	20.96	20.78	point-like
020114448	$02^h27^m00.99^s$	$-04^o45^m16.83^s$	1.6140	13	22.24	23.39	23.35	22.97	point-like
020118986	$02^h26^m54.53^s$	$-04^o44^m37.72^s$	3.3018	14	23.57	25.42	23.98	23.97	–
020118483	$02^h27^m36.06^s$	$-04^o44^m41.89^s$	1.2606	13	22.86	23.82	23.44	23.30	–
020188089	$02^h25^m25.68^s$	$-04^o35^m09.45^s$	2.1384	14	20.66	21.12	20.94	20.95	point-like
020147295	$02^h25^m29.19^s$	$-04^o40^m44.16^s$	1.5562	$14^{(F)}$	22.59	23.87	23.44	22.84	–
020169816	$02^h25^m45.04^s$	$-04^o37^m35.95^s$	3.5893	$14^{(F)}$	22.14	24.67	22.95	22.64	point-like
020190479	$02^h25^m45.55^s$	$-04^o34^m45.18^s$	0.1524	14	21.33	21.99	21.55	21.64	point-like
020268754	$02^h26^m09.63^s$	$-04^o24^m37.74^s$	2.7187	14	20.59	20.56	20.60	20.75	point-like
020164607	$02^h25^m32.46^s$	$-04^o38^m18.63^s$	2.9220	14	23.11	23.92	23.46	23.21	–
020179116	$02^h25^m34.98^s$	$-04^o36^m16.46^s$	3.3080	$14^{(F)}$	23.89	25.18	23.94	23.84	–
020237445	$02^h25^m57.38^s$	$-04^o28^m46.04^s$	1.2138	14	22.43	23.92	23.53	23.06	extended
020223153	$02^h26^m17.52^s$	$-04^o30^m29.27^s$	1.4777	$14^{(F)}$	20.65	21.18	21.05	20.94	point-like
020163018	$02^h26^m45.20^s$	$-04^o38^m30.58^s$	1.3208	$14^{(F)}$	23.11	23.89	23.62	23.29	–
020180665	$02^h26^m45.46^s$	$-04^o36^m15.43^s$	3.2619	14	18.14	21.09	19.32	19.03	point-like
020177875	$02^h26^m53.87^s$	$-04^o36^m27.21^s$	1.6821	13	22.53	24.01	23.65	23.36	–
020234610	$02^h26^m58.99^s$	$-04^o29^m06.02^s$	2.1645	13	23.87	26.05	25.11	24.74	–
020159510	$02^h27^m09.85^s$	$-04^o39^m02.21^s$	1.9309	14	21.97	22.73	22.41	22.44	point-like
020218399	$02^h27^m31.34^s$	$-04^o30^m50.26^s$	2.2255	14	22.19	22.91	22.39	22.53	point-like
020254511	$02^h27^m36.93^s$	$-04^o26^m31.30^s$	1.7466	14	20.66	20.76	20.84	20.85	point-like
020243922	$02^h27^m47.33^s$	$-04^o27^m53.20^s$	1.1203	14	21.29	22.02	21.71	21.60	point-like
020165108	$02^h26^m59.85^s$	$-04^o38^m12.68^s$	1.3219	13	23.09	24.70	24.04	23.78	–
020179225	$02^h27^m02.15^s$	$-04^o36^m15.96^s$	1.3860	13	22.39	23.90	23.50	23.01	point-like
020195823	$02^h27^m24.10^s$	$-04^o33^m55.72^s$	2.4250	$14^{(F)}$	23.38	24.19	23.61	23.85	–
020254576	$02^h25^m27.23^s$	$-04^o26^m31.02^s$	3.8527	14	21.15	23.33	21.78	21.44	point-like
020200020	$02^h25^m50.40^s$	$-04^o33^m24.00^s$	2.7373	13	21.91	21.95	22.10	21.73	point-like
020329650	$02^h26^m08.71^s$	$-04^o16^m34.53^s$	1.0498	14	20.84	21.52	21.14	20.96	point-like
020232397	$02^h26^m26.04^s$	$-04^o29^m27.88^s$	1.6280	$14^{(F)}$	22.69	23.72	23.31	23.15	–
020461765	$02^h26^m35.95^s$	$-04^o23^m21.81^s$	3.2831	14	22.89	24.62	23.01	22.87	–
020466135	$02^h26^m46.99^s$	$-04^o18^m37.56^s$	1.5806	14	21.13	21.29	21.56	21.05	point-like
020467962	$02^h26^m59.17^s$	$-04^o16^m55.89^s$	3.3247	13	23.59	25.22	23.96	23.80	–
020461459	$02^h27^m04.25^s$	$-04^o23^m37.77^s$	1.8211	13	21.60	23.50	22.92	22.41	point-like
020465339	$02^h27^m06.44^s$	$-04^o19^m24.30^s$	3.2852	14	21.09	21.77	21.31	20.99	point-like
020467628	$02^h27^m04.06^s$	$-04^o17^m09.77^s$	1.3582	13	21.35	21.97	21.82	21.61	point-like

Table 5.2. continued.

Object ID	α_{J2000}	δ_{J2000}	z	$flag$	I_{AB}	B_{AB}	V_{AB}	R_{AB}	$Morphology^{(*)}$
020205812	$02^h27^m23.84^s$	$-04^o32^m31.69^s$	2.8922	14	23.87	24.77	24.36	24.52	–
020208084	$02^h27^m29.24^s$	$-04^o32^m27.51^s$	2.2850	$14^{(F)}$	19.04	19.34	19.10	19.12	point-like
020277536	$02^h27^m53.85^s$	$-04^o23^m20.10^s$	3.6260	14	23.55	25.25	23.88	23.60	–
020278210	$02^h27^m40.00^s$	$-04^o23^m17.43^s$	1.7574	13	21.36	22.68	21.87	22.28	point-like
020239945	$02^h27^m31.14^s$	$-04^o28^m22.83^s$	2.4247	$14^{(F)}$	22.90	23.65	23.13	23.14	–
020351846	$02^h26^m30.84^s$	$-04^o13^m26.09^s$	3.5680	$14^{(F)}$	22.80	25.05	23.71	23.24	–
020367106	$02^h26^m34.71^s$	$-04^o11^m33.98^s$	1.3973	$14^{(F)}$	22.42	23.28	23.02	22.55	extended
020351277	$02^h25^m57.41^s$	$-04^o13^m39.43^s$	0.6061	14	19.83	20.60	20.39	20.32	extended
020258622	$02^h26^m20.06^s$	$-04^o25^m54.51^s$	1.3386	14	22.74	24.45	23.84	23.46	–
020286836	$02^h26^m22.17^s$	$-04^o22^m21.62^s$	2.0060	14	18.51	19.28	19.11	19.05	point-like
020291309	$02^h26^m31.23^s$	$-04^o21^m28.87^s$	1.9930	14	22.89	23.95	23.56	23.81	–
020465540	$02^h26^m44.48^s$	$-04^o19^m16.76^s$	2.7372	14	23.58	24.15	23.94	23.81	–
020302785	$02^h26^m24.63^s$	$-04^o20^m02.14^s$	2.2357	14	21.01	21.42	21.26	21.34	point-like
020364478	$02^h26^m49.41^s$	$-04^o11^m53.30^s$	1.1573	14	21.74	22.94	22.74	22.25	extended
020463196	$02^h27^m00.65^s$	$-04^o21^m49.00^s$	1.3875	14	23.27	24.49	24.42	23.91	–
1003+01	wide mode	18 AGN							
100122852	$10^h02^m11.17^s$	$+01^o22^m28.58^s$	1.8007	14	19.86	–	–	–	point-like
100110223	$10^h02^m48.14^s$	$+01^o20^m02.29^s$	1.8255	13	21.30	–	–	–	point-like
100210521	$10^h03^m27.33^s$	$+01^o35^m50.91^s$	1.1723	14	21.59	22.05	21.73	21.56	point-like
100139500	$10^h02^m57.37^s$	$+01^o25^m40.38^s$	1.2478	13	20.96	–	–	–	point-like
100126868	$10^h03^m08.80^s$	$+01^o23^m16.56^s$	2.3302	14	20.34	–	–	–	point-like
100105943	$10^h03^m46.33^s$	$+01^o19^m11.04^s$	3.5553	13	21.15	–	–	–	point-like
100290682	$10^h03^m11.33^s$	$+01^o47^m01.56^s$	1.5487	$14^{(F)}$	21.45	–	–	–	extended
100327652	$10^h03^m13.81^s$	$+01^o52^m13.97^s$	1.2173	14	22.39	23.85	23.43	22.90	extended
100232259	$10^h03^m30.37^s$	$+01^o38^m51.18^s$	1.7647	14	21.09	21.37	21.30	21.33	point-like
100190464	$10^h04^m25.14^s$	$+01^o33^m07.74^s$	1.0760	14	21.66	22.98	22.38	22.41	extended
100168207	$10^h04^m36.55^s$	$+01^o30^m05.86^s$	2.7152	14	22.40	22.38	21.84	22.14	point-like
100113463	$10^h04^m07.25^s$	$+01^o20^m38.90^s$	1.8436	14	20.47	–	–	–	point-like
100123590	$10^h04^m46.72^s$	$+01^o22^m39.10^s$	2.0963	13	21.47	–	–	–	point-like
100343840	$10^h04^m32.08^s$	$+01^o54^m24.12^s$	2.3666	$14^{(F)}$	19.75	20.68	20.40	20.15	point-like
100338914	$10^h04^m13.45^s$	$+01^o53^m41.38^s$	1.1584	14	19.73	20.15	19.80	19.78	extended
100245809	$10^h04^m00.36^s$	$+01^o40^m45.74^s$	3.0789	14	21.62	22.71	22.01	21.94	point-like
100241696	$10^h04^m11.84^s$	$+01^o40^m06.47^s$	1.1112	13	21.95	22.59	21.89	22.19	point-like
100451895	$10^h04^m38.01^s$	$+02^o09^m25.07^s$	1.7806	13	20.03	20.46	20.31	20.36	point-like
2217+00	wide mode	31 AGN							
220586430	$22^h14^m34.82^s$	$+00^o19^m24.18^s$	1.0285	14	20.35	–	–	–	point-like
220568559	$22^h14^m43.23^s$	$+00^o14^m16.29^s$	1.4980	13	22.10	–	–	–	point-like
220566905	$22^h14^m02.39^s$	$+00^o13^m49.58^s$	1.5285	13	22.28	–	–	–	point-like
220554336	$22^h14^m44.17^s$	$+00^o10^m02.54^s$	0.4470	14	21.02	–	–	–	point-like
220001963	$22^h13^m51.58^s$	$+00^o25^m01.30^s$	2.6801	14	22.19	–	–	–	point-like
220010371	$22^h14^m28.40^s$	$+00^o27^m32.40^s$	3.6952	14	21.79	–	–	–	point-like
220056847	$22^h14^m48.77^s$	$+00^o41^m16.67^s$	3.0015	14	21.38	–	–	–	point-like
220567825	$22^h15^m08.48^s$	$+00^o14^m04.38^s$	1.1601	13	21.07	–	–	–	point-like
220576817	$22^h15^m09.17^s$	$+00^o16^m42.38^s$	3.0957	14	21.81	–	–	–	point-like
220536609	$22^h15^m31.65^s$	$+00^o04^m18.31^s$	0.4970	14	21.10	–	–	–	extended
220041929	$22^h15^m09.54^s$	$+00^o36^m39.11^s$	1.4751	13	18.24	–	–	–	extended
220090821	$22^h15^m46.25^s$	$+00^o50^m58.51^s$	1.8326	13	20.40	–	–	–	point-like
220082140	$22^h15^m32.40^s$	$+00^o48^m36.29^s$	1.8484	$14^{(F)}$	20.58	–	–	–	point-like
220055529	$22^h15^m54.10^s$	$+00^o40^m55.47^s$	3.5941	13	21.42	–	–	–	point-like
220567863	$22^h16^m27.06^s$	$+00^o14^m02.32^s$	2.1610	14	20.80	–	–	–	point-like
220567224	$22^h16^m44.02^s$	$+00^o13^m48.54^s$	5.0042	14	20.07	–	22.90	–	point-like
220591287	$22^h16^m49.05^s$	$+00^o20^m46.27^s$	1.2968	$14^{(F)}$	22.30	23.47	23.32	–	extended
220580912	$22^h15^m56.66^s$	$+00^o17^m52.28^s$	3.0432	13	22.11	–	–	–	point-like
220107230	$22^h16^m56.10^s$	$+00^o56^m00.77^s$	1.0937	13	21.64	–	–	–	point-like

Table 5.2. continued.

Object ID	α_{J2000}	δ_{J2000}	z	*flag*	I_{AB}	B_{AB}	V_{AB}	R_{AB}	*Morphology*$^{(*)}$
220575888	$22^h17^m36.55^s$	$+00^o16^m23.09^s$	3.0755	14	21.25	22.16	21.50	–	point-like
220556037	$22^h17^m05.53^s$	$+00^o10^m19.85^s$	2.7422	14	19.46	20.52	20.29	–	point-like
220542377	$22^h17^m10.42^s$	$+00^o06^m04.72^s$	1.3097	13	21.12	22.24	21.95	–	point-like
220554600	$22^h17^m36.64^s$	$+00^o10^m05.86^s$	1.3689	$14^{(F)}$	20.65	21.21	21.00	–	point-like
220544855	$22^h17^m39.71^s$	$+00^o06^m52.80^s$	2.2934	$14^{(F)}$	20.91	21.97	21.61	–	extended
220044408	$22^h17^m34.47^s$	$+00^o37^m33.52^s$	2.9096	$14^{(F)}$	21.18	21.65	21.54	–	point-like
220093875	$22^h17^m48.64^s$	$+00^o51^m50.39^s$	1.3365	$14^{(F)}$	21.83	–	–	–	point-like
220081925	$22^h18^m00.42^s$	$+00^o48^m31.41^s$	1.2167	13	21.68	22.79	22.40	–	extended
220609820	$22^h18^m29.04^s$	$+00^o20^m24.32^s$	1.4794	$14^{(F)}$	21.52	22.04	21.86	–	extended
220610034	$22^h18^m14.20^s$	$+00^o20^m49.73^s$	1.5135	$14^{(F)}$	20.54	20.77	20.86	–	extended
220613346	$22^h18^m33.73^s$	$+00^o27^m09.76^s$	1.2530	$14^{(F)}$	20.39	21.63	21.25	–	extended
220098629	$22^h18^m01.51^s$	$+00^o53^m19.83^s$	2.5790	$14^{(F)}$	21.71	–	–	–	point-like

$^{(*)}$ Morphological classification for objects with $I_{AB} < 22.5$. Objects in the VVDS-CDFS field are not classified. (See Sect. 5.4.1);

$^{(F)}$ AGN re-observed in the 3800-6500 range with FORS1 in our follow-up program;

$^{(S)}$ Redshift confirmed by matching the catalog from Szokoly et al. (2004).

Table 5.3. AGN with a single emission line detected (flag 19). We list all the possible redshifts depending on the line identification (see below for more detail). Our best z solution is reported in boldface.

Object ID	α_{J2000}	δ_{J2000}	λ_{BL}	*z solutions*	I_{AB}	B_{AB}	V_{AB}	R_{AB}	*Morphology*$^{(*)}$
CDFS:	deep mode	2 AGN							
000031270	$03^h32^m57.74^s$	$-27^o43^m50.12^s$	7319.	0.1150^a **1.6150**^{b}	23.52	–	–	–	–
000017025	$03^h31^m54.30^s$	$-27^o53^m49.58^s$	6500.	**1.3220**^{b} 2.4050^c 3.1960^d	23.70	–	–	–	–
0226-04 :	deep mode	6 AGN							
020137737	$02^h26^m47.76^s$	$-04^o42^m04.06^s$	6320.	**1.2580**^{b} 2.3110^c 3.0800^d	23.78	24.58	24.14	24.16	–
020225567	$02^h27^m06.42^s$	$-04^o30^m14.34^s$	6558.	**1.3430**^{b} 2.4350^c	23.07	24.65	24.26	23.74	–
020281035	$02^h26^m12.30^s$	$-04^o22^m51.63^s$	6805.	0.0370^a **1.4310**^{b} 2.5650^c 3.3930^d	23.93	25.06	24.39	24.07	–
020375508	$02^h25^m48.99^s$	$-04^o10^m28.04^s$	5963.	1.1300^b **2.1240**^{c} 2.8500^d	22.54	23.25	22.98	23.04	–
020293248	$02^h26^m25.92^s$	$-04^o21^m12.73^s$	7335.	0.1180^a **1.6210**^{b}	23.25	24.79	24.54	24.13	–
020469530	$02^h26^m49.92^s$	$-04^o15^m17.44^s$	6701.	0.0210^a **1.3940**^{b} 2.5100^c 3.3260^d	23.50	24.69	24.35	24.28	–
2217+00:	wide mode	7 AGN							
220593613	$22^h14^m11.61^s$	$+00^o21^m29.15^s$	6893.	0.0500^a **1.4630**^{b} 2.6110^c	21.90	–	–	–	extended
220056092	$22^h13^m53.81^s$	$+00^o41^m06.90^s$	6100.	1.1790^b **2.1950**^{c}	22.08	–	–	–	point-like
220583713	$22^h15^m34.70^s$	$+00^o18^m42.01^s$	7352.	0.1200^a **1.6270**^{b}	21.88	–	–	–	point-like
220548678	$22^h15^m02.71^s$	$+00^o08^m10.56^s$	6766.	0.0310^a **1.4170**^{b} 2.5440^c	21.97	–	–	–	point-like
220023681	$22^h17^m46.44^s$	$+00^o31^m26.58^s$	6956.	0.0600^a **1.4850**^{b} 2.6440^c	21.71	24.33	23.25	–	point-like
220551735	$22^h18^m05.78^s$	$+00^o09^m12.66^s$	8056.	0.2270^a **1.8780**^{b}	21.12	21.73	21.72	–	point-like
220234909	$22^h18^m13.40^s$	$+00^o48^m54.05^s$	6407.	**1.2890**^{b} 2.3560^c 3.1360^d	21.88	23.40	22.55	–	extended

$^{(*)}$ Morphological classification for objects with $I_{AB} < 22.5$. Objects in the VVDS-CDFS field are not classified. See Sect. 5.4.1

^{a} Emission line identified as Hα.

^{b} Emission line identified as MgII.

^{c} Emission line identified as C III].

^{d} Emission line identified as CIV .

Chapter 6

AGN Number Counts

In this Chapter I will present the derived surface density as a function of the apparent magnitude $I_{\rm AB}$ derived for the VVDS-BLAGN sample.

To derive the real number of objects in a given observed sky area, it is important to quantify the efficiency of the adopted selection method. In general, the efficiency with which AGN can be detected by a particular observing strategy is function of several parameters (e.g. luminosity, redshift, SED).

6.1 VVDS selection function for BLAGN

Given the adopted selection method for the VVDS-BLAGN (see Section 5.1), to obtain the total number of BLAGN in the VVDS fields, we have to correct our sample for the fraction of BLAGN in the photometric catalog, which have not been spectroscopically observed and for those, spectroscopically observed, but not correctly identified from their spectrum. Our incompleteness function is indeed made up of two terms linked, respectively, to the selection algorithm and to the spectral analysis: the Target Sampling Rate (TSR) and the Spectroscopic Success Rate (SSR).

The correction is then performed applying to our BLAGN two statistical weights, w^{TSR} and w^{SSR}.

6.1.1 Treatment of non-targeted BLAGN: w^{TSR}

The *Target Sampling Rate* is the fraction of objects in the photometric catalog inside our targeted area which have been spectroscopically observed.

As already mentioned in Section 4.2.3, SPOC (the tool for the automatic positioning of slits) uses the projected size of the object along the slit $x-radius$, to maximize the number of slits. It is defined as: $xradius = (n_{pxl} + 0.5) \times 0.205$, where 0.205 arcsec/pxl is the VIMOS spatial resolution and n_{pxl} is an integer number (n_{pxl} = 1,2,3,...) that quantifies the projected radius size in pixels (Bottini et al., 2005). The TSR of these

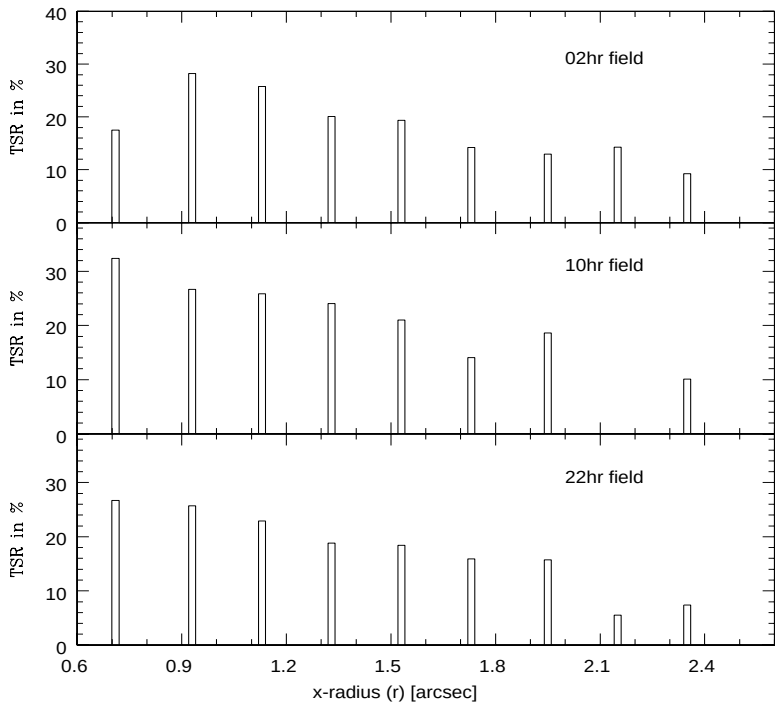

Figure 6.1. *Target Sampling Rate* (ratio between observed objects and the total photometric sources) as a function of x-radius for the 02h, 10h and 22h fields.

fields is presented in figure 6.1. As a consequence of the optimization process, small size objects, like AGN, are favored against the large size ones. For them the TSR runs from 30% to 20%. For the CDFS instead, a constant value of the x-radius was considered. To balance for non-targeted BLAGN we apply to our BLAGN the weight $w^{TSR} = \frac{1}{TSR}$.

6.1.2 Treatment of misclassified AGN: w^{SSR}

The *Spectroscopic Success Rate* (SSR) is the probability of a spectroscopically targeted AGN to be securely identified. It is a complex function of the BLAGN redshift, apparent magnitude and intrinsic spectral energy distribution. In order to evaluate the SSR, we simulated 20 Vimos pointings, for a total of 2745 spectra. The simulations incorporate the major instrumental effects of Vimos observations, including sensitivity curve, fringing in the redmost part of the spectra, sky background and contamination by zeroth-orders. Each spectrum has been simulated using the SSDS composite spectrum as a template. Redshifts and magnitudes were drawn at random in the ranges $0 < z \leq 5$ and $17.5 \leq I \leq 24$ respectively. The spectra were then analyzed and classified in the same way as the real spectra, except that we did not try to resolve cases where a single line was present; we simply checked whether the BLAGN nature of the object could be detected in the spectrum or not.

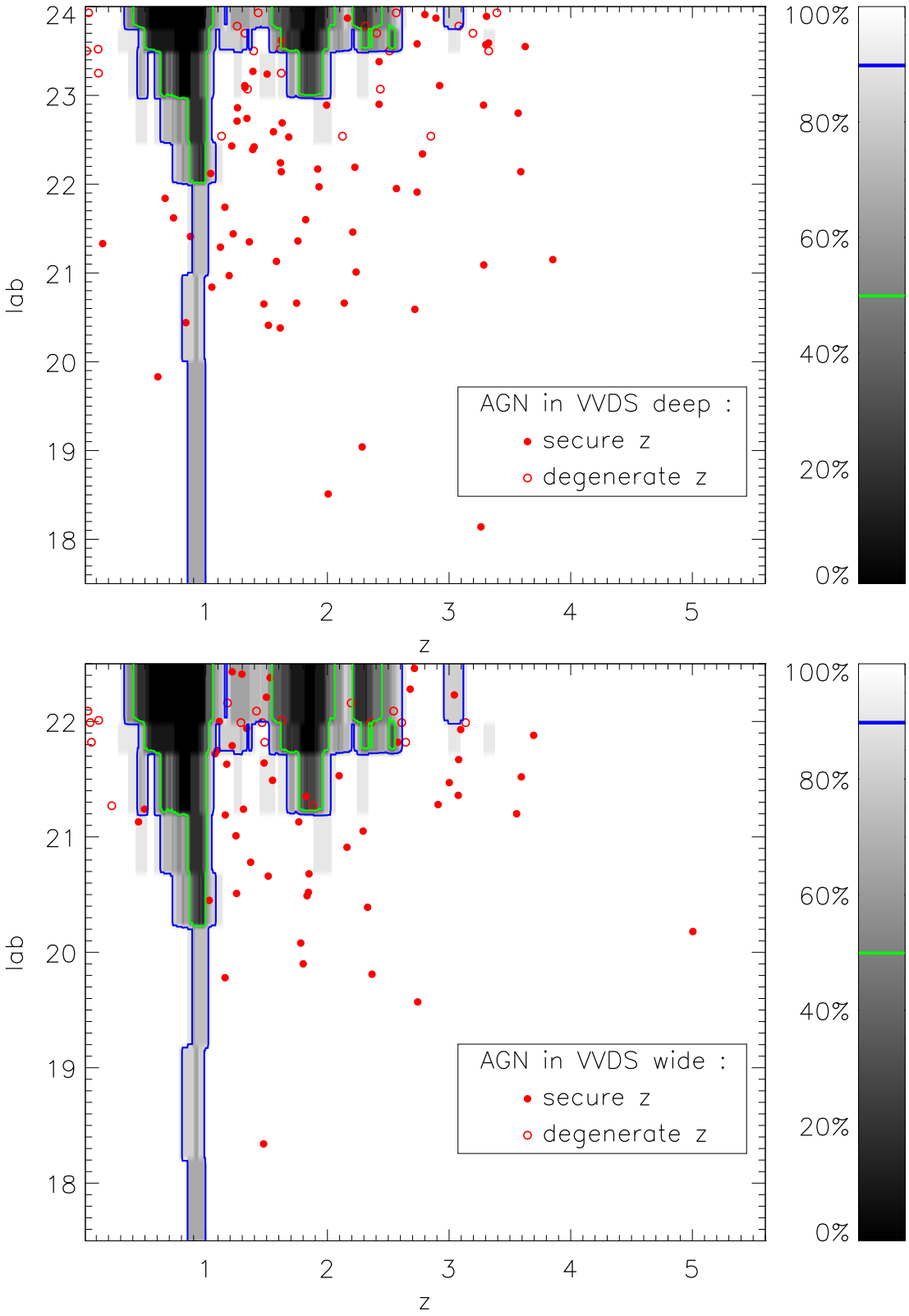

Figure 6.2. *Spectroscopic Success Rate* for BLAGN in the VVDS deep (top) and wide (bottom) sample as a function of redshift and apparent magnitude. Contour lines are drawn for 90% and 50% of identification success rate. The location of BLAGN with a secure redshift is reported with filled dots. BLAGN with a degenerate redshift are plotted at their different redshift solutions with open circles.

Figure 6.2 presents the resulting SSR as a function of redshift and apparent I_{AB} magnitude in the deep and wide fields. To correct for missed BLAGN we apply to our objects the weight $w^{SSR} = \frac{1}{SSR}$. Objects for which the broad-line equivalent width (EW) is larger than in the SDSS composite spectrum will be over-estimated by our method and, on the contrary, objects with weaker broad emission lines will be under-estimated.

The global correction for our selection function is obtained by applying to each of our objects the product of these two weights, i.e. $w^{TSR} \times w^{SSR}$.

6.2 Coherent sample

Our sample consists of objects found in 4 fields, with two different limiting magnitudes, I_{AB}=24.0 for the deep samples (02h field and CDFS) and I_{AB}=22.5 for the wide samples (10h and 22h fields). In the VVDS samples, as shown in Figure 5.5, the wide and deep samples span essentially the same redshift interval. This means that through the deep sample we are mainly exploring the fainter part of the luminosity function at each redshift.

Avni & Bahcall (1980) have shown that the most efficient way to statistically analyze samples derived from areas with different flux limits is through what they call *"Coherent Analysis of Independent Samples"*. In this analysis it is assumed that each object, characterized by an observed redshift z_i and intrinsic luminosity L_i, could have been found in any of the survey areas for which its observed magnitude is brighter than the corresponding flux limit. This means that, for our total sample, we consider an area of:

$$\mathcal{A}_{tot}(m) = \mathcal{A}_{deep} + \mathcal{A}_{wide} = 1.72 \text{ deg}^2 \qquad \text{for} \quad 17.5 < I_{AB} < 22.5 \tag{6.1}$$

and

$$\mathcal{A}_{tot}(m) = \mathcal{A}_{deep} = 0.62 \text{ deg}^2 \qquad \text{for} \quad 22.5 < I_{AB} < 24.0 \tag{6.2}$$

6.3 AGN Surface Density

Since the objects to be observed spectroscopically in the VVDS are selected on the basis of their I_{AB} band magnitude, we have computed the BLAGN cumulative surface density in this band.

Taking into account the correction for the global selection function, and computing the coherent area by using Equations 6.1 and 6.2, the algorithm for the cumulative surface density is the following:

$$\mathcal{N}(\leq I_{AB}) = \frac{1}{\mathcal{A}_{wide} + \mathcal{A}_{deep}} \sum_{i, I_{AB,i} \leq I_{AB}} w_i^{TSR} w_i^{SSR} \qquad \text{if} \quad I_{AB} \leq 22.5 \tag{6.3}$$

$$\mathcal{N}(\leq I_{AB}) = \mathcal{N}(\leq 22.5) + \frac{1}{\mathcal{A}_{deep}} \sum_{i,22.5<I_{AB,i}\leq I_{AB}} w_i^{TSR} w_i^{SSR} \qquad \text{if} \quad I_{AB} > 22.5 \qquad (6.4)$$

where $\mathcal{A}$ (*deep* and *wide*) is the geometrical area targeted by the spectroscopic survey (*deep* and *wide*), i.e. the area covered by the different VIMOS fields of view corrected for the area masked in our photometric catalogs, and the sum is running over all BLAGN i with magnitude I_i less or equal to I_{AB}.

The upper panel of Figure 6.3 presents the cumulative surface density derived in the VVDS individual fields with the corresponding Poissonian error bars (Gehrels, 1986). Although some differences in the counts in different fields are visible, the surface densities measured in all our fields at $I_{AB} = 22.5$, (corresponding to the magnitude limit of the wide fields) are all consistent, within the errors, with each other. We conclude that the error induced by cosmic variance is smaller than our Poissonian noise. We compute a single $log\mathcal{N} - I_{AB}$ curve by merging the data from the four fields into a single coherent sample (Avni & Bahcall, 1980, see Section 6.2).

At the limit of our deep fields ($I_{AB} < 24.0$) our measured surface density of BLAGN is $\sim 472 \pm 48$ per square degree and the correction applied for misclassified BLAGN corresponds to $\sim 10\%$ of this value. The differential surface density computed for the total sample is shown in Figure 6.4. In this plot the different points and associated errors are independent from each other. This Figure suggests a significant turn-over in the slope of the counts at $I_{AB} \sim 21.5$. At $I_{AB} \gtrsim 21.5$ the differential number counts are still increasing with magnitude, but at a much lower rate than at brighter magnitudes. This effect is seen, although less clearly, in the continuous flattening with magnitude of the integral number counts in Figure 6.3.

Comparison with other spectroscopic surveys is not straightforward since most of the optical QSO surveys are based on much shallower B-band flux limited samples and most of them are not complete over the entire redshift range due to their different selection criteria. The CFRS is an exception with essentially the same selection function as the VVDS (i.e. a flux limited sample in the I band with no color nor morphological selection). Although it contains only 6 BLAGN at a magnitude limit of $I_{AB} < 22.5$ (see Schade et al., 1996), the surface density resulting from these objects is in excellent agreement with our current measurement (see Figure 6.3, lower panel).

The surface density derived from the recent SDSS Faint Quasar Survey (SFQS, Jiang et al., 2006) is also reported in Figure 6.3, lower panel. This survey selects AGN over $0 < z < 5$ up to $g = 22.5$. The surface density, corrected for completeness, is computed in the g band (Jiang, private communication) and approximately translated to the I_{AB} band assuming the mean color term observed in our sample: $\langle I_{AB} - g \rangle = -0.7$. The VVDS and SFQS number counts at $I_{AB} \sim 21.8$ are in good agreement.

With a limiting magnitude similar to ours the only other comparable sample is the

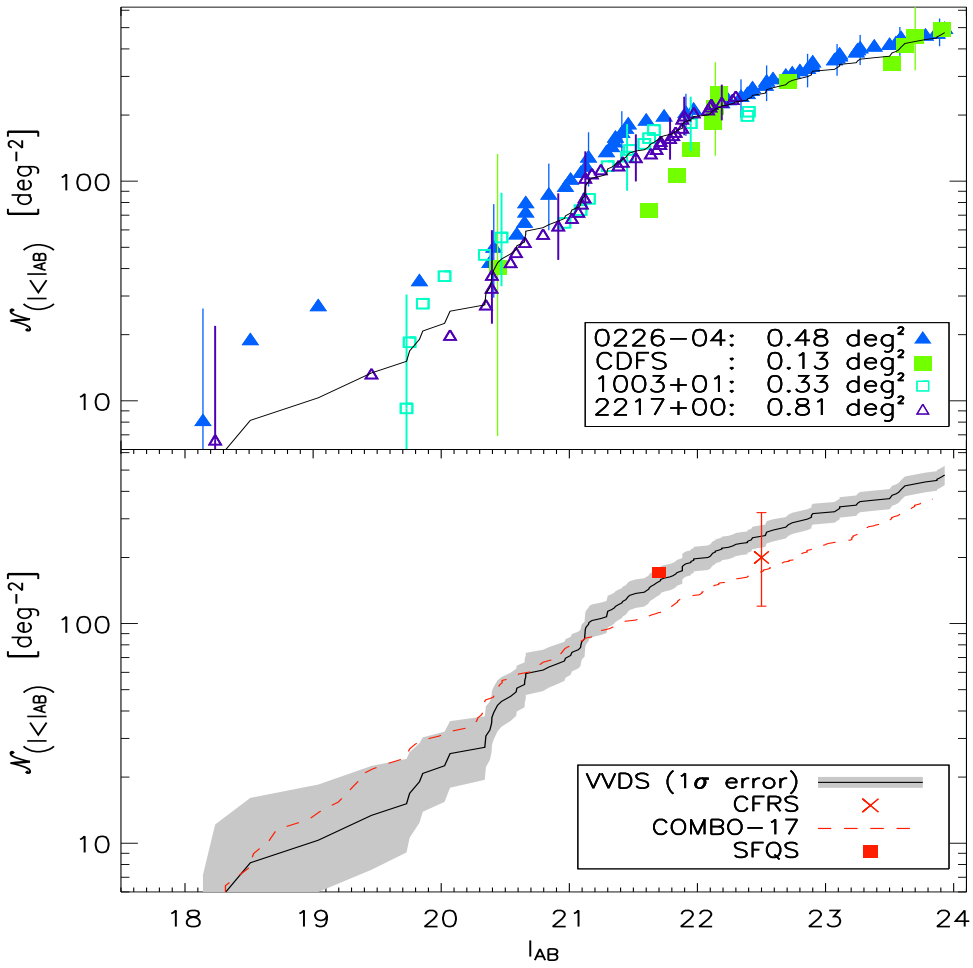

Figure 6.3. BLAGN cumulative surface density in the VVDS sample. Error bars are the 1-σ Poissonian errors. Top panel: Observed surface density in the individual fields and in the total sample (solid line). For readability error bars are reported each 5 data points. Bottom panel: comparison of the VVDS total surface density with CFRS, SFQS and COMBO-17 survey results.

I_{AB}	N	$\mathcal{N}(\leq I_{AB})$
19	3	10
20	9	22
21	29	71
22	76	196
23	108	327
24	130	472

Table 6.1. BLAGN number counts as function of I_{AB} magnitude. N is the actual number of BLAGN in the VVDS survey while $\mathcal{N}(\leq I_{AB})$ is the cumulative surface density of BLAGN (objects / square degree) corrected for incompleteness.

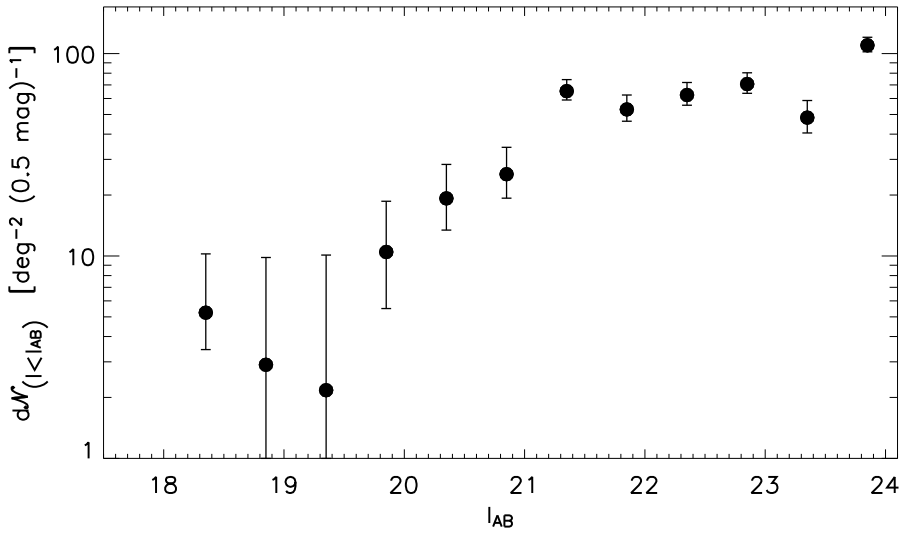

Figure 6.4. BLAGN differential surface density in the VVDS sample. Error bars are the 1σ Poissonian errors.

COMBO-17 one (see Wolf et al., 2003b), which is however based on photometric selection of AGN, with a small fraction of spectroscopic confirmation. For comparison with our sample, we have obtained the complete COMBO-17 sample cumulative counts, without redshift restriction (Wisotzki, private communication). Since this sample is selected in R-band, we apply a global color term of -0.16 magnitude to translate their surface density to our I_{AB} reference system. This color term corresponds to the mean $I_{AB} - R_{vega}$ color observed for our objects. In addition, a dozen of BLAGN are observed in both the VVDS and the COMBO-17 samples. The mean color term of these objects is measured to be -0.12.

The result is presented in the lower panel of Figure 6.3. Our number counts are statistically consistent with COMBO-17 for magnitudes brighter than 21.5. At fainter magnitude our counts are systematically higher by $\sim 30-40\%$. This can be explained by incompleteness in the COMBO-17 at low redshift in the regime where the host galaxy contamination becomes non-negligible. This is the reason why the published version of the COMBO-17 AGN sample was restricted to $z > 1.2$.

Considering different redshift ranges and computing the surface density in the R-band (Figure 6.5), we find that, for $z > 1.2$, $\mathcal{N}(R \leq 24) = 340 \pm 47$, which compares well with the published result of COMBO-17 sample: $\mathcal{N}(R \leq 24) = 337$. However,, while at $z > 2.2$, our estimated surface density is in agreement with the COMBO-17 one, in the intermediate redshift bin ($1.2 < z < 2.2$) we do not observe a flattening of the number counts towards faint magnitudes. This effect might result from some incompleteness of the COMBO-17 sample in this redshift range at the faintest magnitudes (we detect in our sample contribution of host galaxy up to $z \sim 1.6$: see Figure 5.8). This difference is also

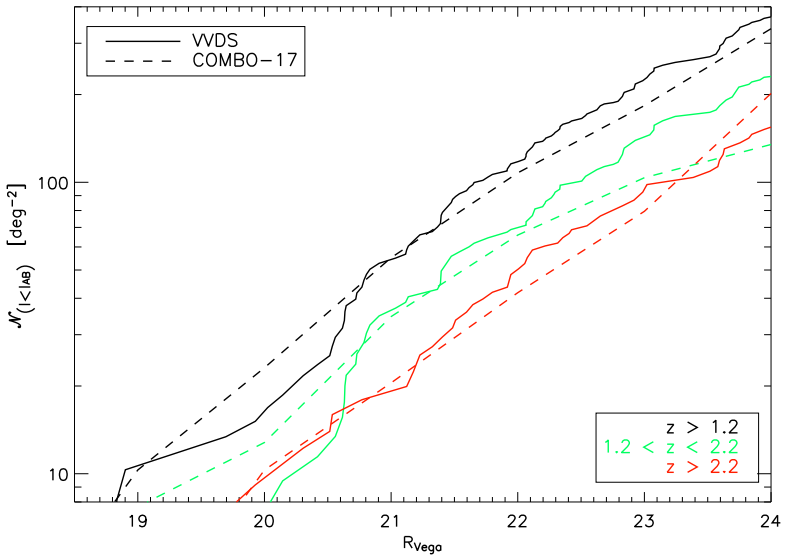

Figure 6.5. Comparison of the BLAGN cumulative density of the VVDS and the COMBO-17 sample in different redshift bins.

observed in the lower redshift bin of our luminosity function (Section 8.5.1).

Chapter 7

Evolution of type–1 AGN

The major aim of cosmology is to study how our Universe is evolving in time. This is done by studying the evolution of its content, from galaxies and AGN to large scale structures. The discovery of a tight relation between black holes mass and velocity dispersion of their host galaxy suggests that the evolution of the growth of SMBH and their host galaxy are linked together. Hence, the understanding of the history of accretion in the Universe and of the formation of massive black holes and their host galaxies relies on the measurement of the AGN space density and evolution.

7.1 Luminosity function

A useful way to statistically describe the AGN activity along the cosmic time is through the study of their luminosity function (LF), whose shape, normalization and evolution are key observational quantities for understanding the origin and accretion history onto supermassive black holes, which are now believed to occupy the centers of most galaxies. The luminosity function corresponds to the density of objects of a given absolute magnitude, at a given redshift:

$$\Phi(M,z) = \frac{dN(M,z)}{dMdV} \ , \tag{7.1}$$

where dN is the number of objects with magnitude $M \in [M, M+dM]$ and redshift $z \in [z, z+dz]$, this redshift interval enclosing the elementary comoving volume dV. The comoving volume at a given redshift is the volume scaled to the value it would have today (at z=0). Since the Universe is larger today than it was at a redshift z by a factor 1+z, the space density of QSOs would be greater in the past even if their numbers and luminosities have remained constant. The use of the comoving volume removes the effect of the expanding Universe so, the comoving space density of a constant number of non-evolving objects does not change as the Universe expands. A change in this density implies that the number of objects is varying or that the objects are evolving (or both).

7.1.1 The V/V_{max} test

Despite many difficulties encountered in the determination of the space density and luminosity function of QSOs (i.e. results are sensitive to many different types of selection effects), it was clear even since the first decade of QSO research, that the comoving density of QSOs varies strongly with redshift.

In 1968, Schmidt (1968) highlighted this evidence through the "*luminosity-volume test*" or more commonly, the "V/V_{max} test". The basic idea of this test is the following: for an object i of absolute magnitude M_i selected in a flux limited survey, one can compute the maximal luminosity distance $d_{max,i}$ for which this object could have been detected in this sample. We define $V_i = \frac{4\pi r_i^3}{3}$ as the volume enclosed by the actual distance d_i of this object and $V_{max,i} = \frac{4\pi r_{max,i}^3}{3}$ as the volume enclosed by $d_{max,i}$. For a sample of objects homogeneously distributed, the probability to observe this object i with $V_i < \frac{V_{max,i}}{2}$ is the same as to observe it with $V_i > \frac{V_{max,i}}{2}$ and hence the mean value $\langle V/V_{max}\rangle$ should be 0.5. In his sample, Schmidt measured $\langle V/V_{max}\rangle \sim 0.7$ and interpreted this result as an evolution of the density of QSO with redshift. This model is referred as *pure density evolution*. In 1976, Mathez (1976) showed that this result could be interpreted in terms of luminosity evolution as well. In this model, referred as *pure luminosity evolution*, highly luminosity quasars observed at redshift 2 are seen as a parent population, fading with time, of today's quasars characterized by a lower luminosity.

This simple test provided clear evidence for evolution of the QSO population per comoving volume over cosmological time scales. This means that the LF is function of redshift and it is indeed necessary to consider the distribution of luminosities or absolute magnitudes over relatively restricted redshift intervals. Moreover, to examine the distribution over two parameters, L and z, a large sample of objects is required to avoid problems of small-number statistics.

7.1.2 Computation and Parameterization of the Luminosity Function

If AGN are drawn from a 'volume-limited' sample, the luminosity function is simply computed from:

$$\Phi(M)\Delta M = \sum_{M-\Delta M/2}^{M-\Delta M/2} \frac{1}{V_{max}} = \frac{N_M}{V_{max}} \tag{7.2}$$

where N_M is the number of AGN in the sample with absolute magnitudes between $M - \Delta M/2$ and $M + \Delta M/2$. More often AGN are drawn from 'flux-limited' or 'magnitude-limited' samples. The total volume of space surveyed is thus a function of the absolute magnitude M. We must indeed replace V_{max} with $V_{max}(M)$ to account for the fact that more luminous objects can be seen at larger distances than fainter sources and are thus overrepresented in a magnitude-limited sample (Malmquist bias, Mihalas & Binney,

1981). Weighting each individual AGN by the reciprocal of the volume over which it could have been found corrects this problem. We then must normalize each QSO by its accessible volume. Finally, as we know that the space density of AGN changes with time, we compute the luminosity function as a function of redshift as well:

$$\Phi(M,z)\Delta M = \sum_{\substack{M-\Delta M/2 \\ z-\Delta z/2}}^{\substack{M+\Delta M/2 \\ z+\Delta z/2}} \frac{1}{V_{max}(i)} \tag{7.3}$$

As suitable samples of AGN started to be accumulated, it became evident that, at least at low redshift, the QSO luminosity function is steeper at high luminosity than at low luminosity. This led to a simple parameterization of the luminosity function as a two-component power law, with different slopes at high and low luminosities and a 'break-point' where the slope changes. A similar description has been used in the past for the luminosity function of normal galaxies (e.g Abell, 1962). A better mathematical formulation (since the derivative is not discontinuous at the break point) was proposed by Marshall (1987) and, expressed in luminosity, has the following form:

$$\Phi(L,z) = \frac{\Phi_L^*/L^*}{(L/L^*)^{-\alpha} + (L/L^*)^{-\beta}} \tag{7.4}$$

where Φ_L^* is a normalization constant proportional to the number of AGN per Mpc^3, L^* is the characteristic luminosity where the slope of the luminosity function is changing and α and β are the double power law slopes. Equation 7.4 can be expressed in absolute magnitude by defining

$$M = M^*(z) - 2.5\log L/L^*(z) \tag{7.5}$$

and using the transformation

$$\Phi(M,z)dM = \Phi(L,z)\left|\frac{dL}{dM}\right|dM. \tag{7.6}$$

The luminosity function, expressed in absolute magnitude, is thus:

$$\Phi(M,z) = \frac{\Phi_M^*}{10^{0.4(\alpha+1)(M-M^*)} + 10^{0.4(\beta+1)(M-M^*)}} \tag{7.7}$$

where $\Phi_M^* = \Phi_L^* \cdot \left|ln10^{-0.4}\right|$.

7.2 AGN evolution: main results

In the parameterizations described in Equations 7.4 and 7.7, $L^*(z)$ (or $M^*(z)$) and $\Phi^*(z)$ are the evolutionary parameters which allow us to distinguish between simple evolutionary models such as Pure Luminosity Evolution (PLE) and Pure Density

Evolution (PDE).
This means that, for a PLE model:

$$L^*(z) = L^*(0) \cdot e(z) \tag{7.8}$$

and equivalently

$$M^*(z) = M^*(0) - 2.5 \log e(z), \tag{7.9}$$

while for a PDE model:

$$\Phi^*(z) = \Phi^*(0) \cdot e(z) \tag{7.10}$$

where $e(z)$ (i.e. the redshift dependence) can be parameterized in different ways. Here we report some of the most commonly used evolutionary laws:

$$\text{(a)} \qquad e(z) = (1+z)^p \, e^{-\left(\frac{p\,z}{1+z_c}\right)}$$

$$\text{(b)} \qquad e(z) = \begin{cases} (1+z)^p & if \quad z < z_c \\ (1+z_c)^p \left(\frac{1+z}{1+z_c}\right)^q & if \quad z > z_c \end{cases} \tag{7.11}$$

$$\text{(c)} \qquad e(z) = 10^{k_1 z + k_2 z^2}$$

Although the PLE and PDE models should be mainly considered as mathematical descriptions of the evolution of the luminosity function, two different physical interpretations can be associated to them: either a small fraction of bright galaxies harbor AGN, and the luminosities of these sources change systematically with time ('luminosity evolution'), or all bright galaxies harbor AGN, but at any given time most of them are in 'inactive' states. In the latter case, the fraction of galaxies with AGN in an 'active' state changes with time ('density evolution')

At $z \lesssim 2.5$, the luminosity function of optically selected AGN has been well studied for many years (Boyle et al., 1988; Hewett et al., 1991; Pei, 1995; Boyle et al., 2000; Croom et al., 2004). Up to now, the PLE model is the preferred description for the evolution of optically selected QSOs, at least at low redshift ($z < 2$). In Figure 7.1, we report the optical QSO luminosity function, as derived by Croom et al. (2004) for the *2dF Quasar Redshift Survey* (2Qz) AGN sample. The luminosity function is presented in six redshift intervals and is described by a double power law with luminosity evolution with a quadratic dependence in redshift (as Equation 7.11(c)), with $L^*_B(z) \propto 10^{1.39z - 0.29z^2}$.

Studies on high redshift AGN samples (Warren et al., 1994; Kennefick et al., 1995; Schmidt et al., 1995; Fan et al., 2001; Wolf et al., 2003b; Hunt et al., 2004) have shown that the number density of quasars declines rapidly from $z \sim 3$ to $z \sim 5$. Since the size of complete and well studied samples of quasars at high redshift is still relatively small, the rate of this decline and the shape of the high redshift luminosity function is not yet as well constrained as at low redshift. For example, Fan et al. (2001), studying a sample of 39 luminous high redshift quasars at $3.6 < z < 5.0$, selected from the commissioning data

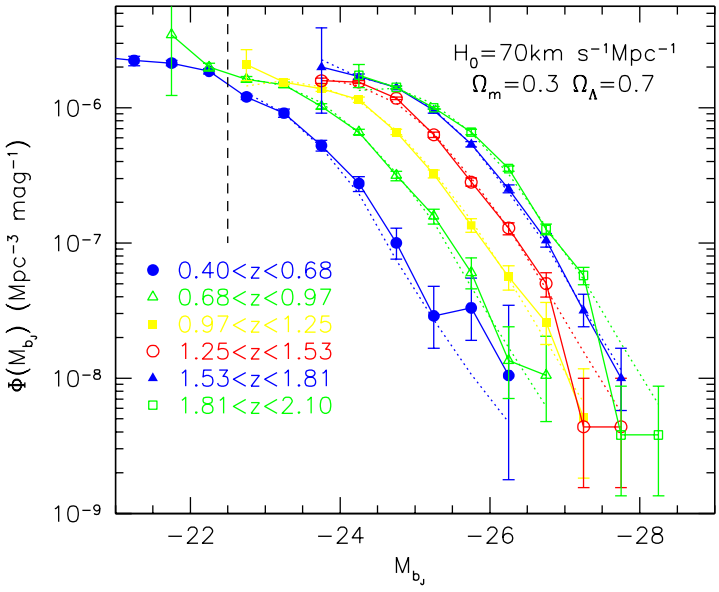

Figure 7.1. The optical QSO luminosity function for the *2dF Quasar Redshift Survey* (2Qz) AGN sample in six redshift intervals (figure 20 of Croom et al., 2004)

of the Sloan Digital Sky Survey (SDSS), found that the slope of the quasar luminosity function evolves with redshift, becoming flatter at high redshift, and that the quasar evolution from $z = 2$ to $z = 5$ cannot be described as a pure luminosity evolution. A similar result on the flattening at high redshift of the luminosity function slope for luminous quasars has been recently obtained by Richards et al. (2006c) from the analysis of a much larger sample of SDSS quasars. At $z < 3$ they estimate, in agreement with Croom et al. (2004), a bright-end slope $\beta \simeq -3.31$, which progressively flattens to become $\beta \simeq -2.5$ at $z > 4$. This result has not been confirmed by Fontanot et al. (2007) who, studying the GOODS sample combined with the SDSS sample, do not find any evidence for a bright-end flattening at redshift $z > 3.5$. They attribute this discrepancy to the template spectra used by the SDSS team to calibrate their selection criteria (see Fontanot et al., 2007, for more details).

A growing number of observations at different redshifts in radio, optical, soft and hard X-ray bands, suggested that also the faint end slope evolves, becoming flatter at high redshift (Page et al., 1997; Miyaji et al., 2000, 2001; La Franca et al., 2002; Cowie et al., 2003; Ueda et al., 2003; Fiore et al., 2003; Hunt et al., 2004; Cirasuolo et al., 2005; Hasinger et al., 2005). This evolution, now dubbed as "AGN cosmic downsizing", is described as "luminosity dependent density evolution" (LDDE), and it has been the subject of many speculations since it implies that the space density of low luminosity AGN peaks at lower

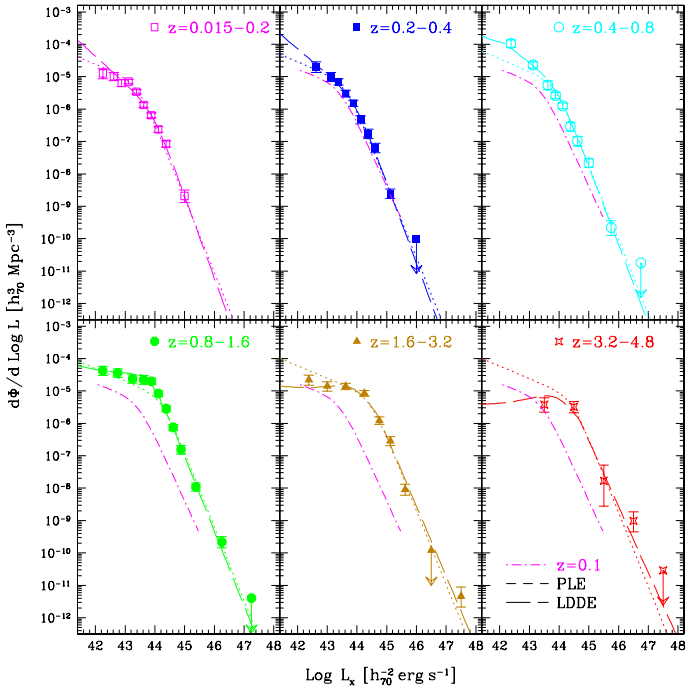

Figure 7.2. The soft X–ray luminosity function of the type–1 AGN sample as derived by Hasinger et al. (2005). The best–fit two power law model for the $0.015 < z < 0.2$ shell are overplotted in the higher redshift panels for reference. The dotted and long-dashed lines give the best–fit PLE and LDDE models.

redshift than in bright ones.

A combined luminosity-density evolution was originally suggested by Schmidt & Green (1983) to describe optically-selected QSOs. They suggested this kind of evolution on the basis of the fact that the $\langle V/V_{max}\rangle$ values, for the *Bright Quasar Survey* (BQS) sample, show a strong dependence on M_B. For the most luminous QSOs, $\langle V/V_{max}\rangle$ is almost 0.8, while for the least luminous ones, it is around 0.5. They assumed that the comoving space density of QSOs was an exponential function of cosmic time, with a coefficient in the exponential depending linearly on M_B, i.e.

$$\Phi(M_B,z) = \Phi(M_b,0)\cdot e^{[k\ (M_0-M_B)\ \tau(z)]} \tag{7.12}$$

where k and M_0 are constants and $\tau(z)$ is the light travel time expressed as a fraction of the age of the Universe. In their model, they assumed k=0 for $M_B > M_0$. This corresponds to no evolution for low luminosity objects.

Following the more recent formulation based on X-ray selected sample (e.g. Hasinger et al., 2005), the LDDE is parameterized as follows:

$$\frac{\mathrm{d}\,\Phi(L_\mathrm{x},z)}{\mathrm{d}\log L_\mathrm{x}} = \frac{\mathrm{d}\,\Phi(L_\mathrm{x},0)}{\mathrm{d}\log L_\mathrm{x}}\cdot e_\mathrm{d}(z,L_\mathrm{x}), \tag{7.13}$$

where $\Phi(L_\mathrm{x},0)$ is the luminosity function at z=0 and $e_\mathrm{d}(z,L_\mathrm{x})$, the evolution function, is expressed as:

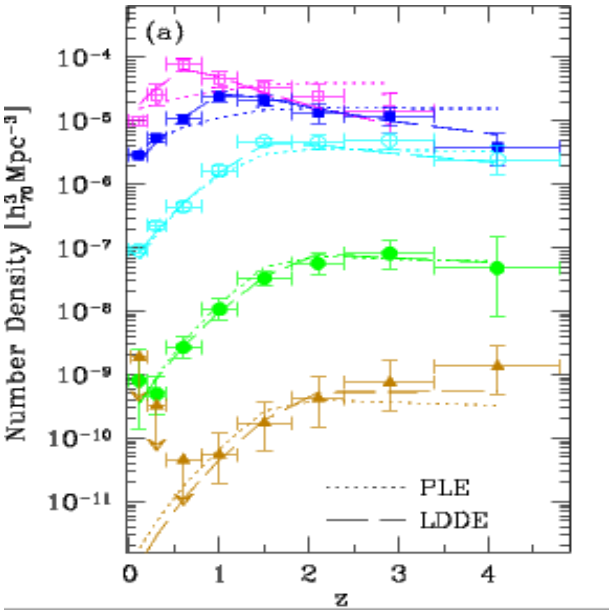

Figure 7.3. Space density of X-ray selected type–1 AGN as a function of redshift in different luminosity classes and the sum over all luminosities with $\log L_{\rm x} \geq 42$ (Hasinger et al., 2005). Densities from the PLE and LDDE models derived by Hasinger et al. (2005) are overplotted with solid lines.

$$e_{\rm d}(z, L_{\rm x}) = \begin{cases} (1+z)^{p1} & (z \leq z_{\rm c}) \\ e_{\rm d}(z_{\rm c})[(1+z)/(1+z_{\rm c})]^{p2} & (z > z_{\rm c}) \end{cases} . \tag{7.14}$$

where $z_{\rm c}$ is a simple function of $L_{\rm x}$:

$$z_{\rm c}(L_{\rm x}) = \begin{cases} z_{\rm c,0}(L_{\rm x}/L_{\rm x,c})^{\alpha} & (L_{\rm x} \leq L_{\rm x,c}) \\ z_{\rm c,0} & (L_{\rm x} > L_{\rm x,c}) \end{cases} . \tag{7.15}$$

Figure 7.2 shows the soft X–ray luminosity function derived by Hasinger et al. (2005) for an X-ray selected sample of type–1 AGN. The best model to fit the evolution of their luminosity function is a LDDE of the form given by 7.14 in which they considered also a dependence of $p1$ and $p2$ on luminosity:

$$p1(L_{\rm x}) = p1_{44} + \beta_1 \, (\log L_{\rm x} - 44) \tag{7.16}$$

$$p2(L_{\rm x}) = p2_{44} + \beta_2 \, (\log L_{\rm x} - 44) \tag{7.17}$$

This evolutionary trend implies an AGN differential evolution depending on the luminosity. As shown in Figure 7.3, more luminous AGN (QSOs) peak earlier in the history of the universe, while the low luminosity ones arise later ("AGN cosmic downsizing").

It has been observed that, in addition to the well known local scale relations between the black hole (BH) masses and the properties of their host galaxies (Kormendy & Richstone, 1995; Magorrian et al., 1998; Ferrarese & Merritt, 2000), also the galaxy

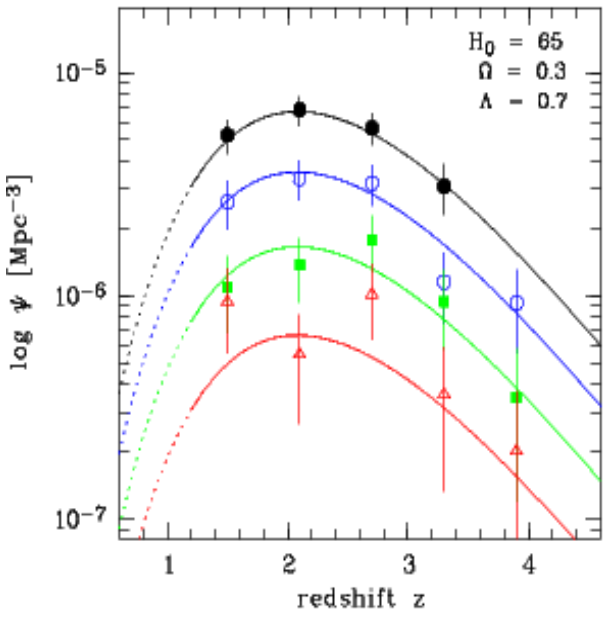

Figure 7.4. Evolution of comoving AGN space density with redshift, for different lower luminosity limits, derived from the COMBO-17 sample by Wolf et al. (2003b). Filled circles: $M_{145} < -24$; open circles: $M_{145} < -25$; filled squares: $M_{145} < -26$; open triangles: $M_{145} < -27$. The corresponding curves are integrated from the best-fit PDE models.

spheroid population follows a similar pattern of "cosmic downsizing" (Cimatti et al., 2006). Various models have been proposed to explain this common evolutionary trend in AGN and spheroid galaxies. The majority of them propose that the feedback from the black hole growth plays a key role in determining the BH-host galaxy relations (Silk & Rees, 1998; Di Matteo et al., 2005) and the co-evolution of black holes and their host galaxies. Indeed, AGN feedback can shut down the growth of the most massive systems steepening the bright end slope (Scannapieco & Oh, 2004), while the feedback-driven quasar decay determines the shape of the faint end QSOs LF (Hopkins et al., 2006b).

This evolutionary trend has not been clearly seen yet with optically selected AGN samples. By combining results from low and high redshifts, it is clear from the studies of optically selected samples that the cosmic QSO evolution shows a strong increase of the activity from $z \sim 0$ out to $z \sim 2$, reaches a maximum around $z \simeq 2-3$ and then declines, but the shape of the turnover and the redshift evolution of the peak in activity as a function of luminosity is still unclear.

As described in Section 3.1, most of the optically selected AGN samples studied so far are obtained through various color (e.g. UV-excess) selections of candidates, followed by spectroscopic confirmation, or grism and slitless spectroscopic surveys. These samples are expected to be highly complete, at least for luminous AGN, at either $z \leq 2.2$ or $z \geq 3.6$, where AGN show conspicuous colors in broad band color searches, but less complete in the redshift range $2.2 \leq z \leq 3.6$ (Richards et al. 2002).

An improvement in the multi-color selection in optical bands is through the simultaneous

use of many broad and medium band filters as, for example, in the COMBO-17 survey (Wolf et al., 2003b). Such a survey is the only optical survey so far which, in addition to covering a redshift range large enough to see the peak of AGN activity ($1.2 < z < 4.8$), is also deep enough to sample up to high redshift AGN with luminosity below the break in the luminosity function. However, only photometric redshifts are available for this sample and, because of their selection criteria, it is incomplete for objects with a small ratio between the nuclear flux and the total host galaxy flux and for AGN with anomalous colors, such as, for example, the Broad Absorption Line (BAL) QSOs , which have on average redder colors and account for ($\sim 10 \div 15$) % of the overall AGN population. The evolution of comoving AGN space density with redshift, for different lower luminosity limits, derived from this sample by Wolf et al. (2003b) is shown in Figure 7.4. From this Figure, no indication for a difference between the space density peaks of AGN of different luminosities is visible.

In this context, the VVDS AGN sample gives the opportunity to study the type–1 AGN activity peak and to observe whether at low luminosity, optically selected AGN follow the trend seen in X-ray surveys.

Chapter 8

The VVDS type–1 AGN luminosity function

In this Chapter I will present the luminosity function derived for the VVDS type–1 AGN sample described in Chapter 5.

8.1 Definition of the redshift range

For the study of the LF we decided to exclude AGN with $z \leq 1.0$. This choice is due to the fact that, given the VVDS observed wavelength range (5500 – 9500 $\AA$), for $0.5 \leq z \leq 1.0$ the only visible broad line is Hβ (see Figure 5.2). This means that all objects with narrow or almost narrow Hβ and broad Hα (type 1.8, 1.9 AGN; Osterbrock 1981; see Section 2.4) would not be included in our sample, because we include in the AGN sample all the objects with at least one visible broad line. Since at low luminosities the number of intermediate type AGN is not negligible, this redshift bin is likely to be under-populated and the results would not be meaningful. In principle, at $z < 0.5$ we have less problems, because also Hα is within the wavelength range of the VVDS spectra, but only 3 objects have secure redshifts in this redshift bin in the current sample. For these reasons, our luminosity function has been computed only for $z > 1.0$ AGN. The small fraction of objects with an ambiguous redshift determination (see Section 5.2.1) have been included in the computation of the luminosity function assuming that our best estimate of their redshift is correct.

8.2 The K-correction

The estimate of the rest frame luminosities for sources at cosmological distances requires knowledge about the intrinsic spectral shape of each source. In optical astronomy, this knowledge is usually represented by a function K(z) (Oke & Sandage, 1968) which gives the redshift dependence of the magnitude of any objects in a given wavelength band:

$$m_{intrinsic} = m_{observed} - K(z) \tag{8.1}$$

The K-correction consists of two terms and it is is formally defined as:

$$K(z) = 2.5\log(1+z) + 2.5\log\left[\frac{\int_0^\infty F(\lambda)S(\lambda)d\lambda}{\int_0^\infty F\left(\frac{\lambda}{1+z}\right)S(\lambda)d\lambda}\right] \tag{8.2}$$

where $F(\lambda)$ is the SED of the object observed (galaxy or QSO) and $S(\lambda)$ is the filter response function. The first term in the K-correction is due to the narrower width of the filter in the observer's frame[1]. The integrals in the second term of the K-correction, are the convolution of the spectrum with the filter response in the observer's frame, normalized by the value at rest. If we consider a simple AGN power law $f_\nu \propto \nu^{-\alpha}$ or, expressed in λ, $f_\lambda \propto \lambda^{\alpha-2}$, the K-correction will be:

$$K(z) = 2.5(\alpha-1)\log(1+z) \tag{8.3}$$

and it vanishes for $\alpha = 1$. However, QSO SED is more complex than a simple power-law. The K-correction is a complicated function of z, since it depends on the fact that emission lines are shifted into the filter. Nominal K-correction are computed by convolving a typical AGN spectrum at different redshifts with the filter response.

8.3 Estimate of the absolute magnitude

We derived the absolute magnitude in the reference band from the apparent magnitude in the observed band as:

$$M = m_{obs} - 5log_{10}(dl(z)) - 25 - K(z) \tag{8.4}$$

where M is computed in the band in which we want to compute the luminosity function, m_{obs} is the observed band from which we want to calculate it, dl(z) is the luminosity distance expressed in Mpc and K(z) is the K-correction in the reference band as defined in Section 8.2. To make easier the comparison with previous results in the literature, we computed the luminosity function in the B-band.

To minimize the uncertainties in the adopted K-correction, m_{obs} for each object should be chosen in the observed band which is sampling the rest-wavelength closer to the band in which the luminosity function is computed. For our sample, which consists only of $z > 1$ objects, the observed band used to compute the B-band absolute magnitude is thus always the I-band.

As discussed in Section 5.6, the VVDS AGN sample shows redder colors than those typical of normal, more luminous AGN and this can be due to the combination of the host galaxy contribution and the presence of dust. Since, in this redshift range, the fractional contribution from the host galaxies is expected to be more significant in the I-band than in

[1] a spectral region of width $\delta\lambda_0$ is stretched to width $\delta\lambda_0(1+z)$ in the observer's frame, which is equivalent to apparent contraction of the observer's filter by the same factor

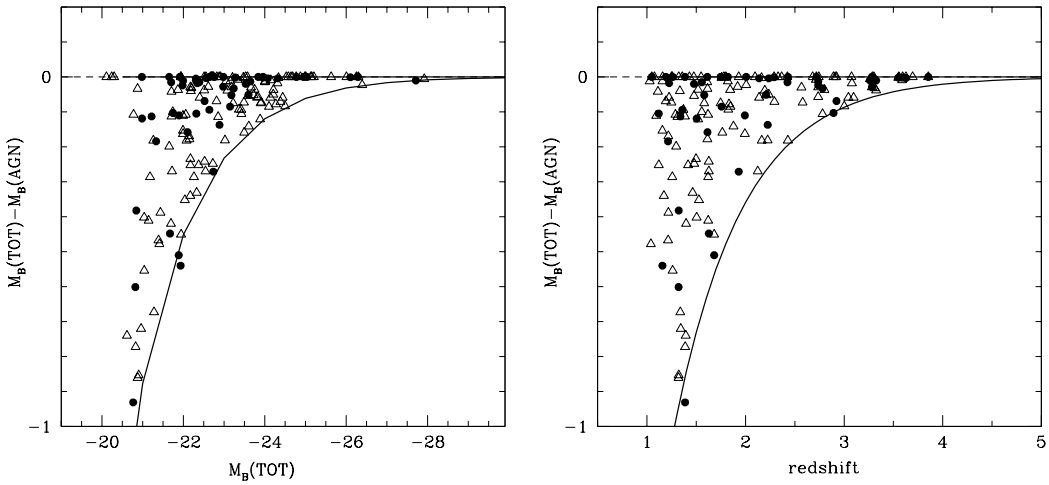

Figure 8.1. Real (solid circles; AGN in the deep sample) and simulated (open triangles; AGN in the wide sample) B-band absolute magnitude differences as a function of M_B(TOT) (left panel) and redshift (right panel). M_B(TOT) is the absolute magnitude computed considering the total observed flux, while M_B(AGN) is the absolute magnitude computed after subtracting the host-galaxy contribution.

bluer bands, the luminosity derived using the I-band observed magnitude could, in some cases, be somewhat overestimated due to the contribution of the host galaxy component.

We estimated the possible impact of this effect on our results in the following way. From the results of the analysis of the SED performed on single objects in the deep sample (see Section 5.6.1) we computed for each of them the difference $m_I(TOT) - m_I(AGN)$ and, consequently, $M_B(TOT) - M_B(AGN)$. These differences are shown as solid circles in Figure 8.1 as a function of absolute magnitude (left panel) and redshift (right panel). For most of the objects the resulting differences between the total and the AGN magnitudes are small ($\Delta M \leq 0.2$). However, for a not negligible fraction of the faintest objects ($M_B \geq$-22.5, $z \leq 2.0$) these differences can be significant (up to $\sim$1 mag). For the wide sample, for which the more restricted photometric coverage did not allow a detailed SED analysis and decomposition, we used simulated differences. These simulated differences have been derived through a Montecarlo simulation on the basis of the bivariate distribution $\Delta M(M,z)$ estimated from the objects in the deep sample. The resulting simulated differences for the objects in the wide sample are shown as open triangles in both panels in Figure 8.1.

The AGN magnitudes and the limiting magnitudes of the samples have been corrected also for galactic extinction on the basis of the mean extinction values $E(B-V)$ in each field derived from Schlegel et al. (1998). Only for the 22h field, where the extinction is highly variable across the field, we used the extinction on the basis of the position of individual objects. The resulting corrections in the I-band magnitude are $A_I \simeq 0.027$ in the 2h and 10h fields and $A_I = 0.0089$ in the CDFS field, while the average value in the 22h

field is $A_I = 0.065$. These corrections have been applied also to the limiting magnitude of each field.

8.4 Computation of the luminosity function: the $1/V_{max}$ estimator

We compute the luminosity function for the whole sample of AGN in all the VVDS fields. Our sample consists of objects found in 4 fields, with two different limiting magnitudes, I_{AB}=24.0 for the deep samples (02h field and CDFS) and I_{AB}=22.5 for the wide samples (10h and 22h fields). As in the computation of the number counts, we combined the four samples using the method proposed by Avni & Bahcall (1980): *"Coherent Analysis of Independent Samples"*. This means that, for our total sample, we consider an area of:

$$\mathcal{A}_{tot}(m) = \mathcal{A}_{deep} + \mathcal{A}_{wide} = 1.72 \text{ deg}^2 \qquad \text{for} \quad 17.5 < I_{AB} < 22.5$$

and

$$\mathcal{A}_{tot}(m) = \mathcal{A}_{deep} = 0.62 \text{ deg}^2 \qquad \text{for} \quad 22.5 < I_{AB} < 24.0$$

We derived the binned representation of the luminosity function using the usual $1/V_{max}$ estimator (Schmidt, 1968), which gives the space density contribution of individual objects. The luminosity function, for each redshift bin $(z - \Delta z/2 \; ; \; z + \Delta z/2)$, is then computed as:

$$\Phi(M) = \frac{1}{\Delta M} \sum_{M-\Delta M/2}^{M+\Delta M/2} \frac{w_i^{tsr} w_i^{ssr}}{V_{max,i}} \tag{8.5}$$

where $V_{max,i}$ is the comoving volume within which the i^{th} object would still be included in the sample. w_i^{tsr} and w_i^{ssr} are respectively the inverse of the TSR and of the SSR (as defined in Section 6.1), associated to the i^{th} object. The statistical uncertainty on Φ(M) is given by (Marshall et al., 1983):

$$\sigma_\phi = \frac{1}{\Delta M} \sqrt{\sum_{M-\Delta M/2}^{M+\Delta M/2} \frac{(w_i^{tsr} w_i^{ssr})^2}{V_{max,i}^2}} \tag{8.6}$$

The resulting luminosity functions in different redshift ranges are plotted in Figure 8.2 and 8.3, where all bins which contain at least one object are plotted. In Figure 8.2 we assume a cosmology with Ω_m = 0.3, Ω_Λ = 0.7 and H_0 = 70 km s^{-1} Mpc^{-1}, while in Figure 8.3 we assume a different cosmology ($\Omega_m = 1$, $\Omega_\Lambda = 0$ and H_0 = 50 km s^{-1} Mpc^{-1}) for comparison with previous works. The LF values, together with their 1σ errors and the numbers of objects in each absolute magnitude bin are presented in Table 8.1.

Even if the differences between the total absolute magnitudes and the magnitudes corrected for the host galaxy contribution (see Section 4.4) can be significant for a fraction of the faintest objects, we have a posteriori verified that the resulting luminosity functions

computed by using these two sets of absolute magnitudes are not significantly different. For this reason and for a more direct comparison with previous works, the results on the luminosity function presented in the next Section are those obtained using the total magnitudes.

8.5 Comparison with the results from other optical surveys

We derived the luminosity function up to $z = 3.6$ and we compared it with the results from other surveys at both low and high redshift.

8.5.1 The low redshift luminosity function

In Figure 8.2 we present our luminosity function up to $z = 2.1$. Both panels show our LF data points (solid circles) derived in two redshift bins: $1.0 < z < 1.55$ and $1.55 < z < 2.1$. The upper panel shows the comparison with the LF fits derived from the 2dF QSO sample by Croom et al. (2004) and by Boyle et al. (2000), and from the COMBO-17 sample by Wolf et al. (2003b), while the bottom panel shows our data points compared with the 2dF-SDSS (2SLAQ) LF fit by Richards et al. (2005). In each panel the curves, computed for the average z of the redshift range, correspond to a double power law luminosity function in which the evolution with redshift is characterized by a pure luminosity evolution modeled as $M^*_b(z) = M^*_b(0) - 2.5(k_1 z + k_2 z^2)$ (see Equation 7.11(c)). Moreover, the thick parts of the curves show the luminosity range covered by the data in each of the comparison samples, while the thin parts are extrapolations based on the the best fit parameters of the models.

We start considering the comparison with the 2dF and the COMBO-17 LF fits. As shown in Figure 8.2, our bright LF data points connect rather smoothly to the faint part of the 2dF data. However, our sample is more than two magnitudes deeper than the 2dF sample. For this reason, a comparison at low luminosity is possible only with the extrapolations of the LF fit. At $z > 1.55$, while the Boyle's model fits well our faint LF data points, the Croom's extrapolation, being very flat, tends to underestimate our low luminosity data points. At $z < 1.55$ the comparison is worse: as in the higher redshift bin, the Boyle's model fits our data better than the Croom's one but, in this redshift bin, our data points show an excess at low luminosity also with respect to Boyle's fit. This trend is similar to what is shown also by the comparison with the fit of the COMBO-17 data which, differently from the 2dF data, have a low luminosity limit closer to ours: at $z > 1.55$ the agreement is very good, but in the first redshift bin our data show again an excess at low luminosity. This excess is likely due to the fact that, because of its selection criteria, the COMBO-17 sample is expected to be significantly incomplete for objects in which the ratio between the nuclear flux and the total host galaxy flux is small.

In the bottom panel, we compare our data with the 2SLAQ fits derived by Richards et al.

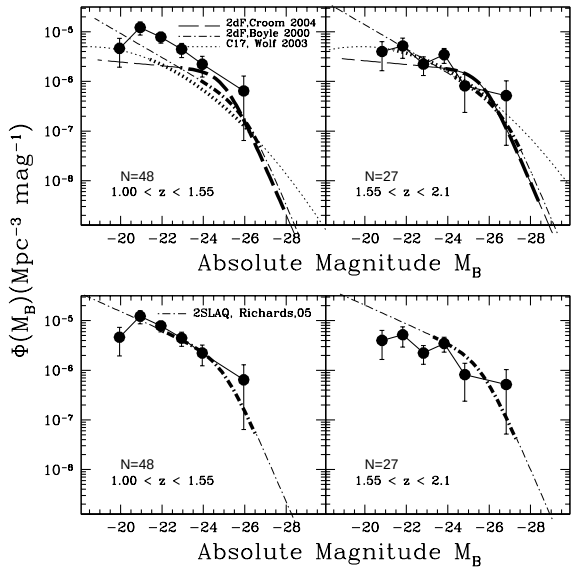

Figure 8.2. Our rest-frame B-band luminosity function, derived in the redshift bins $1.0 < z < 1.55$ and $1.55 < z < 2.1$, compared with the 2dFQRS (Croom et al., 2004; Boyle et al., 2000) and COMBO-17 data (Wolf et al., 2003b) in the upper panel and with the 2dF-SDSS (2SLAQ) data (Richards et al., 2005) in the lower panel. The curves in the Figure show the PLE fit models derived by these authors. The thick parts of the curves correspond to the luminosity range covered by the data in each sample, while the thin parts are extrapolations based on the best fit parameters of the models.

(2005). The 2SLAQ data are derived from a sample of AGN selected from the SDSS, at $18.0 < g < 21.85$ and $z < 3$, and observed with the 2-degree field instrument. Similarly to the 2dF sample, also for this sample the LF is derived only for $z < 2.1$ and $M_B < -22.5$. The plotted dot-dashed curve corresponds to a PLE model in which they fixed most of the parameters of the model at the values found by Croom et al. (2004), leaving to vary only the faint end slope and the normalization constant Φ^*. In this case, the agreement with our data points at $z < 1.55$ is very good also at low luminosity. The faint end slope found in this case is $\beta = -1.45$, which is similar to that found by Boyle et al. (2000) ($\beta = -1.58$) and significantly steeper than that found by Croom et al. (2004) ($\beta = -1.09$). At $z > 1.55$, the Richards et al. (2005) LF fit tends to overestimate our data points at the faint end of the LF, which suggest a flatter slope in this redshift bin.

The first conclusion from this comparison is that, at low redshift (i.e. $z < 2.1$), the data from our sample, which is $\sim$2 mag fainter than the previous spectroscopically confirmed samples, are not well fitted simultaneously in the two analyzed redshift bins by the PLE models derived from the previous samples. Qualitatively, the main reason for this appears to be due to the fact that our data suggest a change in the faint end slope of the LF, which appears to flatten with increasing redshift. This trend, as already said in Section 7.2, has been highlighted by previous X-ray surveys (La Franca et al., 2002; Ueda et al., 2003; Fiore et al., 2003) and it suggests that a simple PLE parameterization may not be

a good representation of the evolution of the AGN luminosity function over a wide range of redshift and luminosity. Different model fits will be discussed in Section 8.7.

8.5.2 The high redshift luminosity function

The comparison of our LF data points for 2.1<z<3.6 (solid circles) with the results from other samples in similar redshift ranges is shown in Figure 8.3. In this Figure an $\Omega_m = 1$, $\Omega_\Lambda = 0$, $h = 0.5$ cosmology has been assumed for comparison with previous works, and the absolute magnitude has been computed at 1450Å. As before, the thick parts of the curves show the luminosity ranges covered by the various data samples, while the thin parts are model extrapolations. In terms of number of objects, depth and covered area, the only sample comparable to ours is the COMBO-17 sample (Wolf et al., 2003b), which, in this redshift range, consists of 60 AGN candidates over 0.78 square degree. At a similar depth, in terms of absolute magnitude, we show also the data from the sample of Hunt et al. (2004), which however consists of 11 AGN in the redshift range ($\langle z \rangle \pm \sigma_z$) = (3.03±0.35) (Steidel et al., 2002). Given the small number of objects, the corresponding Hunt model fit was derived including also the Warren data points. Moreover, they assumed the Pei (1995) luminosity evolution model, adopting the same values for L^* and Φ^*, leaving free to vary the two slopes, both at the faint and at the bright end of the LF. For comparison we show also the original Pei model fit derived from the empirical luminosity function estimated by Hartwick & Schade (1990) and Warren et al. (1994).

In general, the comparison of the VVDS data points with those from other surveys shown in Figure 8.3 shows a satisfactory agreement in the region of overlapping magnitudes. It is interesting to note that, in the faint part of the LF, our data points appear to be higher with respect to the Hunt et al. (2004) fit and are instead closer to the extrapolation of the original Pei model fit. This difference with the Hunt et al. (2004) fit is probably due to the fact that, having only 11 AGN in their faint sample, their best fit to the faint-end slope was poorly constrained.

8.6 The bolometric luminosity function

The comparison between the AGN LFs derived from samples selected in different bands has been for a long time a critical point in the studies of the AGN luminosity function. The crucial points in the LFs transformation between two different bands are essentially two:

- this procedure requires an accurate knowledge of the whole QSO spectral energy distribution in order to convert the luminosities between two different wavebands;
- it requires an accurate knowledge of the AGN absorption properties to rescale and correct the LF for the extinction in the different observed bands.

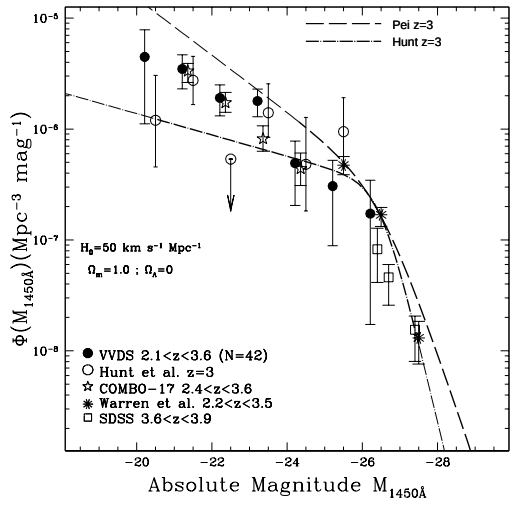

Figure 8.3. Our luminosity function, at 1450Å rest-frame, in the redshift range 2.1<z<3.6, compared with data from other high-z samples (Hunt et al. (2004) at $z = 3$; Combo-17 data from Wolf et al. (2003b) at $2.4 < z < 3.6$; data from Warren et al. (1994) at $2.2 < z < 3.5$ and the SDSS data from Fan et al. (2001)). The SDSS data points at $3.6 < z < 3.9$ have been evolved to z=3 using the luminosity evolution of Pei (1995) as in Hunt et al. (2004). The two curves show some model fits in which the thick parts of the curves correspond to the luminosity range covered by the data samples, while the thin parts are model extrapolation. For this plot, an $\Omega_m = 1$, $\Omega_\Lambda = 0$, $h = 0.5$ cosmology has been assumed for comparison with the previous works.

Recently, Hopkins et al. (2007), combining a large number of LF measurements obtained in different redshift ranges, observed wavelength bands and luminosity intervals, derived the Bolometric Quasar Luminosity Function in the redshift range z = 0 - 6.

For each observational band, they derived appropriate bolometric corrections, taking into account the variation with luminosity of both the average absorption properties (e.g. the quasar column density N_H from X-ray data) and the average global spectral energy distributions. They show that, with these bolometric corrections, it is possible to find a good agreement between results from all different sets of data.

The bolometric corrections (with zero attenuation) derived by Hopkins et al. (2007), by constructing a model of an "intrinsic" (un-reddened) QSOs SED, can be accurately approximated as a double power-law:

$$\frac{L}{L_{\rm band}} = c_1 \left(\frac{L}{10^{10} L_\odot}\right)^{k_1} + c_2 \left(\frac{L}{10^{10} L_\odot}\right)^{k_2}, \tag{8.7}$$

with (c_1, k_1, c_2, k_2) are given by (6.25, -0.37, 9.00, -0.012) for $L_{\rm band} = L_B$, (7.40, -0.37, 10.66, -0.014) for $L_{15\mu{\rm m}}$, (17.87, 0.28, 10.03, -0.020) for $L_{0.5-2\,{\rm keV}}$, and (10.83, 0.28, 6.08, -0.020) for $L_{2-10\,{\rm keV}}$. Figure 8.4 shows these corrections as a function of luminosity.

As already mentioned, in order to convert the observed luminosity function to a bolometric luminosity function, it is necessary to correct for the extinction in the different observed bands. Essentially, the probability of observing a quasar of a given bolometric luminosity at some observed luminosity in a given band must account for the probability

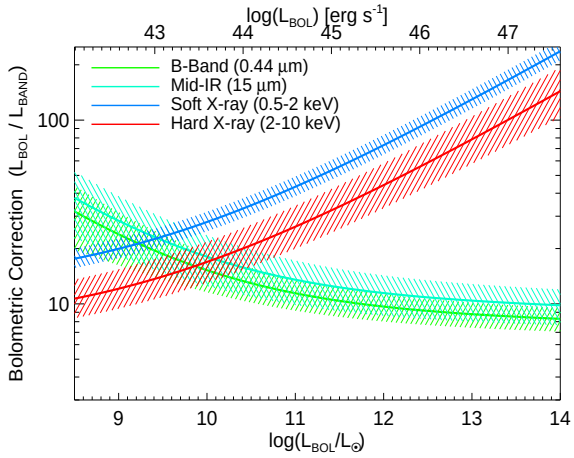

Figure 8.4. Bolometric corrections for *B*-band, mid-IR, soft and hard X-ray bands, determined by Hopkins et al. (2007) from a number of observations, as a function of luminosity and given by the fitting formulae in Equation (8.7).

of extinction or attenuation. The column density distribution, derived by Hopkins et al. (2007), in which an "obscured fraction" as a function of luminosity was adopted, has been parameterized as a power law:

$$f(L) \equiv \frac{\phi(L_i)}{\phi(L[L_i])} = f_{46}\left(\frac{L[L_i]}{10^{46}\,\mathrm{erg\,s^{-1}}}\right)^{\beta} \frac{d\log(L[L_i])}{d\log(L_i)}\,, \tag{8.8}$$

where L_i is the luminosity in some bands, and L is the corresponding bolometric luminosity given by the bolometric corrections of Equation (8.7). This gives values (f_{46}, β) of $(0.260, 0.082)$ for $L_i = L_B$ (4400 Å), $(0.438, 0.068)$ for $L_i = L_{IR}$ ($15\,\mu$m), $(0.609, 0.063)$ for $L_i = L_{SX}$ ($0.5-2$ keV), and $(1.243, 0.066)$ for $L_i = L_{HX}$ ($2-10$ keV).

We derived the bolometric LF for our sample by applying to our LF data points the bolometric corrections given by Eqs. 8.7 and 8.8 for the B-band. The VVDS type–1 AGN Bolometric LF is shown as black dots in Figure 8.5. The solid line represents the bolometric LF best fit model derived by Hopkins et al. (2007) and the colored data points correspond to different samples: green points are from optical LFs, blue and red points are from soft-X and hard-X LFs, respectively, and finally the cyan points are from the mid-IR LFs. All these bolometric LFs data points have been derived following the same procedure described in Hopkins et al. (2007).

Our data, which sample the faint part of the bolometric luminosity function better than all previous optically selected samples, are in good agreement with all the other samples, selected in different bands, and thus also with the model fit derived by Hopkins et al. (2007). By trying various analytic fits to the bolometric luminosity function, Hopkins et al. (2007) concluded that neither pure luminosity nor pure density evolution represent well all the data. An improved fit can instead be obtained with a luminosity dependent density evolution model (LDDE) or, even better, with a PLE model in which both the

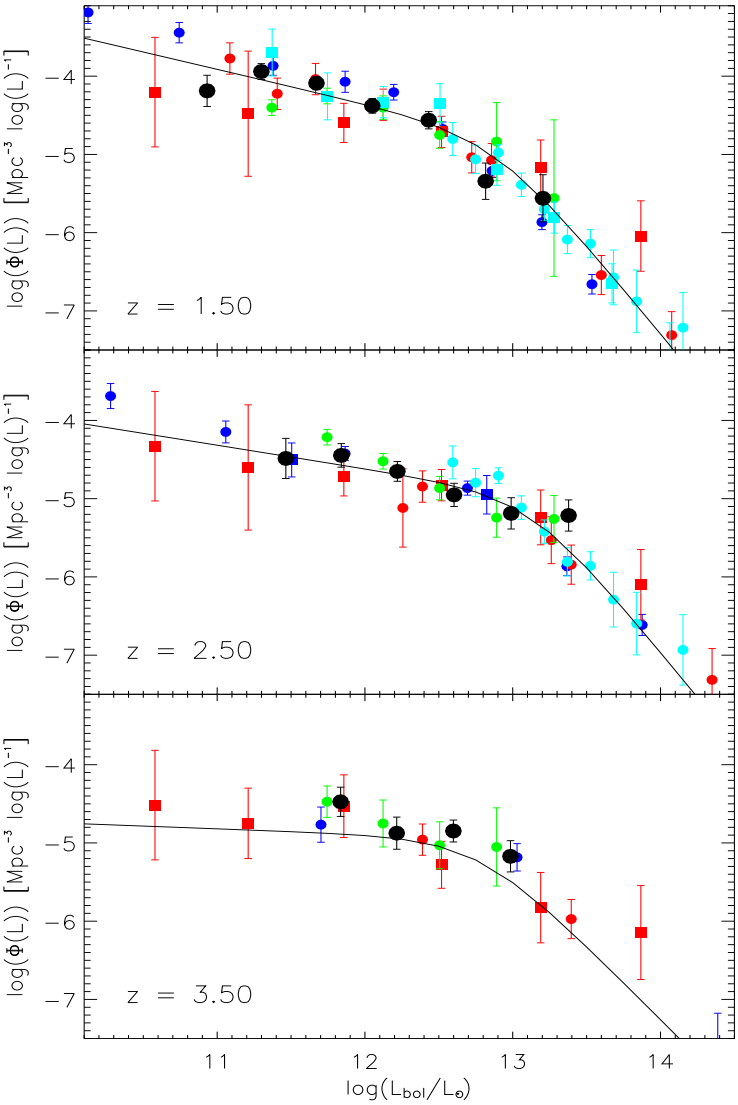

Figure 8.5. Bolometric luminosity function derived in three redshift bins from our data (black dots), compared with Hopkins et al. (2007) best-fit model and the data-sets used in their work. The central redshift of each bin is indicated in each panel. Here, we adopted the same color-code as in Hopkins et al. (2007), but for more clarity we limited the number of samples presented in the Figure. Red symbols correspond to hard X-ray surveys (squares: Barger et al. 2005; circles: Ueda et al. 2003). Blue to soft X-ray surveys (squares: Silverman et al. 2005; circles: Hasinger et al. 2005). Cyan to infra-red surveys (circles: Brown et al. 2006; squares: Matute et al. 2006). For the optical surveys weshow here, with green circles, the data from the COMBO-17 survey (Wolf et al., 2003b), which is comparable in depth to our sample.

bright- and the faint-end slopes evolve with redshift. Both these models can reproduce the observed flattening with redshift of the faint end of the luminosity function.

8.7 Model fitting

In this Section we discuss the results of a number of different fits to our data as a function of luminosity and redshift. Since our data cover only the faint part of the luminosity function at redshift $1.0 < z < 4.0$ (see Section 8.1), these fits have been performed by combining our data with the LF data points from the SDSS data release 3 (DR3) (Richards et al., 2006b) in the redshift range $0 < z < 4$. The advantage of using the SDSS sample, rather than, for example, the 2dF sample, is that this sample, because of the way it is selected, probes the luminosity function to much higher redshifts. The SDSS sample contains more than 15,000 spectroscopically confirmed AGN selected from an effective area of 1622 sq.deg. Its limiting magnitude (i $<$ 19.1 for z $<$ 3.0 and i $<$ 20.2 for z $>$ 3.0) is much brighter than the VVDS and because of this it does not sample well the AGN in the faint part of the luminosity function. For this reason, Richards et al. (2006b) fitted the SDSS data using only a single power law, which is meant to describe the luminosity function above the break luminosity. Adding the VVDS data, which instead mainly sample the faint end of the luminosity function, and analyzing the two samples together, allows us to cover the entire luminosity range in the common redshift range (1.0 $< z <$ 4.0), also extending the analysis at z $<$ 1.0 where only SDSS data are available.

The goodness of fit between the computed LF data points and the various models is then determined by the χ^2 test.

For all the analyzed models we have parameterized the luminosity function as a double power law expressed in absolute magnitude as in Equation 7.7

$$\Phi(M,z) = \frac{\Phi^*_M}{10^{0.4(\alpha+1)(M-M^*)} + 10^{0.4(\beta+1)(M-M^*)}} \tag{8.9}$$

8.7.1 The PLE and PDE models

The first model that we tested is a Pure Luminosity Evolution (PLE) with the dependence of the characteristic luminosity described by a 2nd-order polynomial in redshift (7.11(c)):

$$M^*(z) = M^*(0) - 2.5(k_1 z + k_2 z^2). \tag{8.10}$$

Following the model found by Richards et al. (2006b) for the SDSS sample, we have allowed a change (flattening with redshift) of the bright end slope according to a linear evolution in redshift: $\alpha(z) = \alpha(0) + A\ z$. The resulting best fit parameters are listed in the second line of Table 8.2 and the resulting model fit is shown as a green short dashed

line in Figure 8.6. The bright end slope α derived by our fit (α_{VVDS}=-3.19 at z=2.45) is consistent with the one found by Richards et al. (2006b) (α_{SDSS} = -3.1). [2]

As shown in Figure 8.6, while this model reproduces well the bright part of the LF in the entire redshift range, does not fit the faint part of the LF at low redshift ($1.0 < z < 1.5$). This appears to be due to the fact that, given the overall best fit normalization, the derived faint end slope (β =-1.38) is too shallow to reproduce the VVDS data in this redshift range.

Richards et al. (2005), working on a combined 2dF-SDSS (2SLAQ) sample of AGN up to $z = 2.1$ found that, fixing all the parameters except β and the normalization, to those of Croom et al. (2004), the resulting faint end slope is $\beta = -1.45 \pm 0.03$. This value would describe better our faint LF at low redshift. This trend suggests a kind of combined luminosity and density evolution not taken into account by the used model. For this reason, we attempted to fit the data also including a term of density evolution in the form of:

$$\Phi^*_M(z) = \Phi^*_M(0) \cdot 10^{k_{1D}z + k_{2D}z^2} \tag{8.11}$$

In this model the evolution of the LF is described by both a term of luminosity evolution, which affects M^*, and a term of density evolution, which allows for a change in the global normalization Φ^*. The derived best fit parameters of this model are listed in the third line of Table 8.2 and the model fit is shown as a blue long dashed line in Figure 8.6. This model gives a better χ^2 with respect to the previous model, describing the entire sample better than a simple PLE (the reduced χ^2 decreases from $\sim$ 1.9 to $\sim$ 1.35). However, it still does not satisfactorily reproduce the excess of faint objects in the redshift bin $1.0 < z < 1.5$ and, moreover, it underestimates the faint end of the LF in the last redshift bin ($3.0 < z < 4.0$).

8.7.2 The LDDE model

Recently, a growing number of observations at different redshifts, in soft and hard X-ray bands, have found evidences of flattening of the faint end slope of the LF towards high redshift. This trend has been described through a luminosity-dependent density evolution parameterization. Such a parameterization allows the redshift of the AGN density peak to change as a function of luminosity. This could help in explaining the excess of faint AGN found in the VVDS sample at $1.0 < z < 1.5$. Therefore, we considered a luminosity dependent density evolution model (LDDE), as computed in the major X-surveys (Miyaji et al. 2000; Ueda et al. 2003; Hasinger et al. 2005). In particular, following Hasinger et al. (2005), we assumed an LDDE evolution of the form:

$$\Phi(M_{\rm B}, z) = \Phi(M, 0) * e_{\rm d}(z, M_{\rm B}) \tag{8.12}$$

[2] in their parameterization A_1=-0.4$(\alpha + 1)$ =0.84

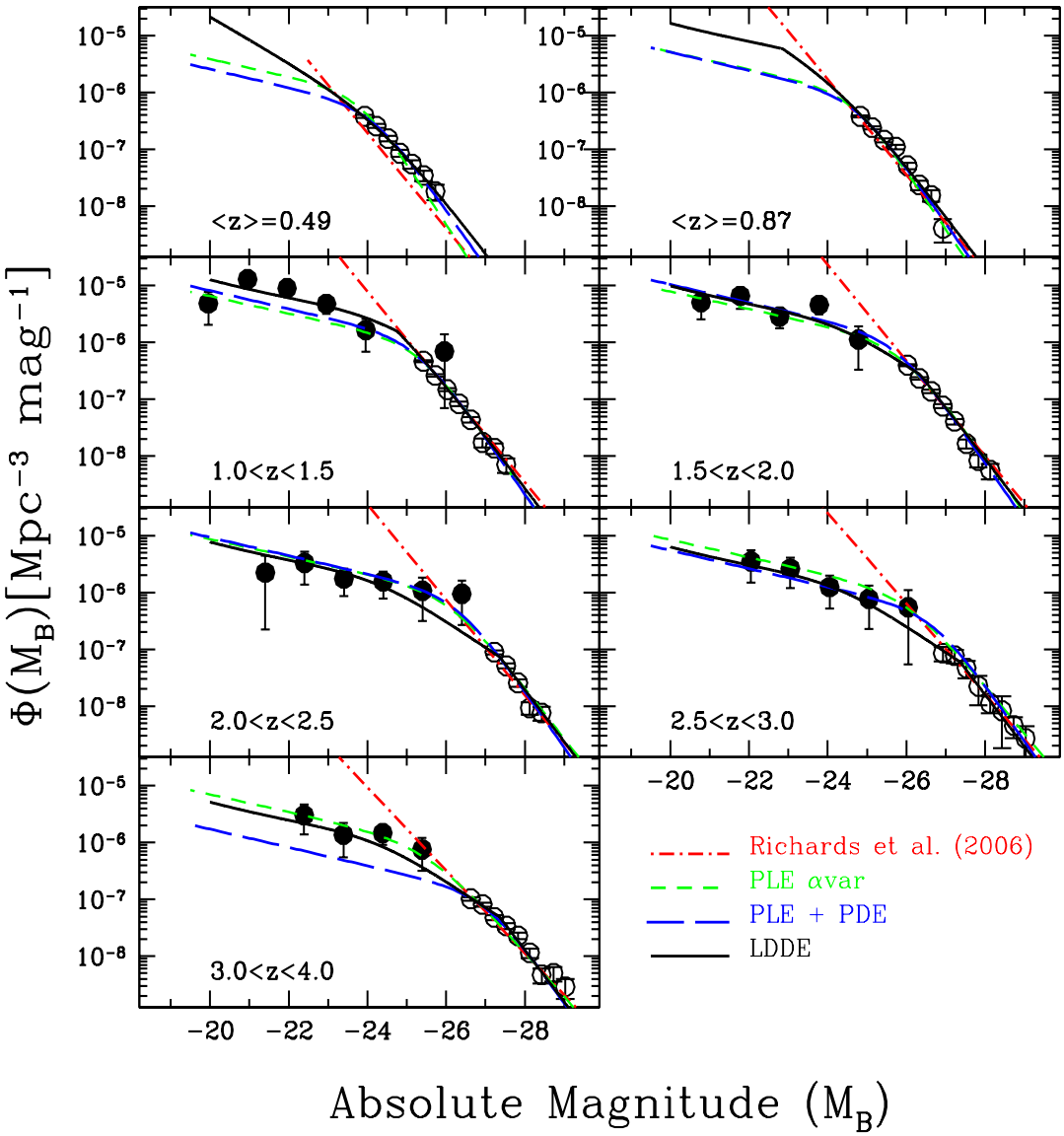

Figure 8.6. Filled circles correspond to our rest-frame B-band luminosity function data points, derived in the redshift bins $1.0 < z < 1.5$, $1.5 < z < 2.0$, $2.0 < z < 2.5$, $2.5 < z < 3.0$ and $3.0 < z < 4.0$. Open circles are the data points from the SDSS Data Release 3 (DR3) by Richards et al. (2006b). These data are shown also in two redshift bins below z = 1. The red dot-dashed line corresponds to the model fit derived by Richards et al. (2006b) only for the SDSS data. The other lines correspond to model fits derived considering the combination of the VVDS and SDSS samples for different evolutionary models, as listed in Table 8.2 and described in Section 8.7.

where:

$$e_{\rm d}(z, M_{\rm B}) = \begin{cases} (1+z)^{p1} & (z \leq z_{\rm c}) \\ e_{\rm d}(z_{\rm c})[(1+z)/(1+z_{\rm c})]^{p2} & (z > z_{\rm c}) \end{cases} . \quad (8.13)$$

along with

$$z_{\rm c}(M_{\rm B}) = \begin{cases} z_{\rm c,0} 10^{-0.4\gamma(M_{\rm B}-M_{\rm c})} & (M_{\rm B} \geq M_{\rm c}) \\ z_{\rm c,0} & (M_{\rm B} < M_{\rm c}) \end{cases} . \quad (8.14)$$

where z_c corresponds to the redshift at which the evolution changes. Note that z_c is not constant but it depends on the luminosity. This dependence allows different evolutions at different luminosities and can indeed reproduce the differential AGN evolution as a function of luminosity, thus modifying the shape of the luminosity function as a function of redshift. We also considered two different assumptions for p1 and p2: (i) both parameters constant and (ii) both linearly depending on luminosity as follows:

$$p1(M_{\rm B}) = p1_{M_{\rm ref}} - 0.4\varepsilon_1 \, (M_{\rm B} - M_{\rm ref}) \quad (8.15)$$

$$p2(M_{\rm B}) = p2_{M_{\rm ref}} - 0.4\varepsilon_2 \, (M_{\rm B} - M_{\rm ref}) \quad (8.16)$$

The corresponding χ^2 values for the two above cases are respectively χ^2=64.6 and χ^2=56.8. Given the relatively small improvement of the fit, we considered the addition of the two further parameters (ε_1 and ε_2) unnecessary. The model with constant p1 and p2 values is shown with a solid black line in Figure 8.6 and the best fit parameters derived for this model are reported in the last line of Table 8.2.

This model reproduces well the overall shape of the luminosity function over the entire redshift range, including the excess of faint AGN at $1.0 < z < 1.5$. The χ^2 value for the LDDE model is in fact the best among all the analyzed models and corresponds to a fully acceptable value of the reduced χ^2 of ~ 1. [3]

The best fit value of the faint end slope, which in this model corresponds to the slope at z = 0, is β=-2.0. This value is consistent with that derived by Hao et al. (2005) studying the emission line luminosity function of a sample of Seyfert galaxies at very low redshift ($0 < z < 0.15$), extracted from the SDSS. They in fact derived a slope β ranging from -2.07 to -2.03, depending on the line used to compute the nuclear luminosity. In Figure 8.7 we show the comparison between the Hao et al. (2005) luminosity function (red line), derived for type–1 AGN and parameterized by a single power-law, and our best fit model (black line; LLDE model). The Hao's LF, plotted here as a function of the M_B, has been derived by the Hα line-luminosity function by applying the conversion, given in the Hao et al. (2005) paper, between the Hα luminosity and the r-band PSF absolute magnitude M_r. Hao et al. (2005) found in fact that the relationship between this two variables is very

[3] We note that the reduced χ^2 of our best fit model, which includes also VVDS data, is significantly better than that obtained by Richards et al. (2006b) in fitting only the SDSS DR3 data.

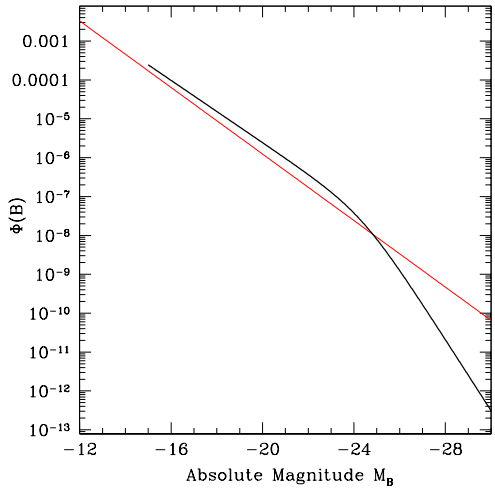

Figure 8.7. Comparison between our LF best-fit model extrapolated at z=0 and the model derived by Hao et al. (2005) for a sample of Seyfert galaxies at very low redshift ($0 < z < 0.15$), extracted from the SDSS.

tight, demonstrating that the Hα luminosities for these quasars are indeed excited by their nuclear luminosities. A linear fit to these data gives:

$$log[L(H_\alpha)/L_\odot] = -(0.419 \pm 0.010)\, M_r - (0.209 \pm 0.30) \tag{8.17}$$

Then, M_r has been converted in B-band absolute magnitudes. Moreover a further correction factor has been applied, both in luminosity and in the normalization, to take into account for the different assumed cosmologies [4].

As shown in Figure 8.7, the comparison between the two slopes is very good; this was expected given the slope values, -2.0 for the VVDS and -2.07 for the Hao's sample. Moreover, also the normalization are in good agreement, confirming our model also in a redshift range where data are not available and indeed leading us to have a good confidence on the extrapolation of the derived model.

8.8 The AGN activity as a function of redshift

By integrating the luminosity function corresponding to our best fit model (i.e the LDDE model; see Table 8.2), we derived the comoving AGN space density as a function of redshift for different luminosity ranges (Figure 8.8).

The existence of a peak at z$\sim$ 2 in the space density of bright AGN is known since a long time, even if rarely it has been possible to precisely locate the position of this maximum within a single optical survey. Figure 8.8 shows that for our best fit model the peak of the AGN space density shifts significantly towards lower redshift going to lower

[4]They assumed a cosmology with Ω_m = 0.3, Ω_Λ = 0.7 and H_0 = 100 km s^{-1} Mpc^{-1} while our LF is derived assuming Ω_m = 0.3, Ω_Λ = 0.7 and H_0 = 70 km s^{-1} Mpc^{-1}

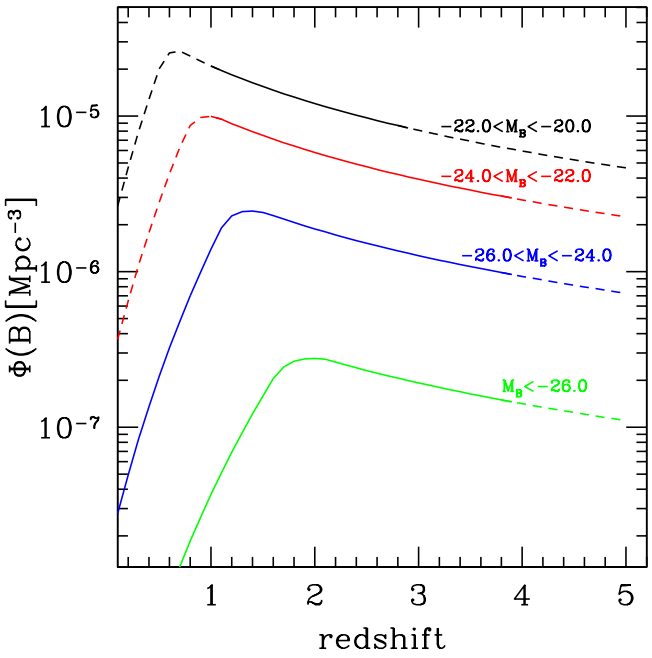

Figure 8.8. Evolution of the comoving AGN space density with redshift, for different luminosity ranges: $-22.0 < M_B < -20.0$; $-24.0 < M_B < -22.0$; $-26.0 < M_B < -24.0$ and $M_B < -26.0$. Dashed lines correspond to the redshift range in which the model has been extrapolated.

luminosity. The position of the maximum moves from z$\sim$ 2.0 for M_B <-26.0 to z$\sim$ 0.65 for -22< M_B <-20.

A similar trend has recently been found by the analysis of several deep X-ray selected samples (Cowie et al., 2003; Hasinger et al., 2005) and it has been interpreted as evidence of AGN (i.e. black hole) "cosmic downsizing", similar to what has recently been observed in the galaxy spheroid population (Cimatti et al., 2006). The downsizing (Cowie et al., 1996) is a term which is used to describe the phenomenon whereby luminous activity (star formation and accretion onto black holes) appears to be occurring predominantly in progressively lower mass objects (galaxies or BHs) as the redshift decreases. As such, it explains why the number of bright sources peaks at higher redshift than the number of faint sources.

As already said, this effect had not been seen so far in the analysis of optically selected samples. This can be due to the fact that most of the optical samples, because of their limiting magnitudes, do not reach luminosities where the difference in the location of the peak becomes evident. The COMBO-17 sample (Wolf et al., 2003b), for example, even if it covers enough redshift range ($1.2 < z < 4.8$) to enclose the peak of the AGN activity, does not probe luminosities faint enough to find a significant indication for a difference between the space density peaks of AGN of different luminosities (see, for example, Figure 7.4, which is analogous to our Figure 8.8, but in which only COMBO-17 AGN, which are brighter than M $\sim$ -24, are shown). The VVDS sample, being about one

magnitude fainter than the COMBO-17 sample and not having any bias in finding faint AGN, allows us to detect for the first time in an optically selected sample the shift of the maximum space density towards lower redshift for low luminosity AGN.

Table 8.1. Binned luminosity function estimate for Ω_m=0.3, Ω_Λ=0.7 and H_0=70 km $\cdot$ s^{-1} $\cdot$ Mpc^{-1}. We list the values of Log Φ and the corresponding 1σ errors in five redshift ranges, as plotted with solid circles in Figure 8.6 and in ΔM_B=1.0 magnitude bins. We also list the number of AGN contributing to the luminosity function estimate in each bin

$1.0 < z < 1.5$						$1.5 < z < 2.0$					
ΔM		N_{qso}	LogΦ(B)	ΔLogΦ(B)		ΔM		N_{qso}	LogΦ(B)	ΔLogΦ(B)	
-19.46	-20.46	3	-5.31	+0.20	-0.38						
-20.46	-21.46	11	-4.89	+0.12	-0.16	-20.28	-21.28	4	-5.29	+0.18	-0.30
-21.46	-22.46	17	-5.04	+0.09	-0.12	-21.28	-22.28	7	-5.18	+0.15	-0.22
-22.46	-23.46	9	-5.32	+0.13	-0.18	-22.28	-23.28	7	-5.54	+0.14	-0.20
-23.46	-24.46	3	-5.78	+0.20	-0.38	-23.28	-24.28	10	-5.34	+0.12	-0.17
-25.46	-26.46	1	-6.16	+0.52	-0.76	-24.28	-25.28	2	-5.94	+0.23	-0.53
$2.0 < z < 2.5$						$2.5 < z < 3.0$					
ΔM		N_{qso}	LogΦ(B)	ΔLogΦ(B)		ΔM		N_{qso}	LogΦ(B)	ΔLogΦ(B)	
-20.90	-21.90	1	-5.65	+0.52	-0.76						
-21.90	-22.90	3	-5.48	+0.20	-0.38	-21.55	-22.55	3	-5.45	+0.20	-0.38
-22.90	-23.90	4	-5.76	+0.18	-0.30	-22.55	-23.55	4	-5.58	+0.19	-0.34
-23.90	-24.90	4	-5.81	+0.18	-0.30	-23.55	-24.55	3	-5.90	+0.20	-0.38
-24.90	-25.90	2	-5.97	+0.23	-0.53	-24.55	-25.55	2	-6.11	+0.23	-0.53
-25.90	-26.90	2	-6.03	+0.23	-0.55	-25.55	-26.55	1	-6.26	+0.52	-0.76
$3.0 < z < 4.0$											
ΔM		N_{qso}	LogΦ(B)	ΔLogΦ(B)							
-21.89	-22.89	4	-5.52	+0.19	-0.34						
-22.89	-23.89	3	-5.86	+0.20	-0.40						
-23.89	-24.89	7	-5.83	+0.14	-0.21						
-24.89	-25.89	3	-6.12	+0.20	-0.38						

Table 8.2. Best fit models derived from the χ^2 analysis of the combined sample VVDS+SDSS-DR3 in the redshift range $0.0 < z < 4.0$ assuming a flat ($\Omega_m + \Omega_\Lambda = 1$) universe with $\Omega_m = 0.3$. For comparison we list also the parameters found by Richards et al. (2005), for the 2dF-SDSS (2SLAQ) sample in the redshift range $0.4 < z < 2.1$, in the same cosmology.

Sample - Evolution Model	α	β	M^*	k_{1L}	k_{2L}	A	k_{1D}	k_{2D}	Φ^*	χ^2	ν
2SLAQ (Rich05)	-3.28	-1.78	-22.68	1.37	-0.32	-	-	-	5.96E-7	-	-
VVDS+SDSS - PLE α var	-3.83	-1.38	-22.51	1.23	-0.26	0.26	-	-	9.78E-7	130.4	69
VVDS+SDSS - PLE+PDE	-3.49	-1.40	-23.40	0.68	-0.073	-	-0.97	-0.31	2.15E-7	91.4	68
Sample - Evolution Model	α	β	M^*	$p1$	$p2$	γ	$z_{c,0}$	M_c	Φ^*	χ^2	ν
VVDS+SDSS - LDDE	-3.29	-2.0	-24.38	6.54	-1.37	0.21	2.08	-27.36	2.79E-8	64.6	67

Chapter 9

Conclusion

In this work we have studied the properties and the evolution of a spectroscopic type–1 AGN sample collected by the VVDS. The sample consists of 130 BLAGN at $0< z <5$ and constitutes an unprecedented opportunity to explore the variety of properties of the entire AGN population. This sample presents two major advantages with respect to other existing samples:

- **The BLAGN have been selected on the basis of only their spectral features, with no morphological and/or color selection biases.**
  The absence of these biases is particularly important for this sample because the typical non-thermal AGN continuum can be significantly masked by the emission of the host galaxy at the low intrinsic luminosity of the VVDS AGN. This makes the optical selection of the faint AGN candidates very difficult using the standard color and morphological criteria. Only spectroscopic surveys without any pre-selection can therefore be considered complete in this luminosity range.

- **The limiting magnitudes ($I_{AB} = 22.5$ and $I_{AB} = 24$ for the *wide* and *deep* sample, respectively) represent the faintest limit ever reached among the existing spectroscopically selected samples of AGN**. In terms of number of objects, depth and covered area, only photometric selected samples are comparable to the one presented here.

The main results found in this study are here summarized:

(i) We tested the classical ultraviolet-excess preselection technique based on three color bands by applying this method *a posteriori* to our sample and we concluded that classical optical preselection techniques are significantly under-sampling the overall BLAGN population in deep samples. In fact, by comparing the $u-g$, $g-r$ color distribution of our AGN population with $z < 2.3$ and $I_{AB} < 22.5$ with the usually adopted photometric selection criteria on stellar-like objects, we find that $\sim 35\%$ of the AGN present in our sample would be missed by the usual UV excess and

morphological criteria used for the preselection of optical QSO candidates in this redshift range. Most of the extended VVDS BLAGN are below the redshift $z = 1.6$, a redshift range where 42% of VVDS BLAGN are extended.

(ii) After a comprehensive analysis of our selection function, we measured the surface density of BLAGN in the sky: we find 472 ± 48 BLAGN per deg^2 with a magnitude $I_{AB} \leq 24$. A turn-over is observed in the differential number counts at $I_{AB} \sim 21.5$;

These results have been published in Gavignaud, I.; Bongiorno, A. et al., 2006

(iii) Because of the absence of morphological and color selection, our sample shows redder colors than those expected, for example, on the basis of the color track derived from the SDSS composite spectrum and the difference is stronger for the intrinsically faintest objects. Thanks to the extended multi-wavelength coverage in the deep VVDS fields in which we have, in addition to the optical VVDS bands, also photometric data from GALEX, CFHTLS, UKIDSS and Spitzer, we examined the Spectral Energy Distribution of each object and we fitted it with a combination of AGN and galaxy emission, allowing also for the possibility of extinction of the AGN flux. We found that both effects (presence of dust and contamination from the host galaxy) are likely to be responsible for this reddening, even if it is not possible to exclude that some of the faint AGN are intrinsically redder. In particular, we found that for $\sim$44% of our objects the contamination from the host galaxy is not negligible. The fraction decreases to $\sim$21% if we restrict the analysis to a bright sub-sample (M_{1450} <-22.15).

(iv) We derived the luminosity function in the B-band for $1 < z < 3.6$, by applying the usual $1/V_{max}$ estimator (Schmidt, 1968), which gives the space density contributions of individual objects. Moreover, using the expressions recently derived by Hopkins et al. (2007), we computed also the bolometric luminosity function for our sample. This allows us to compare our results also with other samples selected from different bands. Our data sample the faint part of the bolometric luminosity function better than all previous optically selected samples and are in good agreement with all the other samples, selected in different bands, and thus also with the model fit derived by Hopkins et al. (2007).

(v) Our data, more than one magnitude fainter than previous optical surveys, allow us to constrain the faint part of the luminosity function up to high redshift. A comparison of our data with the 2dF sample at low redshift ($1 < z < 2.1$) shows that the VDDS data can not be well fitted with the PLE models derived by previous samples. Qualitatively, this appears to be due to the fact that our data suggest the presence of an excess of faint objects at low redshift ($1.0 < z < 1.5$) with respect to these models. This is in agreement with the results, recently found by a growing

number of observations at different redshifts, in soft and hard X-ray bands. They have found in fact evidences of a similar trend and they have reproduced it with a luminosity-dependent density evolution parameterization. Such a parameterization allows the redshift of the AGN density peak to change as a function of luminosity and explains the excess of faint AGN that we found at $1.0 < z < 1.5$.

(vi) By combining our faint VVDS sample with the large sample of bright AGN extracted from the SDSS DR3 (Richards et al., 2006b), we found that the evolutionary model which better represents the combined luminosity functions, over a wide range of redshift and luminosity, is an LDDE model, similar to those derived from the major X-surveys. The derived faint end slope at z=0 is β = -2.0, consistent with the value derived by Hao et al. (2005) studying the emission line luminosity function of a sample of Seyfert galaxies at very low redshift.

(vii) By integrating the luminosity function corresponding to our best fit model (i.e. the LDDE model), we derived the comoving AGN space density as a function of redshift for different luminosity ranges. We found that the comoving AGN space density shows a shift of the peak with luminosity, in the sense that more luminous AGN peak earlier in the history of the Universe (i.e. at higher redshift), while the density of low luminosity ones reaches its maximum later (i.e. at lower redshift). In particular, in our best fit LDDE model the peak of the space density ranges from z $\sim$ 2 for $M_B <$ -26 to z$\sim$ 0.65 for -22 $< M_B <$ -20. This effect had not been seen so far in the analysis of optically selected samples, probably because most of the optical samples do not sample in a complete way the faintest luminosities, where the difference in the location of the peak becomes evident.

These results are presented in Bongiorno, A.; Zamorani, G. et al., 2007 (to be submitted)

Although the results here presented appear to be already robust, the larger AGN sample we will have at the end of the still on-going VVDS survey ($>$ 300 AGN), will allow a better statistical analysis and a better estimate of the parameters of the evolutionary model.

Bibliography

Abazajian, K., Adelman-McCarthy, J. K., Agüeros, M. A., et al. 2005, AJ, 129, 1755

Abazajian, K., Adelman-McCarthy, J. K., Agüeros, M. A., et al. 2003, AJ, 126, 2081

Abell, G. O. 1962, Galaxies: Landmarks in the Universe (Stars and Galaxies: Birth, Ageing, and Death in the Universe), 79–+

Adami, C., Mazure, A., Ilbert, O., et al. 2005, A&A, 443, 805

Alexander, D. M., Bauer, F. E., Brandt, W. N., et al. 2003, AJ, 126, 539

Antonucci, R. 1993, ARA&A, 31, 473

Antonucci, R. R. J. 1982, Nature, 299, 605

Antonucci, R. R. J. & Miller, J. S. 1985, ApJ, 297, 621

Arnouts, S., Vandame, B., Benoist, C., et al. 2001, A&A, 379, 740

Avni, Y. & Bahcall, J. N. 1980, ApJ, 235, 694A

Baldwin, J. A. 1977, ApJ, 214, 679

Barger, A. J., Cowie, L. L., Capak, P., et al. 2003, AJ, 126, 632

Barger, A. J., Cowie, L. L., Mushotzky, R. F., et al. 2005, AJ, 129, 578

Becker, R. H., White, R. L., Gregg, M. D., et al. 2001, ApJS, 135, 227

Becker, R. H., White, R. L., & Helfand, D. J. 1995, ApJ, 450, 559

Bondi, M., Ciliegi, P., Zamorani, G., et al. 2003, A&A, 403, 857

Bottini, D., Garilli, B., Maccagni, D., et al. 2005, PASP, 117, 996

Boyle, B. J., Shanks, T., Croom, S. M., et al. 2000, MNRAS, 317, 1014

Boyle, B. J., Shanks, T., & Peterson, B. A. 1988, MNRAS, 235, 935

Brandt, W. N., Hornschemeier, A. E., Schneider, D. P., et al. 2000, AJ, 119, 2349

Brown, M. J. I., Brand, K., Dey, A., et al. 2006, ApJ, 638, 88

Brunzendorf, J. & Meusinger, H. 2002, A&A, 390, 879

Bruzual, G. & Charlot, S. 2003, MNRAS, 344, 1000

Cimatti, A., Daddi, E., & Renzini, A. 2006, A&A, 453, L29

Cimatti, A., Zamorani, G., & Marano, B. 1993, MNRAS, 263, 236

Cirasuolo, M., Magliocchetti, M., & Celotti, A. 2005, MNRAS, 357, 1267

Colless, M., Dalton, G., Maddox, S., et al. 2001, MNRAS, 328, 1039

Comastri, A., Fiore, F., Vignali, C., et al. 2001, MNRAS, 327, 781

Condon, J. J., Cotton, W. D., Greisen, E. W., et al. 1998, AJ, 115, 1693

Contini et al. 2007, in preparation

Cowie, L. L., Barger, A. J., Bautz, M. W., Brandt, W. N., & Garmire, G. P. 2003, ApJ, 584, L57

Cowie, L. L., Songaila, A., Hu, E. M., & Cohen, J. G. 1996, AJ, 112, 839

Croom, S. M., Smith, R. J., Boyle, B. J., et al. 2004, MNRAS, 349, 1397

Dessauges-Zavadsky, M., Pindao, M., Maeder, A., & Kunth, D. 2000, A&A, 355, 89

Devriendt, J. E. G., Guiderdoni, B., & Sadat, R. 1999, A&A, 350, 381

Di Matteo, T., Springel, V., & Hernquist, L. 2005, Nature, 433, 604

Fabian, A. C. 1999, MNRAS, 308, L39

Fan, X., Strauss, M. A., Schneider, D. P., et al. 2001, AJ, 121, 54

Fath, E. A. 1908, Lick Observatory Bulletin, 5, 71

Ferrarese, L. & Merritt, D. 2000, ApJ, 539, L9

Fiore, F., Brusa, M., Cocchia, F., et al. 2003, A&A, 409, 79

Fiore, F., La Franca, F., Giommi, P., et al. 1999, MNRAS, 306, L55

Floyd, D. J. E., Kukula, M. J., Dunlop, J. S., et al. 2004, MNRAS, 355, 196

Fontanot, F., Cristiani, S., Monaco, P., et al. 2007, A&A, 461, 39

Francis, P. J., Hewett, P. C., Foltz, C. B., et al. 1991, ApJ, 373, 465

Gavignaud, I., Bongiorno, A., Paltani, S., et al. 2006, A&A, 457, 79

Gebhardt, K., Bender, R., Bower, G., et al. 2000, ApJ, 539, L13

Gehrels, N. 1986, ApJ, 303, 336

Giacconi, R., Bechtold, J., Branduardi, G., et al. 1979, ApJ, 234, L1

Giacconi, R., Gursky, H., Paolini, F. R., & Rossi, B. B. 1962, Physical Review Letters, 9, 439

Giacconi, R., Zirm, A., Wang, J., et al. 2002, ApJS, 139, 369

Hall, P. B., Gallagher, S. C., Richards, G. T., et al. 2006, AJ, 132, 1977

Hao, L., Strauss, M. A., Fan, X., et al. 2005, AJ, 129, 1795

Hartwick, F. D. A. & Schade, D. 1990, ARA&A, 28, 437

Hasinger, G., Burg, R., Giacconi, R., et al. 1993, A&A, 275, 1

Hasinger, G., Burg, R., Giacconi, R., et al. 1998, A&A, 329, 482

Hasinger, G., Miyaji, T., & Schmidt, M. 2005, A&A, 441, 417

Heckman, T. M. 1980, A&A, 87, 142

Hewett, P. C., Foltz, C. B., & Chaffee, F. H. 1995, AJ, 109, 1498

Hewett, P. C., Foltz, C. B., Chaffee, F. H., et al. 1991, AJ, 101, 1121

Hewett, P. C., Irwin, M. J., Bunclark, P., et al. 1985, MNRAS, 213, 971

Hoag, A. A. & Schroeder, D. J. 1970, PASP, 82, 1141

Hopkins, P. F., Hernquist, L., Cox, T. J., et al. 2005a, ApJ, 630, 716

Hopkins, P. F., Hernquist, L., Cox, T. J., et al. 2006a, ApJS, 163, 1

Hopkins, P. F., Hernquist, L., Cox, T. J., et al. 2006b, ApJ, 639, 700

Hopkins, P. F., Hernquist, L., Martini, P., et al. 2005b, ApJ, 625, L71

Hopkins, P. F., Richards, G. T., & Hernquist, L. 2007, ApJ, 654, 731

Huchra, J. P. 1977, ApJS, 35, 171

Hunt, M. P., Steidel, C. C., Adelberger, K. L., & Shapley, A. E. 2004, ApJ, 605, 625

Ilbert, O., Lauger, S., Tresse, L., et al. 2006, A&A, 453, 809

Ilbert, O., Tresse, L., Zucca, E., et al. 2005, A&A, 439, 863

Iovino, A., McCracken, H. J., Garilli, B., et al. 2005, A&A, 442, 423

Jackson, C. A., Wall, J. V., Shaver, P. A., et al. 2002, A&A, 386, 97

Jahnke, K., Sánchez, S. F., Wisotzki, L., et al. 2004, ApJ, 614, 568

Jiang, L., Fan, X., Cool, R. J., et al. 2006, AJ, 131, 2788

Kellermann, K. I., Sramek, R., Schmidt, M., Shaffer, D. B., & Green, R. 1989, AJ, 98, 1195

Kennefick, J. D., Djorgovski, S. G., & de Carvalho, R. R. 1995, AJ, 110, 2553

Kewley, L. J., Groves, B., Kauffmann, G., & Heckman, T. 2006, ArXiv Astrophysics e-prints

Kewley, L. J., Heisler, C. A., Dopita, M. A., & Lumsden, S. 2001, ApJS, 132, 37

Khachikian, E. Y. & Weedman, D. W. 1974, ApJ, 192, 581

Kormendy, J. & Richstone, D. 1995, ARA&A, 33, 581

Kron, R. G. 1980, ApJS, 43, 305

Kron, R. G. & Chiu, L.-T. G. 1981, PASP, 93, 397

La Franca, F., Fiore, F., Vignali, C., et al. 2002, ApJ, 570, 100

Lacy, M., Storrie-Lombardi, L. J., Sajina, A., et al. 2004, ApJS, 154, 166

Le Fèvre, O., Mellier, Y., McCracken, H. J., et al. 2004, A&A, 417, 839

Le Fèvre, O., Guzzo, L., Meneux, B., et al. 2005a, A&A, 439, 877

Le Fèvre, O., Paltani, S., Arnouts, S., et al. 2005b, Nature, 437, 519

Le Fèvre, O., Vettolani, G., Garilli, B., et al. 2005c, A&A, 439, 845

Lehmann, I., Hasinger, G., Schmidt, M., et al. 2001, A&A, 371, 833

Lilly, S. J., Tresse, L., Hammer, F., Crampton, D., & Le Fevre, O. 1995, ApJ, 455, 108

Magorrian, J., Tremaine, S., Richstone, D., et al. 1998, AJ, 115, 2285

Marconi, A. & Hunt, L. K. 2003, ApJ, 589, L21

Marinoni, C., Le Fèvre, O., Meneux, B., et al. 2005, A&A, 442, 801

Marshall, H. L. 1987, AJ, 94, 628

Marshall, H. L., Tananbaum, H., Avni, Y., & Zamorani, G. 1983, ApJ, 269, 35

Martínez-Sansigre, A., Rawlings, S., Lacy, M., et al. 2005, Nature, 436, 666

Mathez, G. 1976, A&A, 53, 15

Matthews, T. A. & Sandage, A. R. 1963, ApJ, 138, 30

Matute, I., La Franca, F., Pozzi, F., et al. 2006, A&A, 451, 443

McCracken, H. J., Le Fèvre, O., Brodwin, M., et al. 2001, A&A, 376, 756

McCracken, H. J., Radovich, M., Bertin, E., et al. 2003, A&A, 410, 17

McHardy, I. M., Jones, L. R., Merrifield, M. R., et al. 1998, MNRAS, 295, 641

McLeod, K. K. & Rieke, G. H. 1995, ApJ, 454, L77+

McLure, R. J. & Dunlop, J. S. 2002, MNRAS, 331, 795

Mihalas, D. & Binney, J. 1981, Science, 214, 829

Miyaji, T., Hasinger, G., & Schmidt, M. 2000, A&A, 353, 25

Miyaji, T., Hasinger, G., & Schmidt, M. 2001, A&A, 369, 49

Morrissey, P., Schiminovich, D., Barlow, T. A., et al. 2005, ApJ, 619, L7

Mushotzky, R. F., Cowie, L. L., Barger, A. J., & Arnaud, K. A. 2000, Nature, 404, 459

Norman, C., Hasinger, G., Giacconi, R., et al. 2002, ApJ, 571, 218

Oke, J. B. & Sandage, A. 1968, ApJ, 154, 21

Osmer, P. S. 1982, ApJ, 253, 28

Osterbrock, D. E. 1981, ApJ, 249, 462

Osterbrock, D. E. & Koski, A. T. 1976, MNRAS, 176, 61P

Page, M. J., Mason, K. O., McHardy, I. M., Jones, L. R., & Carrera, F. J. 1997, MNRAS, 291, 324

Pei, Y. C. 1995, ApJ, 438, 623

Peterson, B. A. 1988, in ASP Conf. Ser. 2: Optical Surveys for Quasars, ed. P. Osmer & M. M. Phillips, 23–+

Pierre, M., Valtchanov, I., Altieri, B., et al. 2004, Journal of Cosmology and Astro-Particle Physics, 9, 11

Pollo, A., Meneux, B., Guzzo, L., et al. 2005, A&A, 439, 887

Prevot, M. L., Lequeux, J., Prevot, L., Maurice, E., & Rocca-Volmerange, B. 1984, A&A, 132, 389

Radovich, M., Arnaboldi, M., Ripepi, V., et al. 2004, A&A, 417, 51

Reber, G. 1944, ApJ, 100, 279

Rengstorf, A. W., Mufson, S. L., Abad, C., et al. 2004, ApJ, 606, 741

Richards, G. T., Croom, S. M., Anderson, S. F., et al. 2005, MNRAS, 360, 839

Richards, G. T., Fan, X., Newberg, H. J., et al. 2002, AJ, 123, 2945

Richards, G. T., Hall, P. B., Vanden Berk, D. E., et al. 2003, AJ, 126, 1131

Richards, G. T., Lacy, M., Storrie-Lombardi, L. J., et al. 2006a, ApJS, 166, 470

Richards, G. T., Strauss, M. A., Fan, X., et al. 2006b, AJ, 131, 2766

Richards, G. T., Strauss, M. A., Fan, X., et al. 2006c, AJ, 131, 2766

Rola, C. S., Terlevich, E., & Terlevich, R. J. 1997, MNRAS, 289, 419

Sajina, A., Lacy, M., & Scott, D. 2005, ApJ, 621, 256

Salpeter, E. E. 1955, ApJ, 121, 161

Sandage, A. & Luyten, W. J. 1967, ApJ, 148, 767

Scannapieco, E. & Oh, S. P. 2004, ApJ, 608, 62

Schade, D., Crampton, D., Hammer, F., Le Fèvre, O., & Lilly, S. J. 1996, MNRAS, 278, 95

Schade, D. J., Boyle, B. J., & Letawsky, M. 2000, MNRAS, 315, 498

Schlegel, D. J., Finkbeiner, D. P., & Davis, M. 1998, ApJ, 500, 525

Schmidt, M. 1963, Nature, 197, 1040

Schmidt, M. 1968, ApJ, 151, 393

Schmidt, M. & Green, R. F. 1983, ApJ, 269, 352

Schmidt, M., Hasinger, G., Gunn, J., et al. 1998, A&A, 329, 495

Schmidt, M., Schneider, D. P., & Gunn, J. E. 1995, AJ, 110, 68

Scodeggio, M., Franzetti, P., Garilli, B., et al. 2005, A&A, 000, 00

Seyfert, C. K. 1943, ApJ, 97, 28

Shakura, N. I. 1973, Soviet Astronomy, 16, 756

Shankar, F., Salucci, P., Granato, G. L., De Zotti, G., & Danese, L. 2004, MNRAS, 354, 1020

Silk, J. & Rees, M. J. 1998, A&A, 331, L1

Silverman, J. D., Green, P. J., Barkhouse, W. A., et al. 2005, ApJ, 624, 630

Smith, E. P., Heckman, T. M., Bothun, G. D., Romanishin, W., & Balick, B. 1986, ApJ, 306, 64

Smith, H. J. & Hoffleit, D. 1963, AJ, 68, 292

Spergel, D. N., Bean, R., Doré, O., et al. 2006, ArXiv Astrophysics e-prints

Springel, V., Di Matteo, T., & Hernquist, L. 2005a, ApJ, 620, L79

Springel, V., Di Matteo, T., & Hernquist, L. 2005b, MNRAS, 361, 776

Steed, A. & Weinberg, D. H. 2003, ArXiv Astrophysics e-prints

Steidel, C. C., Adelberger, K. L., Giavalisco, M., Dickinson, M., & Pettini, M. 1999, ApJ, 519, 1

Steidel, C. C., Hunt, M. P., Shapley, A. E., et al. 2002, ApJ, 576, 653

Szokoly, G. P., Bergeron, J., Hasinger, G., et al. 2004, ApJS, 155, 271

Taylor, G. L., Dunlop, J. S., Hughes, D. H., & Robson, E. I. 1996, MNRAS, 283, 930

Treister, E., Urry, C. M., Van Duyne, J., et al. 2006, ApJ, 640, 603

Tremaine, S., Gebhardt, K., Bender, R., et al. 2002, ApJ, 574, 740

Ueda, Y., Akiyama, M., Ohta, K., & Miyaji, T. 2003, ApJ, 598, 886

Urry, C. M. & Padovani, P. 1995, PASP, 107, 803

Vanden Berk, D. E., Richards, G. T., Bauer, A., et al. 2001, AJ, 122, 549

Veilleux, S. & Osterbrock, D. E. 1987, ApJS, 63, 295

Vittorini, V., Shankar, F., & Cavaliere, A. 2005, MNRAS, 363, 1376

Volonteri, M., Haardt, F., & Madau, P. 2003, ApJ, 582, 559

Warren, S. J., Hewett, P. C., Irwin, M. J., & Osmer, P. S. 1991, ApJS, 76, 1

Warren, S. J., Hewett, P. C., & Osmer, P. S. 1994, ApJ, 421, 412

Weedman, D. W., Feldman, F. R., Balzano, V. A., et al. 1981, ApJ, 248, 105

White, R. L., Becker, R. H., Gregg, M. D., et al. 2000, ApJS, 126, 133

White, S. D. M. & Rees, M. J. 1978, MNRAS, 183, 341

Wisotzki, L., Christlieb, N., Bade, N., et al. 2000, A&A, 358, 77

Wolf, C., Meisenheimer, K., Rix, H.-W., et al. 2003a, A&A, 401, 73

Wolf, C., Wisotzki, L., Borch, A., et al. 2003b, A&A, 408, 499

Worsley, M. A., Fabian, A. C., Bauer, F. E., et al. 2005, MNRAS, 357, 1281

Wyithe, J. S. B. & Loeb, A. 2002, ApJ, 581, 886

Zamorani, G., Mignoli, M., Hasinger, G., et al. 1999, A&A, 346, 731

Zucca, E., Ilbert, O., Bardelli, S., et al. 2006, A&A, 455, 879

List of Figures

2.1 Composite optical spectra of type–1 and type–2 AGN 12
2.2 Unified Model of AGN 14

3.1 Example of UVX selection technique 19
3.2 Examples of multicolor selection technique 19
3.3 Example of standard diagnostic diagrams 22

4.1 Positions of the 4 VIRMOS fields on a dust map of the sky 30
4.2 Typical layout of VIMOS spectra 31
4.3 Examples of VVDS spectra in the range $0 < z \leq 0.7$. 33
4.4 Examples of VVDS spectra in the range $0.7 < z \leq 1.3$. 34
4.5 Examples of VVDS spectra in the range $1.3 < z \leq 2.2$. 34
4.6 Examples of VVDS spectra in the range $2.2 < z \leq 5.0$. 35
4.7 Redshift distribution of the VVDS deep sample. 36
4.8 Color diagram of the VVDS high-redshift galaxies. 39

5.1 AGN position in the spectroscopically observed area 43
5.2 Visibility of AGN broad emission lines, in the VVDS wavelength range . 44
5.3 AGN quality flags statistics 45
5.4 Examples of BLAGN spectra 46
5.5 Redshift distributions of the wide and the deep VVDS BLAGN sample . . 47
5.6 Apparent I_{AB} magnitude as a function of redshift 48
5.7 Morphological analysis 50
5.8 Redshift distribution of BLAGN sample 51
5.9 Color-Color diagram. 52
5.10 Composite spectrum 53
5.11 Differences as a function of redshift between the observed $B_{AB} - I_{AB}$ colors and the color expected for the SDSS composite spectrum 56
5.12 Distribution of the spectral index α 56
5.13 Composite spectra for the “bright” and “faint” sub-samples 58
5.14 Difference between the VVDS-AGN composite spectrum and the SDSS one 59

5.15 Example of an AGN templates with different extinction values 61
5.16 Examples of galaxy templates 61
5.17 Examples of decompositions of the observed SEDs 63

6.1 Incompleteness function: *Target Sampling Rate* 70
6.2 Incompleteness function: *Spectroscopic Success Rate* 71
6.3 VVDS-BLAGN cumulative surface density 74
6.4 BLAGN differential surface density 75
6.5 Surface density: comparison with the COMBO-17 sample 76

7.1 Optical QSO luminosity function for the 2Qz sample 81
7.2 Soft X–ray luminosity function of the type–1 AGN sample Hasinger et al. (2005) 82
7.3 Space density of X-ray selected AGN as a function of redshift (Hasinger et al., 2005) 83
7.4 Space density of optically selected AGN as a function of redshift Wolf et al. (2003b) 84

8.1 Real and simulated -band absolute magnitude differences as a function of M_B(TOT) and redshift 89
8.2 VVDS B-band luminosity function at low redshift 92
8.3 VVDS B-band luminosity function at high redshift 94
8.4 Bolometric corrections derived by Hopkins et al. (2007) 95
8.5 VVDS bolometric luminosity function 96
8.6 VVDS+SDSS B-band luminosity function: model fitting 99
8.7 Comparison between our LF best-fit model extrapolated at z=0 and the model derived by Hao et al. (2005) 101
8.8 Evolution of the comoving AGN space density with redshift 102

List of Tables

3.1 Examples of recent AGN surveys 25

4.1 Survey fields 29
4.2 Summary of the VVDS Epoch-1 spectroscopic fields. 32

5.1 Emission lines properties of the VVDS and SDSS composite spectra . . . 55
5.2 BLAGN with secure redshift 65
5.2 continued. 66
5.2 continued. 67
5.3 AGN with a single emission line detected 68

6.1 BLAGN number counts as function of I_{AB} magnitude 74

8.1 Binned luminosity function estimate 104
8.2 Best fit models of the combined sample VVDS+SDSS-DR3 105